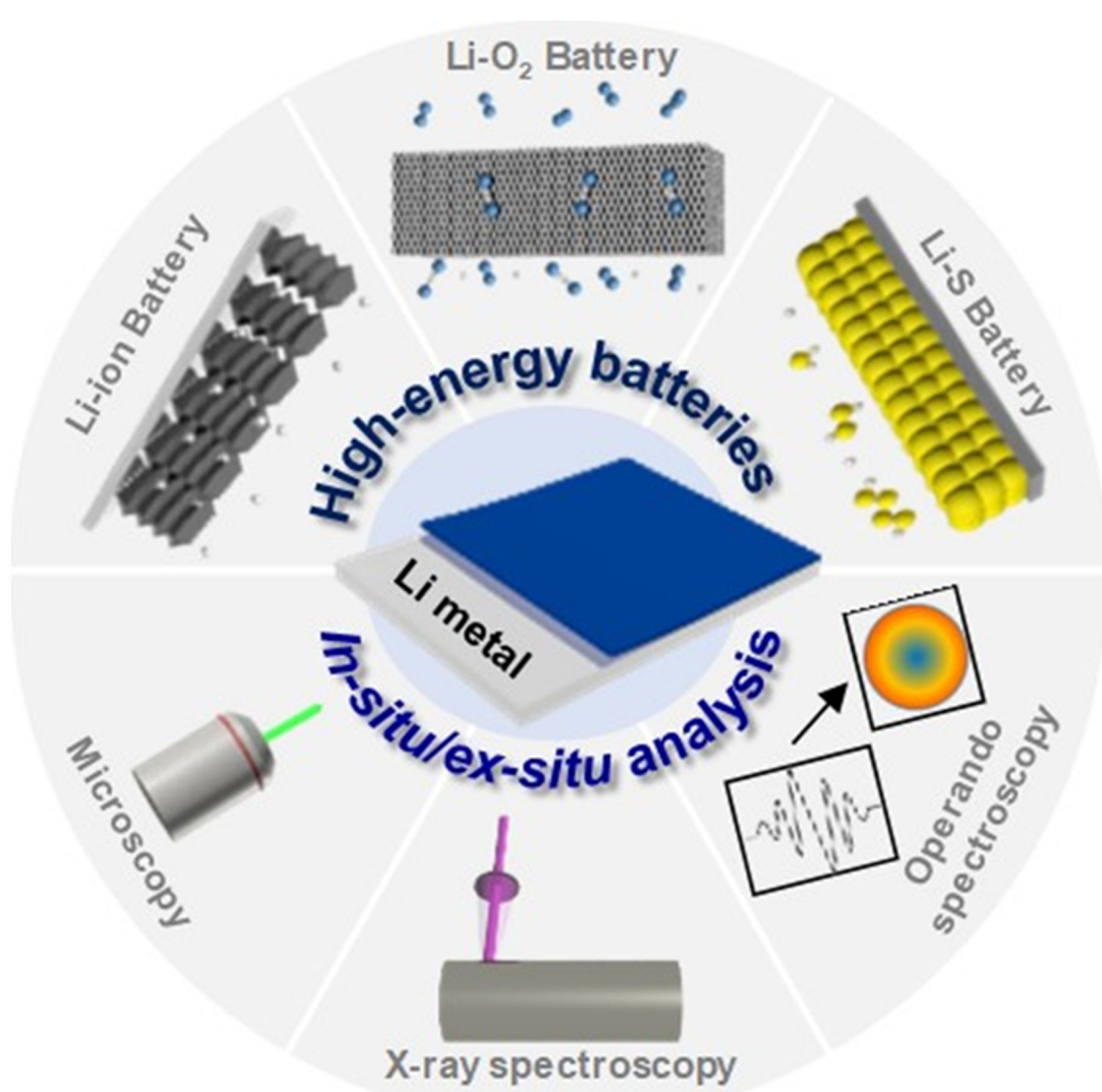


Special
Collection

Lithium Metal Interface Modification for High-Energy Batteries: Approaches and Characterization

Jung-In Lee^{+[a]}, Gyujin Song^{+[a]}, Sungjin Cho,^[b] Dong-Yeob Han,^[b] and Soojin Park*^[a, b]

Rechargeable batteries have been a profoundly greater part of our lives than we could have ever imagined. The rechargeable Li-ion batteries (LIBs) that have been developed for transport systems even put fossil fuels in the corner. However, state-of-the-art Li-ion batteries with graphite anodes are now approaching their theoretical specific energy limits, so they cannot meet the increasing demands of a range of portable electronics and large-scale energy storage systems. Li metal is one of the most promising anode materials that could break through the energy density bottleneck of Li-ion batteries due to its ultrahigh specific capacity and very low potential compared to other anode materials. Nonetheless, the direct use of Li metal in commercial battery systems has been hindered due to significant obstacles associated with it such as safety issues, corrosion from chemical reactions that occur inside the battery, or poor cycling performance. The fundamental reason for these problems is the dendritic growth of Li-ions on the Li metal anode during cycling, as a result of the interfacial phenomena of Li

metal and electrolytes. Modification of the Li metal interface with an electrolyte presents an efficient solution to solve these problems. In this review, the current challenges facing the development of Li metal anodes are presented in detail. The most recent advances in Li metal anodes using a controlled interface between the Li metal surface and an electrolyte are highlighted and an introduction on the synthesis and production methods for the application of high-energy-density battery systems such as Li-oxygen ($\text{Li}-\text{O}_2$), Li-sulfur ($\text{Li}-\text{S}$), and Li metal batteries with high-energy density cathodes is presented. Furthermore, the recent developments in the *in situ*/operando analysis tools adopted for the investigation of Li metal anodes such as the structural and chemical changes, dynamic properties, and solid–electrolyte interface (SEI) layer properties are described and summarized. Finally, some suggestions are given in the direction of the development of Li metal with artificial surface layers for use in future high-energy batteries.

1. Introduction

Li-ion batteries (LIBs) have revolutionized our lives to the extent that they can be used to power devices in our pockets. As a battery anode material, Li metal is undoubtedly considered the most suitable candidate due to its high theoretical capacity (3860 mAh g^{-1}), low density (0.534 g cm^{-3}), and low potential (-3.04 V vs. the standard hydrogen electrode)^[1–3] since it was first used as an anode in the development of rechargeable batteries by Whittingham.^[4] However, its use had some severe shortcomings, such as severe capacity fading and posed a potential explosion hazard as a result of its propensity for dendritic Li growth.^[5–7]

Consequently, the first commercial LIBs developed by Sony in 1991 adopted LiCoO_2 as a cathode and a carbon-based anode.^[8] The advent of commercial LIBs was game-changing for the battery market, and primary batteries became speedily substituted for LIBs that at that time delivered a higher specific energy density of 80 Wh kg^{-1} and energy density of 80 Wh L^{-1} with a charge range up to 4.1 V .^[9] From that point on, the research on LIBs flourished toward further increasing the energy and power density, in parallel with the rapidly increasing use of various electronic devices in new industries, such as electric vehicles (EV), aerospace, and large-scale energy storage stations.^[10–13] Nowadays, thanks to remarkable progress

achieved in science and technology, there has been a resurgence of Li metal anodes to supplant carbon-based anodes in the commercial LIBs that are approaching their limit of capability.^[5–6,14–17] Once the anode is replaced with Li metal, Li metal batteries (LMBs) applied with Li transition metal oxides as cathodes can exhibit a specific energy density of $\sim 400 \text{ Wh kg}^{-1}$.^[18] Furthermore, next-generation battery systems using sulfur and oxygen as cathodes can boost the theoretical specific energy to $\sim 2600 \text{ Wh kg}^{-1}$ and $\sim 3582 \text{ Wh kg}^{-1}$, respectively.^[3,19–21]

Recently, various research groups have been devoting all of their efforts into understanding Li metal anode mechanisms and upgrading Li metal anodes by trying out new methods.^[2,16,22–23] First, porous host structures have been used to reduce the local current density on the electrode surface to accommodate volume expansion and to prevent dendritic Li growth using strategies involving 3D carbon^[24–29] and 3D inactive metal structures.^[30–35] Second, another useful solution is to develop a new electrolyte system.^[36–38] Generally, commercial carbonate-based electrolytes are not suitable for Li metal batteries due to their high flammability and low coulombic efficiency during cycling.^[36,39–41] Therefore, the strategies that have been pursued to this end include modifying components of the liquid electrolyte, introducing new electrolyte systems such as solid and polymer electrolytes,^[42–48] and adding particulate-based additives.^[32,49–53] Finally, Li metal interface modification is a practical approach that can be achieved using *ex situ* and *in situ* artificial layers.^[38,54–59] The artificial layer (or protective layers) on the Li metal surface promotes a stable solid electrolyte surface and uniform Li-ion flux distribution, resulting in the development of safe and high-performance Li metal anodes.^[31,52,60–65] It is a definite fact that these approaches have contributed toward the investigation of high-energy batteries, even though it cannot yet be a judge what the best solution for Li metal anodes is.

- [a] Dr. J.-I. Lee,[†] Dr. G. Song,[†] Prof. S. Park
Department of Chemistry
Pohang University of Science and Technology (POSTECH)
Pohang 37673, Republic of Korea
E-mail: soojin.park@postech.ac.kr
- [b] S. Cho, D.-Y. Han, Prof. S. Park
Division of Advanced Materials Science
Pohang University of Science and Technology (POSTECH)
Pohang 37673, Republic of Korea
- [†] These authors contributed equally to this work.
- Special Collection
An invited contribution to a Special Collection on Lithium Metal Anode Processing and Interface Engineering

Figure 1a summarizes the number of papers on this subject as of November 2019 based on the data from the Web of Science searched using keywords "Li metal anode". The number of articles on Li metal anodes has rapidly increased since 2010. This increase in the number of papers is a testament to the intense interest of researchers in the field of Li metal batteries. Furthermore, the search adding to a keyword "dendrite" shows rising concern about the problem with lithium metal anodes (Figure 1b). Among these papers, the concept of Li metal interface modification as mentioned above has been the most widely used approach, as can be seen in Figure 1c. This is because there are various ways of achieving these; one is via an *in situ* solid electrolyte interface (SEI) layer that originates from the interfacial reactions between Li-metal anodes, and the other is the use of *ex situ* artificial layers.

Hence, a comprehensive review is presented here which aims to provide an overview of the fundamentals of Li metal anodes and to summarize the recent approaches involving Li metal interface modification in high-energy-density battery systems. In addition, recent advances in the methods used to analyze Li metal anodes are briefly reviewed, plus the outlook for Li metal anodes in next-generation high-energy battery systems. The final goal of this review is to help readers who are interested in this field better understand the critical issues associated with the use of Li metal anodes and thus stimulate them to generate new ideas to speed up the commercialization of high-energy battery systems.

2. Challenges Associated with Li Metal Anodes

For Li metal anodes to be accepted into the battery market, there are many obstacles that need to be overcome, as shown in Figure 2. Li is an extremely reactive metal as it quickly loses an electron due to a shielding effect of the nucleus and then forms Li⁺ ions, which are highly reactive and thermodynamically unstable.^[23,66] Thus, in batteries, Li metal tends to spontaneously react with most atmospheric gases, electrolyte solvents, and salts, with or without a current flow. In addition, the flow of current during battery operation is irregularly localized on the surface of Li metal anodes, resulting in several severe problems, such as the formation of an unstable SEI layer, massive volume expansion, and unpredictable untoward reactions with electrolytes.^[67–69] Moreover, unlike in traditional Li-ion batteries where Li-ions move between electrodes in an electrolyte that acts as a conductive medium, batteries with Li metal anodes are accompanied by plating and stripping processes that give rise to the growth of dendritic Li.^[2,70–71] This is known to be the principal cause of the problems associated with the use of Li metal, especially thermal runaway and explosion hazards. Hence, the plating of free-dendritic Li is essential to create a viable anode material for use in high-energy battery systems. Cyclability related to coulombic efficiency and overpotential is the other primary issue with Li metal. In electrochemical cycling, both Li metal and liquid electrolytes are consistently consumed alongside the formation of "dead Li" (inactive Li) and thick SEI layers. Also, it is the main culprit behind low coulombic efficiency in conventional



Dr. Jung-In Lee earned her Ph.D. in energy engineering from UNIST in 2014. She joined in Chemistry department at POSTECH as postdoctoral fellow in 2018. Her present research interests mainly focus on energy storage systems, including Li-ion batteries and Next generation batteries.



Dr. Gyujin Song received his Ph.D. in energy engineering from UNIST in 2020. He now works as a postdoctoral fellow in Chemistry at POSTECH. His research interests focus on the material design of anodes in Li-ion and Li metal batteries..



Sungjin Cho received his B.S. in Energy Engineering from UNIST in 2018. He is currently M.S.-Ph.D integrated course student in the School of Advanced Material Science at POSTECH. His research focuses on the material design of anodes in Li metal batteries..



Dong-Yeob Han received his B.S. in Chemical Engineering from UNIST in 2019. He is currently M.S.-Ph.D integrated course student in the School of Advanced Material Science at POSTECH. His research focuses on polymer membrane and Li metal batteries..



Prof. Soojin Park received his Ph.D. in chemistry from POSTECH in Korea. After he spent three years as a postdoctoral research associate at University of Massachusetts at Amherst, he joined to UNIST in 2009, and he moved to Chemistry department at POSTECH in 2017. His research interest includes design of deformablebatteries, synthesis of high capacity organic/inorganic anode materials, synthesis of poly-meric binder and separator for rechargeable batteries..

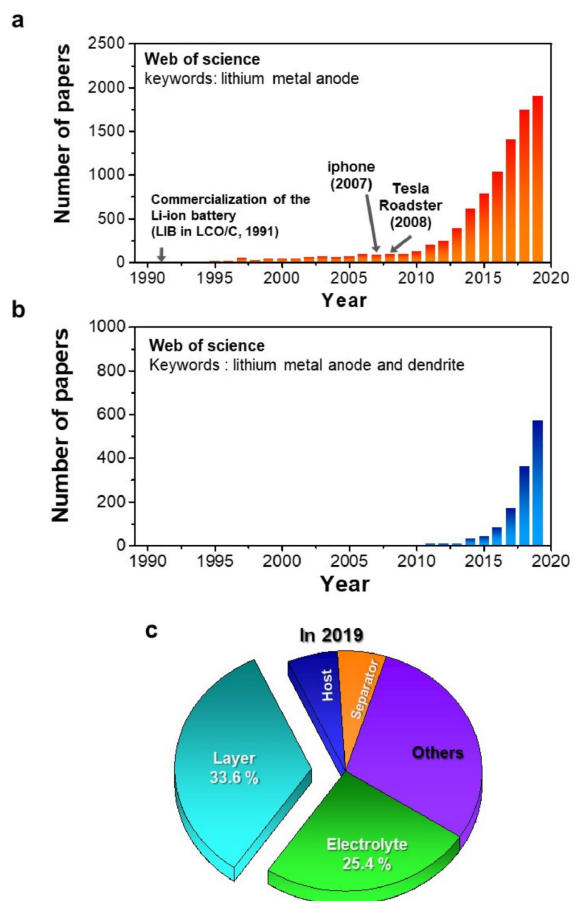


Figure 1. a) Number of papers on lithium metal anodes published each year from 1991 to November 2019. Total papers from 1991 to 2019 is a number of 9457 when a keyword is "lithium metal anode" for searching. b) Number of papers on lithium metal anodes published each year from 1991 to December 2019. Total papers from 1991 to 2019 is a number of 1345 when a keyword is "lithium metal anode and dendrite" for searching. c) Number of papers related to keywords such as "electrolyte", "layer", "host", and "separator" in the result searched after 'lithium metal anode' in November, 2019. The number of papers is a total number of 1941 in 2019. (The searching date: November 25, 2019)

carbonate electrolytes of less than 90%, and of approximately 99% in advanced electrolytes.^[72-76] The use of excess amounts

of Li metal and electrolytes is the quick-fix solution to attain stable batteries with a long life span.^[77] However, it is the antithesis of the new research stream toward investigating high-energy level batteries. In the following sections, the key challenges facing Li metal anodes are discussed in more detail.

2.1. Dendritic Li Growth and Short-Circuiting

During electroplating with a high-current density in electrolytes, the dendritic deposition of metals such as Li, sodium, nickel, zinc, and copper is a frequent occurrence, even though the different types of metals exhibit different morphologies.^[15,78-82] In this process, an ionic concentration gradient between the two electrodes in an electrolyte is essentially generated. During electroplating, the concentration of metal cations decreases at the anode electrode where these ions are removed from the electrolyte, while their concentration increases above their initial value close to the cathode where the metal cations enter the electrolyte. When the current reaches the limiting current density, the current is supplied only for a limited time, which is referred to as Sand's time.^[83] After the Sand's time, the ionic concentration falls to zero at the anode leading to the formation of dendritic Li.^[83-85] This process has been predicted using various ramified metallic deposition models.^[86] In 1990, Chazalviel proposed a mathematical model for ramified metallic deposition via electrodeposition from a dilute salt solution in a high electric current.^[87] It was found that ramified growth is a direct consequence of the space change that occurs upon anion depletion in the vicinity of the cathode. Later, Brissot experimentally confirmed ramified structural growth at anion drift velocity in a symmetrical Li battery with a poly(ethylene oxide)-Li bis(trifluoromethane sulfonyl)imide (PEO-LiTFSI) electrolyte.^[88-89] Thus, in the light of the principle mentioned above, it can be theoretically anticipated that no dendrites are formed when a battery works at a lower current density provoking the low gradient of the Li-ion concentration than the limiting current density. However, dendritic Li generates in actual battery systems that contain nonaqueous electrolytes.^[90-91]

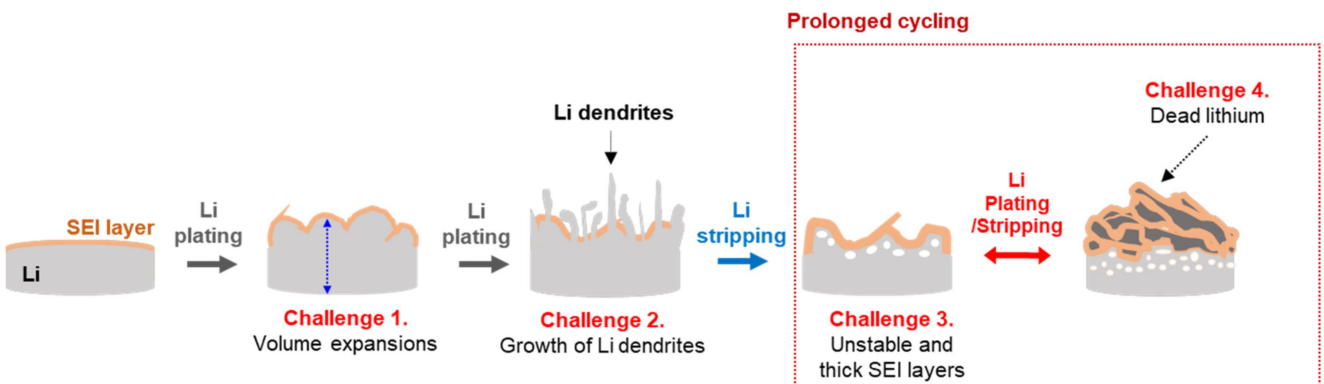


Figure 2. Schematic illustration of the various challenges faced by Li metal anodes during prolonged cycling.

Such models are not wrong, but they cannot perfectly mimic a complicated battery system due to their oversimplifications. In an actual battery, interfacial reactions between Li and the electrolyte need to be considered. In contrast to other metals, Li spontaneously forms an intricate SEI layer on its surface. The SEI layer is electrochemically insulating but ionically conductive, leading to the inhomogeneous nucleation of Li-ions on Li metal. Moreover, due to their poor elasticity, the SEI layer is vulnerable to cracking under stress originated from Li plating.^[92–93] Once a crack appears in the SEI layer, a fresh Li surface with both high electronic and ionic conductivity is exposed and thus becomes a new Li deposition site, resulting in the applied current density being localized there. Therefore, dendritic Li growth occurs, and the process is accelerated, without any mechanical restraints. This is one of the reasons that batteries short circuit, which results in fire.^[92,94–95]

2.2. The Infinite Volume Expansion of Li Metal Anodes

Most anode materials suffer from massive volume expansion when they react with Li, except for intercalation materials such as graphite anodes expand up to 13% when C₆ is fully lithiated to a composition of LiC₆.^[96] The volume expansion of silicon is known to be up to 400% in Li_{4.4}Si, as a result of an alloying reaction with Li.^[97–99] The problem is most acute in the case of Li anode materials due to them being hostless, which cannot stably support the movement of Li-ions between electrodes.^[100] A Li thickness of 20 μm has been shown to exhibit a capacity of 4 mAh cm⁻² in experimental studies published in the literature.^[101–102] Other studies have shown a volume expansion ratio of 156% for a Li metal thickness of 35 μm for a battery containing a high-energy-density LiNi_{1/3}Mn_{1/3}Co_{1/3}O₂ (NMC111) cathode and an excess Li metal anode with a thickness of 200 μm.^[67] This indicates that the thickness of the Li metal anode could be changed during cycling from almost zero to tens of micrometers. Therefore, this variation of Li metal anodes is mainly responsible for the crumbling of the inside configurations of batteries that have been perfectly designed without any space, along with cracking the SEI layers that it is similar to the phenomenon generated in alloy materials with Li-ions.^[94]

2.3. Unstable SEIs on Li Metal Anodes

Due to the highly negative electrochemical potential of Li/Li⁺, the formation of SEI layers in a battery occurs as a result of an inevitable parasitic reaction between a liquid electrolyte and Li metal. An unstable SEI layer leads to increased internal resistance, life span fading, dendritic Li growth, and low coulombic efficiency of the battery. In 1979, Peled first introduced a SEI layer in a battery without drawbacks,^[103] and there were then issues with this until Peled and Aubarch came up with new models in the 1990s.^[104–107] They suggested that the SEI layers consist of mosaic-type and multilayer microstructures of the products that arise from the reaction of the electrolyte and Li.^[103–104] After that, over several decades, many

researchers carried out experimental and theoretical studies to understand the structure and composition of carbon-based, silicon, and other anode materials.^[94,108–113] Recently, the SEI layers on Li metal anodes have been studied increasingly more over traditional anode materials.^[114–119] However, compared to conventional anodes, the prerequisites for a stable SEI layer on Li metal anodes are much more restrictive, as it is required to be homogeneous in composition, morphology, and ionic conductivity for the amicable diffusion of Li-ions, and must totally block electrons. Furthermore, excellent flexibility and electricity of the SEI layer are required because there is colossal and unpredictable fluctuation on the Li metal surface during cycling.^[92–93,120]

The SEI layer is a very complicated layer because its composition and properties may be dependent on numerous factors, such as electrolyte composition and concentration, the working conditions of the battery, including temperature, current density, and so on. Most SEI layers comprise products that form as a result of the degradation of electrolyte components, in the form of inorganic salts, solvent, and anions of salts, generated via reduction reactions.^[6,38,94,121–123]

This is particularly the case on the side of the SEI layer nearest to organic solvents, which makes up the main portion of the electrolyte, where there are sections divided into organic carbonates and ethers. Firstly, organic carbonates are the major electrolytes used in almost all commercial Li-ion batteries, but they are not suitable for Li metal anodes. Li alkyl carbonates (ROCOO–Li) are formed by decomposing organic carbonates after gaining one or two electrons from the Li metal surface and are then further converted to Li carbonates (Li₂CO₃) if the electrolyte contains any amount of H₂O.^[124–125] Moreover, as the cycling progresses, the SEI layer forms into two parts; one containing stable components such as Li halides (LiF), Li oxides (Li₂O), and Li carbonates (Li₂CO₃) as the innermost SEI layer closest to the Li metal surface, and the other is a metastable structure of polymeric Li alkyl carbonates (ROCOO–Li) in the outermost SEI layer that is in contact with the electrolyte.^[93,105,126–127] This structure of the SEI layers is what is described as a “mosaic model”, consisting of the heterogeneous stacking of small domains with distinct compositions.^[104] Thus, the SEI layer is short in terms of flexibility and healing properties, resulting in persistent growth on the freshly exposed Li surface after cracks develop in the SEI layer during cycling.

Ether-based electrolytes, such as dimethyl ether (DME), dioxolane (DOL), diethylene glycol dimethyl ether (DEGDME, diglyme), and so on, are also used. These electrolyte solvents are more stable for Li metal anodes, showing a higher coulombic efficiency of over 98% compared to carbonate-based electrolytes.^[36,128–131] The SEI formed in ether-based electrolyte consists of a more compact and thinner organic layer, which can significantly decrease the diffusion length of Li-ions and prevent the growth of dendritic Li metal.^[132] However, the use of ether-based electrolytes in commercial Li-ion batteries has been discontinued, excluding the use of Li–O₂ and Li–S batteries, due to safety concerns and their narrow working voltage range under 4 V vs. Li⁺/Li.^[128,133–134] When an

ether-based electrolyte is included in a battery with a cathode material that operates above 4 V, the electrolyte is more readily decomposed and diminished, leading to poor capacity retention during prolonged cycling.^[135–137] Thus, because most electrolytes have shortcomings, as mentioned earlier, it is essential to continue to research electrolytes that form stable SEI layers on Li metal anodes covering both types of electrolyte systems mentioned in a range of different batteries.

3. Applications for High-Voltage and High-Energy Batteries

Among the strategies for developing stable Li metal anodes, Li metal interface modification, such as stable artificial layer formation via *in situ* and *ex situ* techniques, is a method that can be used to produce Li metal batteries with a long life span and enhanced safety.^[54] The layers on the surface of Li metal anodes must be homogenous, compact in terms of structure, and possess high mechanical strength and high ionic conductivity, in order to reduce interfacial resistance, prevent electrolyte decomposition, and suppress dendrite formation. There are two ways which develop an artificial layer on a Li metal surface; one is via *in situ* layer formation and the other via *ex situ* layer formation. In the former case, the *in situ* formed artificial layer can be produced using a variety of electrolytes and additives within the working voltage range during cycling and possesses not only better mechanical properties but also chemical stability compared to the native SEI layer. However, the conformation of *in situ* artificial layers is difficult to control in terms of thickness and components, as well as there being no understanding about the reactions that occur in the process. In the latter case, the *ex situ* artificial layer is coated on the surface of Li metal anodes before assembling the battery using more manageable synthesis methods. However, this type of layer can be severely impaired during cycling due to the formation of Li dendrites in a case where the layers are elastic enough and do not have the flexibility to suppress the formation force of dendritic Li, which is more than 6 GPa.^[37,138–139] The damage within the layers causes problems such as continuous dendrite growth and decomposition of electrolyte upon contact with newly exposed Li metal surface in the battery. For each of the approaches mentioned above, there is a trade-off between the advantages and disadvantages, and the obstacles described have not yet entirely been overcome. But, due to the efforts of many researchers who develop Li metal anodes, the *in situ* and *ex situ* formations of artificial layers have recently progressed. From now on, in this section, the recent developmental progress and strategies based on the modification of the surface of Li metal anodes for high-energy-density battery systems as Li–O₂, Li–S, and Li metal batteries containing high-energy-density cathodes will be discussed.

3.1. Li Metal Anodes for Li–Oxygen Batteries

Rechargeable nonaqueous Li–oxygen batteries with Li metal anodes, based on the electrochemical reaction $2\text{Li}^+ + 2\text{e}^- + \text{O}_2 \leftrightarrow \text{Li}_2\text{O}_2$ ($E^\circ = 2.96$ V vs. Li⁺/Li), are one of the highest energy density battery systems, with a theoretical energy density of 3500 Wh kg⁻¹, a value more than ten-fold higher than that of Li-ion batteries.^[140–142] However, unlike Li-ion batteries, the most significant sticking point in the practical application of this system is the problem of the corrosion of the Li metal in the battery due to the O₂ dissolved in the electrolyte and H₂O derived from electrolyte decomposition, even in the absence of discharge/charge processes. Besides this, being in the air, which includes only a small amount of H₂O, can give rise to the very fast corrosion of Li metal to form a layer containing Li carbonate (Li₂CO₃), Li nitride (Li₃N), and Li hydroxide (LiOH).^[143–145] This corrosion brings about some critical problems, such as low reversibility, the accumulation of byproducts, an increase in overpotential, depletion of the electrolyte, the formation of unstable SEI layers, and eventually leads to the premature death of Li–O₂ batteries. Accordingly, besides many studies that have been carried out on the cathode side, such as structural modification, improvements in the catalyst activity, and redox mediator introduction, the development of practical and effective ways to protect Li metal is vital for commercialization of the Li–O₂ battery, while still very challenging.

3.1.1. Bifunctional Additives in Electrolytes: Redox Mediator and SEI Formation

Over the past several years, various strategies have been proposed in the literature to protect Li metal anodes in Li–O₂ batteries. Much effort in this regard has gone into researching artificial layers formed by reactions between the Li metal and electrolytes, such as special Li salts, additives, and solvents.^[128,146–151] The electrolytes of nonaqueous Li–O₂ cells have been studied for several decades. In the early stages of their development, organic carbonates were adopted as electrolytes in Li–O₂ batteries without knowing that they were susceptible to nucleophilic attack by oxygen reduction species, meaning that they were later found to be unsuitable.^[133,152–153] Consequently, ether-based electrolytes, which are appropriate for use with Li metal anodes, have become a substitute solution owing to them having more stability in terms of oxygen reduction species than organic carbonates.^[154–155] Nonetheless, there are still issues with these electrolytes that must be brought into focus, such as their high flammability, high volatility, narrow electrochemical stable range, and parasitic reactions that occur upon cycling.

To address the problems of Li–O₂ batteries along with Li metal anode protection, additives have been employed in ether-based electrolytes. For example, Wang's group suggested a unique additive, a multifunctional tetramethylpiperidinyloxy (TEMPO)-grafted ionic liquid (IL) (Figure 3a).^[156] IL-TEMPO acts as a redox mediator, oxygen shuttle, and Li protector. It contributes toward increasing the discharge capacity by 33–

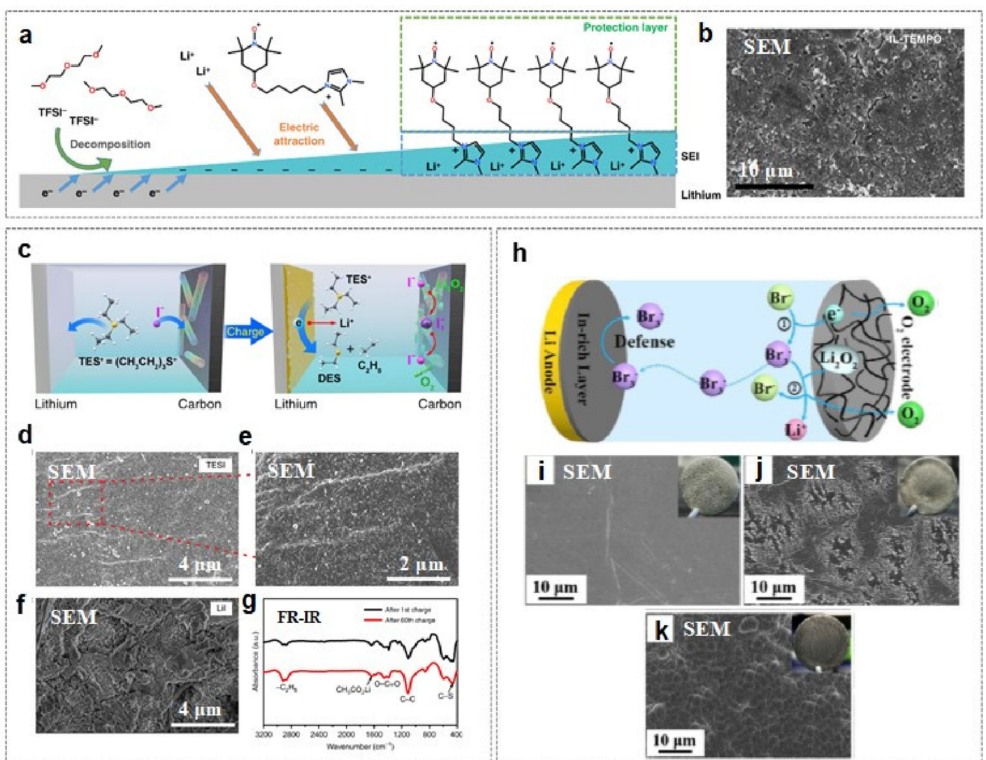


Figure 3. a) Schematic illustration of SEI formation on a Li metal anode in IL-TEMPO electrolyte. b) SEM image of the Li metal anode after 50 cycles in the IL-TEMPO electrolyte. Reproduced with permission.^[156] Copyright 2019, The Authors. c) Schematic illustration of the in situ formation process of a SEI-like layer on a Li anode in the presence of a TESI additive in ether-based electrolyte during the charging process. d–e) SEM images of the Li anode after 60 cycles with 50 mM of TESI additive in the electrolyte. f) SEM image of the pristine Li anode after 30 cycles with 50 mM of LiI additive in the electrolyte. Reproduced with permission.^[157] Copyright 2019, The Authors. h) Schematic illustration of the working mechanism of a InBr_3 additive in a Li–O₂ battery. SEM images of i) the pristine Li metal and Li anode cycled in cells with j) LiBr and k) InBr_3 additives in the electrolyte after 1 cycle at a constant current of 250 mA g⁻¹ with a limited capacity of 1000 mAh g⁻¹. The insets show photographs of the corresponding Li anodes. Reproduced with permission.^[158] Copyright 2019, Elsevier.

fold, decreasing the charge voltage to 3.6 V, and forming stable SEI layers to suppress the growth of Li dendrites and prevent surface corrosion of the Li anode. This phenomenon of protecting the Li metal anode is related to the binding between IL-TEMPO and the SEI layer during cycling. The initial SEI layer originates from the decomposition of LiTFSI and glyme, and then strongly attracts Li-ions and the IL cation in IL-TEMPO due to the negatively charged properties of the SEI layer. The IL cations and Li-ions become securely anchored on the Li metal surface through this process, leading to the stabilization and chemical formation of a SEI layer on the Li metal anode. Furthermore, the TEMPO moiety of IL-TEMPO is arranged side-by-side on the top of the Li metal surface. The n-/p-doping properties of the TEMPO moiety lead to the effective transport of Li-ions owing to the enhancement of the interfacial ionic conductivity of the Li metal anode, resulting in a smooth Li surface and more facial reversible Li stripping and plating (Figure 3b).

Similarly, Zhang et al. developed an effective functional additive for both the cathode and the Li metal anode, triethylsulfonium iodide ($\text{C}_6\text{H}_{15}\text{SI}$, TESI), as shown in Figure 3c, which acts as both an efficient redox mediator and an *in situ* SEI-like layer forming agent on the Li metal anode through reactive ethyl detachment and subsequent oxidation.^[157] When

Li–O₂ batteries use redox mediators to decrease charge polarization, the oxidized redox mediators that diffuse through the separator are reduced at the surface of the Li metal anode upon cycling, which is known as the shuttle effect. Thus, Li metal protection is indispensable for preventing the catalytic activity degradation of redox mediators for long cycling. After TESI dissociates into I⁻ anions and TES⁺ cations in the TEGDEM electrolyte, two phenomena arise simultaneously; one is the oxidation of I⁻ anions at the cathode, and the other is the chemically reductive reaction of TES⁺ cations at the Li metal anode. During charging, I⁻ anions are oxidized to I³⁻ anions, which act as a redox mediator in the electrolyte and decrease the charging overpotential. At the same time, TES⁺ cations deposit on the surface of the Li metal anode, where they are spontaneously chemically reduced upon acquiring an electron due to the antibonding orbitals in the TES⁺ cation. When an electron is received by the lowest unoccupied molecular orbital (LUMO), this occupation promotes the detachment of the ethyl group from TES⁺ to form diethyl sulfide ($\text{C}_4\text{H}_{10}\text{S}$, DES) and an ethyl radical. Consequently, the resulting surface layer not only consists of inorganic components, such as Li_2CO_3 , Li_2O , and Li_2S , but also organic components, such as DES and $\text{CH}_3\text{CO}_2\text{Li}$. The organic components in the SEI layer on the Li metal anode play an important role in transferring Li-ions and blocking the attack

of soluble redox mediators. Scanning electron microscopy (SEM) images of the Li metal anode in the TESI-containing Li–O₂ battery after 60 cycles show a thin fluffy layer, while the other in the LiI containing electrolyte does not have this appearance (Figure 3d–f). The Fourier-transfer infrared (FT-IR) spectra of the protective Li metal anode show similar results after 1 and 60 cycles, indicating that the layer on the Li metal is stable and robust enough to defend it against attacks from O₂ or H₂O during prolonged cycling, as shown in Figure 3g.

In a recent study, InBr₃ was proposed by Liu et al. as a “self-defense” redox mediator, as shown in Figure 3h.^[158] Similar to LiI and LiBr as ordinary redox mediators, the redox couple of Br^{3−}/Br[−] during cycling is beneficial for lowering the polarization and thus enhancing the lifespan of the Li–O₂ battery by up to more than 206 cycles with a limited capacity of 1000 mAh g^{−1}. Due to the presence of In³⁺ cations in the electrolyte, an In-rich composite protective layer can be *in situ* generated on the Li metal anode, which contributes toward suppressing redox shuttling, improving the interfacial stability of the Li metal anode, and preventing dendritic Li growth (Figure 3i–k).

3.1.2. Hybrid Protection Layer Formed via an In Situ Process

Generally, when a Li metal anode is used in Li–O₂ batteries, the very harsh environment quickly leads to the deterioration on the Li metal anode to form detrimental corrosion products such as LiOH and Li₂CO₃. The decay of the Li metal anode is inevitable over time, in both the presence and absence of current flow. Hence, Li metal anodes definitely need a stable protection layer under an oxygen atmosphere, as well as the capability to allow smooth Li-ion diffusion even at a thickness of several micrometers.^[159]

Zhu et al. developed an organic-inorganic hybrid layer (OIHL) to cover a Li metal anode using a facile and practical approach.^[160] This desirable OIHL is directly formed on the Li metal surface via the reaction of surface Li metal, 1-chlorodecane, and mixed O₂/carbon dioxide (CO₂) gas to generate RCO₃Li. Then, during cycling under an O₂/CO₂ atmosphere, the RCO₃Li with long hydrophobic carbon chains intertwines and wraps the LiCl particles to form a protective layer on the Li metal surface, with a thickness of 30 μm, as shown in Figure 4a–b. The Li–O₂ batteries with an OIHL protected Li metal anode exhibit a cycle life of up to 340 cycles with small voltage deviations, indicating excellent cycling performance, as shown in Figure 4c.

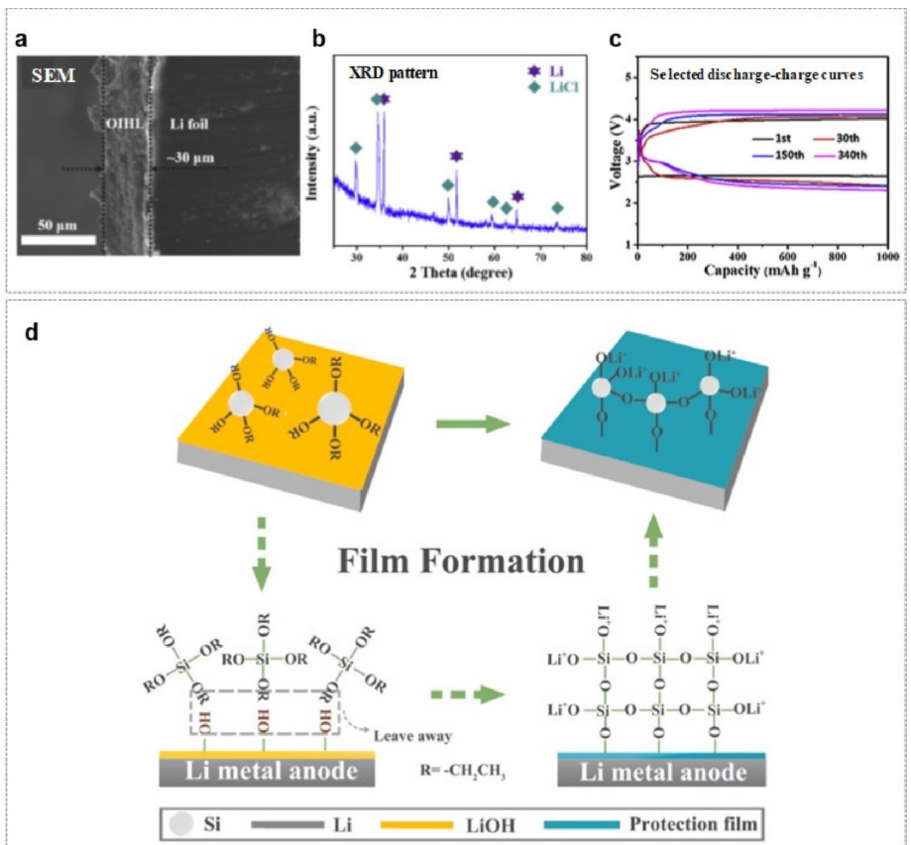


Figure 4. a) Cross-section SEM image and b) XRD patterns of OIHL–Li foil with a thickness of ~30 μm. c) Selected discharge-charge voltage profiles of Li–O₂ cells with an OIHL–Li film anode from the 1st to the 340th cycle at a fixed capacity of 1000 mAh g^{−1} and a current density of 500 mAg^{−1} based on the CNT weight. Reproduced with permission.^[160] Copyright 2017, Elsevier. d) Schematic illustration of the Li protection film formation mechanism on the TAL in the Li–O₂ battery. Reproduced with permission.^[161] Copyright 2019, Elsevier.

Similarly, as shown in Figure 4d, Yu et al. reported a facile and highly efficient strategy for the *in situ* growth of a self-healing protective film on a Li metal anode, wherein tetraethyl orthosilicate (TEOS) plays a key role as a novel film-forming electrolyte additive.^[161] In this system, the corrosive product LiOH aids in the *in situ* film formation process, which reacts with the TEOS electrolyte additive via a non-hydrolytic sol-gel method. LiOH reacts with TEOS, forming a thin layer of Li silicate. Finally, SiO₂ builds upon the Li metal surface as a result of the continuous reaction of the LiOH and TEOS. The protective layer, including polymeric SiO_x compounds, has self-healing properties due to the reaction between TEOS and LiOH, which help to dynamically repair the film, thus improving the electrochemical performance (up to 144 cycles with a limited capacity of 1000 mAh g⁻¹) and the reversibility of the Li metal anode.

3.1.3. Hybrid Protection Layer Formed in an Ex Situ Process

An ideal protective layer on a Li metal anode in a Li–O₂ battery should be mechanically robust enough to prevent dendrite penetration, be electrochemically stable to ensure long-term cycling, and in particular, be H₂O impermeable to defend against attack from H₂O. In these regards, inorganic materials are a good option due to their mechanical and electrochemical properties, but are fragile under stress in the process of dendritic Li growth during cycling. Thus, the combination of organic and inorganic materials is necessary to accommodate volume changes that arise during Li stripping/plating.

As shown in Figure 5a, Lee et al. suggested a composite protective layer (CPL) comprising Al₂O₃ and polyvinylidene fluoride-hexafluoropropylene (PVDF-HFP). Al₂O₃ was introduced to provide the material with sufficient mechanical strength and PVDF-HFP to promote fast Li-ion transport through the CPL by forming a gel-polymer electrolyte with the liquid electrolyte.^[162] A CPL with a thickness of 20 μm was prepared using a doctor blade coating of a slurry in a weight ratio of 4:1 (Al₂O₃:PVDF-HFP) on the Li metal surface. The introduction of the CPL resulted in an enhancement of the lifespan up to 80 cycles, which is two-fold longer than for bare Li metal, with a fixed capacity of 1000 mAh g⁻¹, as shown in Figure 5b. Moreover, after two years, Lee's research group also reported a new capability for CPL, in that it can suppress the shuttle effect of the oxidized redox mediator. A Li–O₂ battery featuring a CPL-Li anode exhibited stable cycling up to 100 cycles and reduced charging overpotential up to 175 cycles.^[163] This was the first study where it was reported that anode protection helps to maintain redox mediation.

Similarly, Liao et al. reported a composite layer featuring amorphous germanium (Ge, GeO_x) and Li compounds (Li₂CO₃, LiOH, Li₂O, LiCl) in their development of water-defendable and dendrite-free Li metal anodes, as shown in Figure 5c.^[164] Their facile Li metal pretreatment methodology is based on a simple galvanic replacement reaction (4Li + GeCl₄ → Ge + 4LiCl) because Ge has a more positive equilibrium potential than Li, which leads to the spontaneous formation of Ge on the Li metal surface (Figure 5d–f). This represents a simple and industrially applicable method that can be used to create a dense and uniform 1.5 μm thick CPL on the Li metal surface. Its

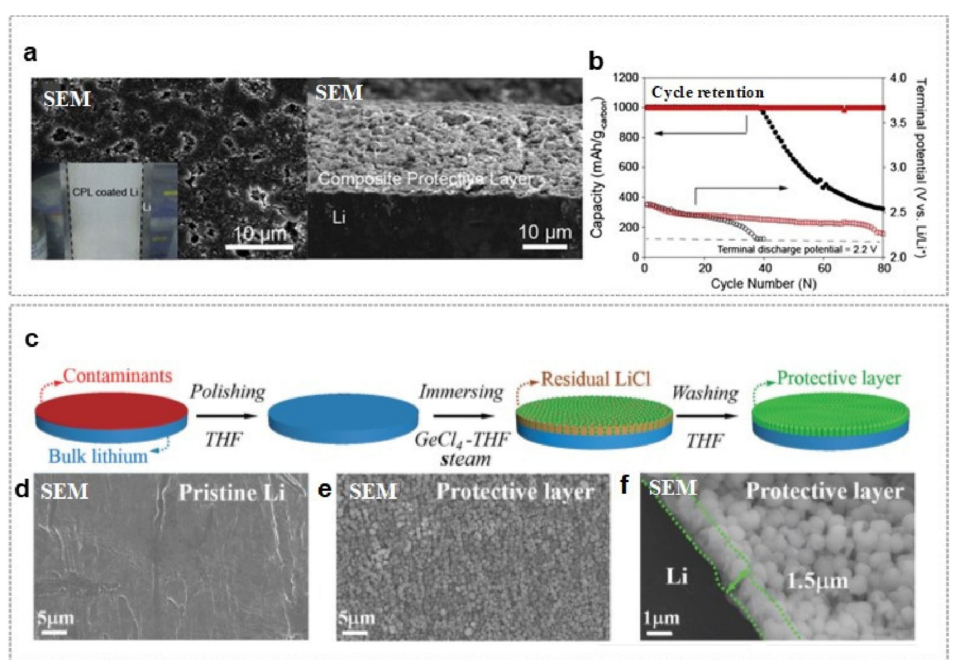


Figure 5. a) SEM images of the surface (left) and cross-sectional morphology (right) of a Li electrode with a CPL layer, where the inset shows a photo of the corresponding Li anode with a CPL layer. b) Cycling performance and potential profiles of Li–O₂ batteries of a pristine Li electrode (black color) and CPL/Li electrode (red color). Reproduced with permission.^[162] Copyright 2014 Elsevier. c) Schematic illustration of the formation sequence of a protected Li electrode. SEM images of the d) pristine Li surface, e) protected Li surface, and the f) edge of the protected Li. Reproduced with permission.^[164] Copyright 2018 Wiley-VCH.

capability of blocking attacks from H_2O and O_2 was proven in an experiment where it was immersed in H_2O -containing electrolytes of various concentrations for one hour. In humid O_2 gas (room humidity of 45%), a Li– O_2 battery with the Ge-based protective layer exhibited stable cycling performance over 150 cycles with low charge polarization, while the untreated Li metal anode showed capacity retention up to 25 cycles.

3.2. Lithium Metal Anodes for Lithium-Sulfur Batteries

A lithium-sulfur battery is one of the next-generation battery systems that uses lithium metal as an anode. The lithium-sulfur battery has a theoretical energy density of about $\sim 2500 \text{ Wh kg}^{-1}$ or 2800 Wh L^{-1} , which is five-fold higher than that of commercial lithium battery systems.^[162,165–168] Furthermore, from an economic point-of-view, the lithium-sulfur battery is fascinating enough to supplement traditional lithium-ion batteries due to the low costs of sulfur, which is highly abundant and easy to recycle.^[169] Thus, this system would be able to satisfy the energy demands of advanced EV and energy storage systems. However, there are problems with all of the components of lithium-sulfur batteries, such as the sulfur cathode, lithium metal anode, and the electrolyte. In particular, with the use of lithium metal anodes in lithium-sulfur batteries, there is a unique problem in that the lithium anode is attacked by polysulfide anions that are transported from the sulfur cathode due to the shuttle effect.^[170] The polysulfide anions react with lithium metal to form $\text{Li}_2\text{S}/\text{Li}_2\text{S}_2$ and then accrue on the lithium metal surface in the form of insulating layers.^[21,171] This process continues during cycling, resulting in critical problems such as the formation of unstable thick SEI layers, depletion of the electrolyte, and deactivation of the lithium metal anode.^[170] Therefore, it is essential to protect the lithium metal surface from being attacked by polysulfide anions, while dealing with the polysulfide dissolution problem at the cathode.

3.2.1. Ex Situ-Formed Artificial SEI Layers: Enhancement of Li-Ionic flux

To enhance the stability of lithium metal anodes, methods have been introduced to protect the Li metal by constructing an artificial SEI layer using an *ex situ* method consisted of organic or inorganic materials.^[47,172–178] *Ex situ* SEI layer formation refers to the pre-forming of an artificial SEI layer on the lithium metal surface before assembling the cell.

The artificial layer should have high mechanical modulus, chemical stability, ionic conductivity, and poor electrical conductivity. However, problems such as mechanical defects, poor interfacial contact with Li metal, and limiting the coating area must be solved to get closer to commercialization. The development of a homogeneous coating technique for forming artificial layers is critical because if the coating layer is unevenly formed and has defects, safety problems can arise. As shown in Figure 6a, Wang's group suggested a lithium phosphorus

oxynitride (LiPON) coating layer, formed nitrogen plasma-assisted deposition of electron-beam reacting evaporation.^[179] The developed LiPON layer is a dense, interfacial stable, mechanically robust, has high ionic conductivity, and can cover the lithium metal on a large scale. To understand the electrochemical properties, electrochemical impedance spectroscopy measurements and calculations were carried out, which revealed that the LiPON coating layer shows high ionic conductivity as a passivation layer, as well as excellent mechanical properties. SEM images showed that lithium metal with the LiPON coating layer is smoother and more uniform than a pristine lithium metal anode after 10 cycles, indicating that the protective layer is well protected against polysulfide attack (Figure 6b).

Liu's group introduced a metallic Sn layer on Li metal anode by the thermal evaporation method.^[178] The Sn layer was selected by its several valuable properties, such as electrochemical reactivity, low cost, and high stability with Li salts. In electrochemical tests, the Li metal anode with the Sn layer exhibited excellent result of symmetric batteries with stable cyclability and low voltage polarization up to 400 cycles at 1 mA cm^{-2} , compared with bare Li shorted after ~ 200 cycles. This layer was effective for suppressing Li dendrites, as well as inhibiting the side reactions of Li metal with an electrolyte or polysulfide (Figure 6c). The research group suggested two reasons why the cell with the Sn layer is guaranteeing high electrical performance. One is that the layer is blocking the side reactions between Li metal and the electrolyte, which lead to preventing the undesirable SEI formation and facilitating the Li-ions transports. The other is the excellent Li diffusion ability of the Sn proved by a low migration energy barrier calculated by DFT simulation (Figure 6d–e).

In Figure 6f, Robert et al. reported a fluorinated reduced graphene oxide (FG) layer via drop-casting FG on Li metal from the dispersion in propylene carbonate.^[180] The protective layer is supposed to have high mechanical strength and high ionic conductivity. The obtained Li metal with the FG layer maintained for 600 h with a slow increase of voltage polarization during cycling (Figure 6g). The results were caused by the FG layer that it is not only controlling Li morphology during cycling but also enhancing a Li-ion flux by forming LiF on the SEI layer.

3.2.2. In Situ-Formed Artificial SEI Layers

As mentioned, *in situ* SEI layer formation has also been introduced as a method to protect lithium metal surfaces.^[181–182] Presented that *in situ* inorganic SEI layers can be formed by adding inorganic additives to protect the Li-metal anode and simultaneously enhance electrochemical performance (Figure 7a).^[183] SOCl_2 , when used as an additive, reacts with lithium in the following way $8\text{Li} + 3\text{SOCl}_2 \rightarrow 6\text{LiCl} + \text{Li}_2\text{SO}_3 + 2\text{S}$ to synthesize a SEI layer containing LiCl. The LiCl-rich film prevents the continuous decomposition of electrolyte, inhibiting dendritic lithium growth, and improving the electrochemical performance by preventing pulverization of the lithium metal

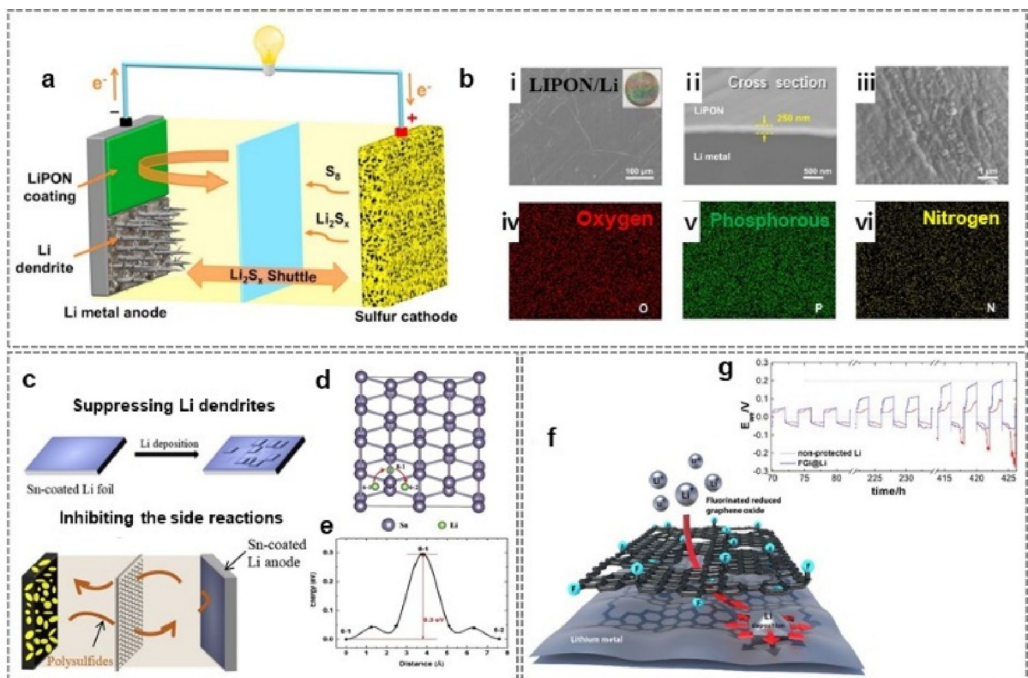


Figure 6. a) Schematic illustration of the ability of a LiPON-coated lithium metal anode in the lithium-sulfur battery. b) SEM and elemental mapping images of the LiPON-coated lithium metal anode, (i) the surface, (ii) cross-section, and (iii) high-resolution SEM images. (The insert is the photos of the corresponding lithium anodes with the LiPON layer.) The elemental mapping images of (iv) Oxygen, (v) Phosphorous, and (vi) Nitrogen by EDS. Reproduced with permission.^[179] Copyright 2019 Elsevier. c) Mechanism of improved electrochemical performance for Li metal anode by Sn coating. d) Li interstitial diffusion path, and e) corresponding migration energy barrier in Sn layer. Those are calculated by DFT simulation of Li interstitial migration through Sn bulk. Reproduced with permission.^[178] Copyright 2020 Elsevier. f) Schematic illustration of Li-ion penetration through the FGL and Li deposition onto lithium surface underneath the FGL. g) Voltage versus time curves for Li-symmetrical cells and schematics of lithium deposition on FGL@Li. Reproduced with permission.^[180] Copyright 2018, The Authors.

anode. At the same time, the sulfur in SOCl_2 acts as a redox additive, resulting in an enhancement in the capacity of the lithium-sulfur battery. To understand the SEI layer properties in more detail, the components of the SEI layer were confirmed through X-ray photoelectron spectroscopy (XPS), as shown in Figure 7b. Moreover, Figure 7c shows SEM images of Li-metal surfaces with and without the additive in symmetric cells after 100 cycles. The results indicate that the SEI layer driven by the SOCl_2 additive helps to stabilize the lithium metal anode, leading to the good electrochemical performance of the lithium-sulfur battery.

In addition, there is another reason for using an additive in an electrolyte. Wang's group used special additives to suppress the flammability and improve the stability of high electrochemical performance Li–S batteries.^[184] They selected numerous phosphate solvents such as triethyl phosphate and trimethyl phosphate (TMP), which are known as efficient flame retardant electrolytes. Then, they reported the use of lithium bis(fluorosulfonyl)imide (LiFSI) in a mixture of TMP and 1,1,2,2-tetrafluoroethyl 2,2,3,3-tetrafluoropropyl ether (HFE) to enhance both the non-flammability and cycling ability of a battery. According to the reported literature, TMP-3HFE (1:3, corresponding to TMP/HFE volume ratio) with 1.6 M lithium bis(fluorosulfonyl) (LiFSI) was used as an electrolyte to ensure good performance and safety. Furthermore, the electrolyte added to TMP-HFE resulted in promoted ionic conductivity (1.36 mS cm^{-1}) and wettability, and viscosity reduction of the

whole electrolyte. To confirm the major components of the SEI layers, XPS was used. In the SEM images shown in Figure 7d–f, different lithium morphologies can be observed in the presence and absence of electrolyte additive on a Cu current collector at a current density of 0.2 mA cm^{-2} with an area capacity of 0.4 mAh cm^{-2} , where it can be seen that the TMP-based electrolyte has a smoother lithium deposit than the conventional carbonate electrolyte. Lithium metal stability in the battery was proved through the cycling performance of Li//Cu asymmetric cells at a current density of 0.2 mA cm^{-2} . The performance of the conventional carbonate electrolyte showed rapid decline after 80 cycles, while the 1.3 M LiFSI/TMP-3HFE electrolyte showed high stability with average efficiency of up to 99.1% over 550 cycles, as shown in Figure 7g.

3.2.3. Controlling the Lithium Metal Surface: Chemical Components and Structure

Research has also been conducted to improve lithium metal stability during plating and stripping processes by controlling the lithium metal surface in terms of chemical components and structure.^[185–187] Kong's research group suggested that a Li-rich lithium-magnesium (Li–Mg) alloy forms a MgO-containing passivation layer on a Li–Mg alloy surface during reaction with lithium in the cell.^[188] The study was based on the difference in exchange current density between Mg (0.81 mA cm^{-2}) and Li

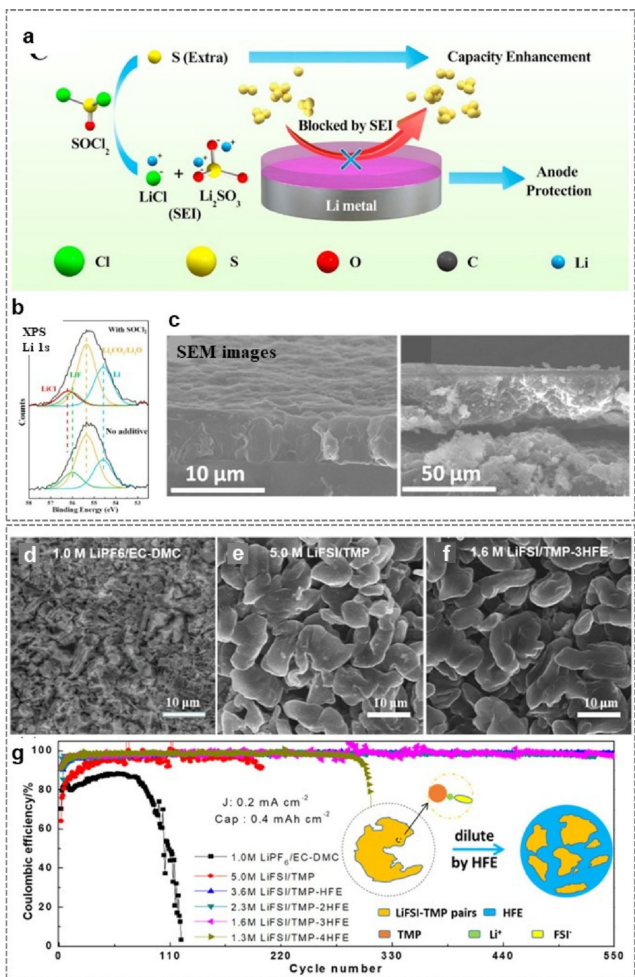


Figure 7. a) Schematic illustration of anode protection and capacity enhancement mechanisms upon adding SOCl_2 to the electrolyte in a Li–S battery. b) XPS spectra of Li metal anodes without (bottom) and with (top) the additive after 100 cycles at a current density of 400 mA g^{-1} . c) SEM images of Li metal surfaces in symmetric cells after 100 cycles using electrolytes with (left) and without (right) the SOCl_2 additive. Reproduced with permission.^[183] Copyright 2019 Elsevier. SEM images of the plated Li morphology on Cu electrodes at a current density of 0.2 mA cm^{-2} with an areal capacity of 0.4 mAh cm^{-2} in various electrolytes; d) $1.0 \text{ M LiPF}_6/\text{EC-DMC}$ (1:1), e) 5.0 M LiFSI/TMP , and f) $1.6 \text{ M LiFSI/TMP-HFE}$ (1:3). g) Coulombic efficiency during the Li plating/stripping process in asymmetric cells with Li/Cu electrodes, at a current density of 0.2 mA cm^{-2} with an areal capacity of 0.4 mAh cm^{-2} . Reproduced with permission.^[184] Copyright 2019, American Chemical Society.

(1.51 mA cm^{-2}). In addition, physical properties such as the high melting temperature of 206°C and less absorbed heat (479.9 J g^{-1}) are also better than for the lithium metal anode, resulting in the thermal stability of the battery. Moreover, these good properties can influence the morphology of lithium during the plating/stripping process, as shown in Figure 8a. The SEM images show that the Li–Mg alloy can adopt a more stable morphology. After Li stripping, the Li poor–Mg rich alloy acts as a current collector in the porous structure and helps to recover a flat and clean surface. As shown in Figure 8b, EDS results show that sulfur was detected in the bare lithium metal anode, while it was not observed in the Li–Mg alloy anode, indicating that the Li–Mg alloy protects the lithium metal

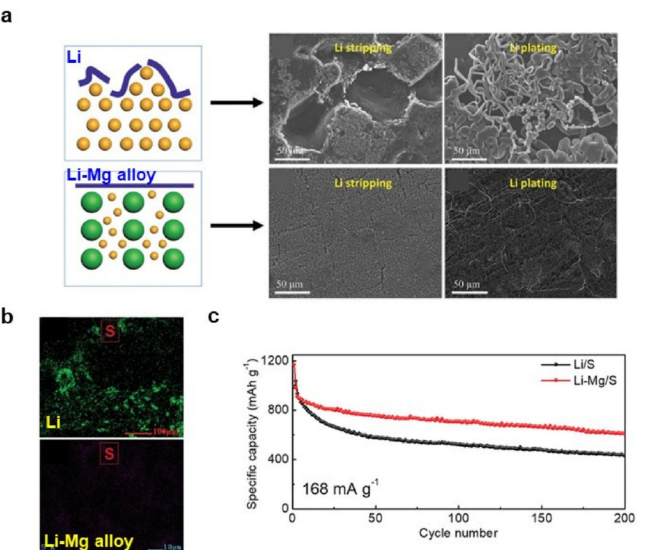


Figure 8. a) SEM images of Li (top row) and a Li–Mg alloy (bottom row) after a Li plating/stripping process at 0.5 mA cm^{-2} for 24 h. b) Elemental distribution of sulfur at Li (top) and Li–Mg alloy (bottom) electrodes retrieved from the cells after 100 cycles. c) Cycle retention of Li–S batteries using Li (black) and Li–Mg alloy (red) anodes at a current density of 168 mA g^{-1} over 200 cycles. Reproduced with permission.^[188] Copyright 2019 Wiley-VCH.

anode against the leaching of soluble sulfur species from the sulfur cathode. Based on these advantages, Figure 8c shows that the long-term cycling stability of the battery with the Li–Mg alloy anode maintains a stable capacity of 607 mAh g^{-1} over 200 cycles, but over the same number of cycles, the Li–S cell with the pristine lithium metal anode delivers a capacity of only 433.6 mAh g^{-1} .

A Li–metal anode can also be protected through the use of a 3D structure current collector because lithium dendrite growth arises as a result of uneven local current density during plating and stripping processes.^[189] Designing a current collector with a 3D structure and good electrical conductivity allows Li deposits to be captured, resulting in the stability of a cell being maintained during cycling.^[190] However, the 3D structure is required to solve problems such as low areal capacities, heavyweight, and complex manufacturing procedures.^[191] Figure 9a shows the results of a study by Zheng's research group where to improve the lithium metal stability in a lithium–S battery, metal foams wrapped with yolk–shell structured N-doped porous carbon nanosheets (M@NPCN) was developed.^[192] In a cell containing M@NPCN as a current collector on the lithium metal anode, there are two advantages; one is that the surface area of the anode is increased, and the other is that yolk–shell structured NPCN has a high content of N and O, resulting in an improvement in the wettability and lithiophilicity of the lithium ions. Previously they developed N-doped hollow carbon bowls (NHCBs) as a sulfur hosting material, which helped to improve the electrochemical performance of the full cell containing NHCB/S (Figure 9b) with 85 wt% sulfur in the host materials. In addition, in a long-term

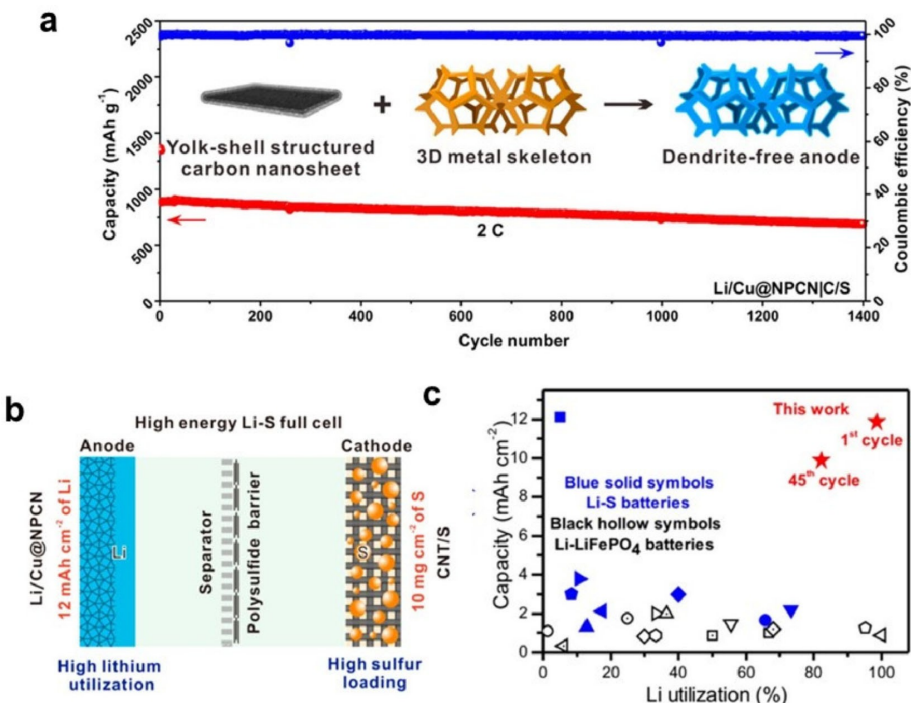


Figure 9. a) Cycling performance of Li–S batteries using designed NPCN-wrapped 3D metal foam as the current collector, where the inset shows a schematic illustration of the designed NPCN-wrapped 3D metal foam. b) Schematic illustration of the fabrication of a high-sulfur loaded Li–S full cell using the designed NPCN-wrapped 3D metal foam. c) Comparative analysis of the Li areal capacities and Li utilizations of the Li/Cu@NPCN|CNT/S cell with those of reported Li–metal batteries (the Li utilizations and Li areal capacities were chosen from the first cycles). Reproduced with permission.^[192] Copyright 2019, American Chemical Society.

cycling experiment, the cell exhibited excellent cycling retention of around 78.1% over 1400 cycles (Figure 9c).

Similarly, the Li–metal anode can be conductively controlled, where an artificial layer is used to improve the efficiency of the Li–S battery. Zhao’s research team used a conductive

material to introduce pores into a Li–metal surface and a stable artificial layer to effectively suppress the shuttle effect (Figure 10a).^[193] As can be seen in Figure 10a, carbon nanofiber matrix (CNF) treated sulfur increases the conductivity and porosity of the electrode. When molten Li metal is spilled,

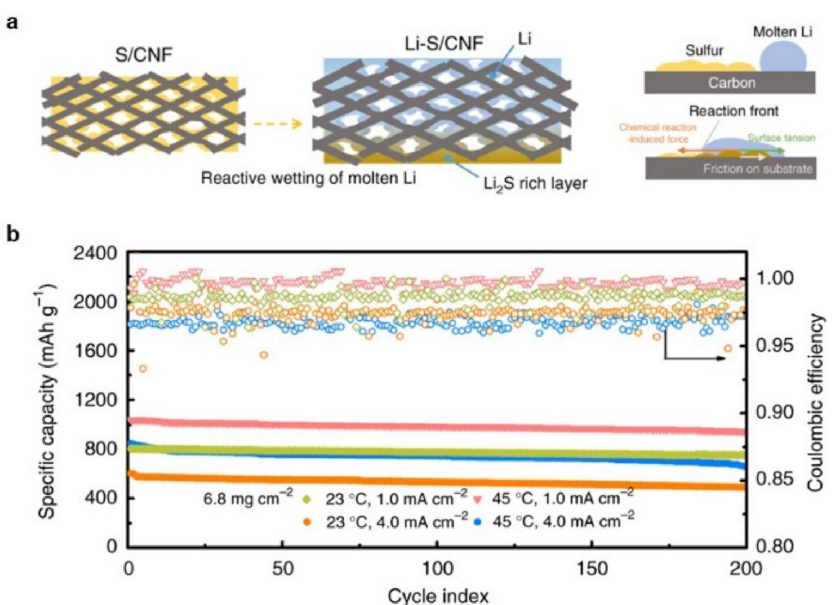


Figure 10. a) Schematic illustration of the fabrication process of a Li–S/CNF electrode. b) Cycling performance of Li–S batteries containing Li–S/CNF electrodes with a sulfur loading of 6.8 mg cm⁻² at current densities of 1.0 or 4.0 mA cm⁻² at 23 or 45 °C. Reproduced with permission.^[193] Copyright 2019, The Authors.

CNF–Li is formed in an exothermic reaction, presenting stable lithium deposition. Then, $\text{BiF}_3\text{-P}_2\text{S}_5$ was coated to CNF–Li to induce spontaneous reactions to form a SEI layer composed of LiF and Li_3Bi , which is called as metal fluoride complex (MFC–Li/CNF). Along with the LiF layer, which is known as a good passivation layer,^[194] Li_3Bi has a high Young's modulus of 22.20 GPa compared to the 1 GPa value for lithium metal, and it can inhibit growth of lithium dendrites and strongly interconnect with LiF, resulting in the cell having a high ionic conductivity of $\sim 6.9 \times 10^{-1} \text{ S cm}^{-1}$ compared to the value when there is only a LiF layer of $\sim 10^{-12} \text{ S cm}^{-1}$. Furthermore, the lithium-S full cell shows the stable electrochemical performance of MFC–Li/CNF, which is maintained over 200 cycles at a high-sulfur loading of 6.0 mA cm^{-2} , as shown in Figure 10b.

3.3. Li Metal Anodes with High-Capacity Cathode Materials for Li Metal Batteries

Since the commercialization of Li-ion batteries in 1991, for a long while, many research studies in the battery field focused on the development of high-capacity cathode materials, because there was no other way to replace the graphite anode. In particular, LiCoO_2 (LCO) with a high working voltage and its transition metal oxide successors such as $\text{LiNi}_{0.8}\text{Co}_{0.15}\text{Al}_{0.05}\text{O}_2$ (NCA) and $\text{LiNi}_x\text{Mn}_y\text{Co}_z\text{O}_2$ (NMC_{xyz} where $x+y+z=1$) coupled with carbon anodes had been shown to be incredibly successful.^[195–199] However, there was still the limitation to improving the energy density levels of Li-ion batteries using a graphite anode.^[200] For example, most pure EV use Li-ion batteries based on an NMC cathode and graphite anode, and can run only a maximum of 300 miles on a single charge, even though the battery is more than a quarter of the vehicle weight.^[9] Thus, one solution to the advanced transition metal oxide cathode/graphite anode paradigm is to replace the graphite anode with a Li metal anode.

3.3.1. Artificial Layers Driven by Electrolyte Component Decomposition

The formation of the SEI layer occurs when the redox potential of the electrodes used in a battery lie outside the electrochemical window of the electrolyte.^[123,201–202] When the LUMO of the electrolyte is higher than the Fermi energy of the anode, the electrolyte is stable in the battery. Otherwise, it is possible for the electrolyte to be reduced. The LUMO of most anodes, such as silicon ($\sim 0.4 \text{ V vs. Li/Li}^+$), graphite ($\sim 0.1 \text{ V vs. Li/Li}^+$), and Li metal (0 V vs. Li/Li^+), is lower than those of electrolytes, leading to electrolyte reduction on the anode surface. An ideal nanometer-thickness SEI layer allows Li-ion transport and blocks electrons from the anode, thus preventing further electrolyte decomposition. Unfortunately, real SEI layers are mechanically unstable under the massive volume expansion of anodes and become more heterogeneous in structure upon electrolyte consumption. Hence, one solution to this is to design a stable SEI layer by altering the electrolyte components

and using additives to enable the practical functioning of Li metal anodes in advanced Li metal batteries.

The principles of this approach are based on the reduction potential differences between the electrolyte elements during cycling. Select chemicals with a high reduction potential form a stable SEI layer on the Li metal before electrolyte decomposition, preventing the formation of unstable SEI layers during further cycling. In a recent study, Yoo et al. suggested aromatic compounds with different functional groups as electrolyte solvents for the formation of a stable SEI layer in carbonate-based Li metal batteries.^[203] To form a uniform and rigid SEI layer on the Li metal, the study used the bonding characteristics of benzene rings that do lead to polymeric branch structures in polymerization after initiating itself due to being three double bonds resonance. In addition, three different aromatic compounds, benzene (Ben), toluene (Tol), and trifluorotoluene (Tof), were chosen for the study because the electron density determined by the functional group attached to the benzene group was found to influence the polymerization, as shown in Figure 11a. Among the electrolytes, including selected aromatic compounds, the electrolyte with toluene that has a methyl group, which is an electron-donating group, showed the best overall performance in terms of high reduction potential (Figure 11b). In addition, it also shows the good observed round-shaped Li and the full cell performance with a NMC532 electrode in a carbonated-based electrolyte. Furthermore, the toluene polymerization process induced the uniform distribution of LiF on the Li metal surface.

Fluoroethylene carbonate (FEC) is one of the most attractive electrolyte components and has gained interest as a promising electrolyte additive for improved SEI passivation on Si- and Sn-based anodes.^[204–207] Recently, many research studies have used FEC as an electrolyte additive on Li metal anodes for enhancing the high round efficiency and capacity retention due to the LiF formed from the decomposition of FEC.^[40,208–212] Among the recently reported studies in the literature, Yan et al. presented a new approach via a chemical reaction between FEC and a Li metal surface, as shown in Figure 11c, with the aim of facilitating the formation of a dual-layered film divided into an inorganic part at the bottom with an organic part on the top.^[213] When the Li metal anode is immersed in only an FEC solution, first the F anions detached as a result of the reduction of FEC due to weak bonding between C and F, and combined with Li to form Li–F bonds. Subsequently, the organic components also simultaneously formed $\text{CH}_3\text{CHOCO}_2\text{Li}$ and CH_2CHOLi on the Li metal anode surface. Over time, the organic components (ROLi and ROCO_2Li) tend to reinforce the outer part and the inorganic components (Li_2CO_3 and LiF) the inner part of the dual-layered interface structure. AFM topography images show that this dual-layer is 25–50 nm thick with a Young's modulus of 0.6 GPa for the top layer and 7.0 GPa for the bottom layer. The organic layer contributes good flexibility to prevent cracks, and the inorganic layer containing Li_2CO_3 and LiF, orders nucleation sites and suppresses the formation of Li dendrites. Moreover, electrochemical tests were carried out on a protected Li metal anode coupled with a NMC532

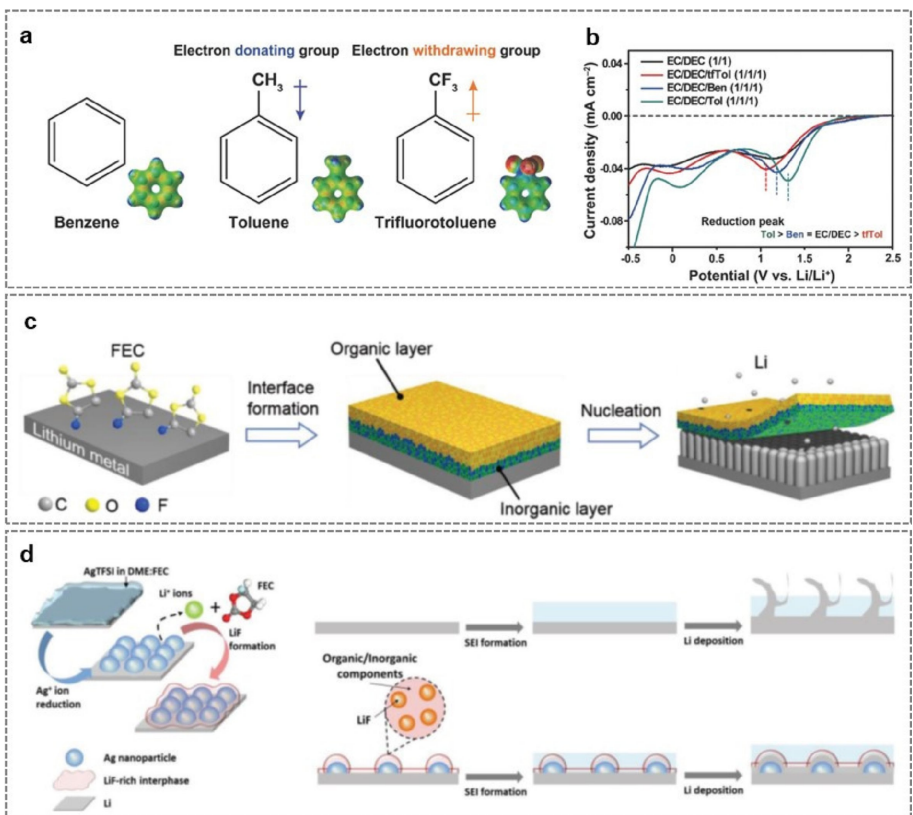


Figure 11. a) Molecular structures of benzene (Ben), toluene (Tol), and trifluorotoluene (tfTol) with their electron-donating/withdrawing character denoted. b) Linear sweep voltammetry curves of three EC/DEC electrolytes containing Ben, Tol, and tfTol in addition to standard EC/DEC (1/1, V/V%). Reproduced with permission.^[203] Copyright 2019, Wiley-VCH. c) Schematic illustration of a dual-layered film formation sequence on a Li metal anode through FEC treatments. Reproduced with permission.^[213] Copyright 2018, Wiley-VCH. d) Schematic representation of the formation of a Li–Ag–LiF surface and the synergistic control of nucleation and SEI for Li plating. Reproduced with permission.^[214] Copyright 2019, Wiley-VCH.

electrode in a full cell. The shielded Li metal electrode delivered superior capacity retention of 68.2% up to 120 cycles.

Similarly, as shown in Figure 11d, Peng et al. fabricated a Li–Ag–LiF decorated Li metal anode via a soaking treatment in an Ag⁺ ion precursor solution.^[214] The principles behind the formation of the layer on the Li metal anode is based on ion exchange chemistry, forming Li alloys such as Sn, Mo, and Li, and has proven to be a useful and facile approach by which to stabilize Li metal during cycling. The Ag⁺ precursor solution consists of silver bis(trifluoromethanesulfonic) imide (AgTFSI) in a mixed DEC and FEC solvent. The ternary coating layer is spontaneously formed by immersing the metal in the solvent solution for a short time. Also, based on the significant difference in the reduction potentials (DME: 0.6–0.7 V, FEC: 1.1–1.2 V, Ag: ~3.84 V vs. Li/Li⁺), it is expected that the reduction sequence begins with Ag⁺ ion reduction. Then, DME and FEC reduction occur, followed by the release of Li-ions to form an organic-inorganic mixed surface with embedded LiF surrounding the Ag nanoparticles. Thus, the Li–Ag–LiF layer with a thickness of ~7 μm was assembled into a composite of Ag nanoparticles and a LiF matrix on the Li metal surface. In this system, the Ag nanoparticles act as a Li nucleation site with significantly lower overpotential, and the LiF-rich interphase improves the ion transfer kinetics to enable fast Li-ion diffusion across the interlayer even at a high-current density of

5 mAh cm⁻² in the symmetric cell. Furthermore, the novel Li–Ag–LiF/Li anode coupled with a NMC333 electrode (loading: 1.8 mAh cm⁻²) in a carbonate-based electrolyte demonstrated a cycling life of more than 500 cycles with a capacity retention of above 80%.

3.3.2. Polymeric Protection Layers: Single-Ion Conducting Properties

A single-ion conductor (ionomer) that has non-conducting ions bound to a polymer backbone conducting only one type of ions without any electrical conductivity. Single-ion conductors can be facilitated by dry polymer electrolytes, gel-polymer electrolytes, and so on.^[215–219] The mechanism of the migration of Li-ions in a single-ion conductor occurs via the hopping of Li-ions as electron-pair acceptors (Lewis acid) around the anions acting as electron-pair donors (Lewis base). The anions are anchored by covalent linking to a polymer backbone or side chains on the constituents of macromolecule repeating units. Accordingly, these materials have high Li-ion transference numbers ($0.8 < t_{Li^+} < 1$), even at a low ionic conductivity ($10^{-8} \sim 10^{-7}$ Scm⁻¹), resulting in the uniform movement of Li-ions.^[220–221] Therefore, there are many researchers using the

single-ion conducting concept for developing an interfacial contact layer.

Bao's research group prepared an artificial SEI layer for a stable Li metal battery based on a single-ion conducting principle.^[222] For the first time, they reported a dynamic single-ion conductive network (DSN), incorporating all of the desirable properties, such as fast ion transport, conformal protection, and parasitic reaction prevention, as shown in Figure 12a–b. In this network, tetrahedral Al(OR)^{4−} (R=soft fluorinated linker) anions are used as a dynamic motif while providing counter anions for Li-ions. Soft fluorinated chains (1H,1H,11H,11H-perfluoro-3,6,9-trioxaundecane-1,11-diol, FTEG) were chosen as an inactive ligand. FTEG is less chemically reactive, more solvent resistant, and helping the transport of Li-ions. The single-ion conducting properties of the DSN were confirmed by ion conductivity via electrochemical impedance spectroscopy and Li-ion transference number via potentiostatic polarization in Li/Li symmetric cells. The high Li-ion conductivity and high Li transference number of the DNS helped to increase the critical Li nucleate size, enable smooth Li deposition, and reduce the untoward reactions between the anions and Li metal, as described in previous literature. For the electrochemical testing of full cells, the DSN protection layer was applied to Li metal (thickness of 42 μm, areal capacity of ~8 mAh cm⁻²) using a dip-coating method, and this was then assembled in a battery together with a NMC532 electrode. The DSN Li/NMC532 full cell shows a much-improved capacity retention of ~85% after 160 cycles with a higher average coulombic efficiency of 99.6% compared to the bare Li battery.

Similarly, as shown in Figure 12c, Archer's group introduced an ionomer protecting layer containing a Nafton-type perfluorinated polymer backbone (Figure 12d) with sulfonic side groups

ion-exchanged with Li-ions.^[223] An ionomer-Li metal anode was prepared via solvent casting directly on a Li chip. One of the advantages of such an ionomer, even at a thickness of a few nanometers on the Li metal anode, is that it exhibits a superior high ionic conductivity of ~10^{−3} S cm^{−1} and a high Li transference number of close to 0.9. This property goes against the conventional thought in that materials with a high transference number exhibit moderate or low ionic conductivity. Like many other artificial layers on Li metal anodes, the Li metal electrode with a 200 nm thick ionomer SEI, shown in Figure 12e, was observed to suppress uncontrollable and rough electrodeposition, resulting in a more compact and smooth electrode surface being observed than for bare Li. Furthermore, a full cell consisting of an NCA cathode (19.9 mg cm^{−2}) and a protective Li metal anode was shown to have a long life cycle (400 cycles) with less than 11% capacity fade.

3.3.3. Inorganic Artificial Layers

One reason why artificial layers are used for Li metal anodes is that Li is an extremely reactive metal. Using an artificial layer on direct Li metal is very useful to curtail the reactivity of Li metal during cycling. However, it is often accompanied by unwanted side reactions between the Li metal and the organic chemicals used in the layer. Besides this, if the protective layers are not chemically resistant with good mechanical properties, unpredictable dendritic Li growth brings about the appearance of cracks, leading to electrolyte depletion, overpotential, and ultimately a short cell lifespan. Thus, in view of these properties, the use of inorganic materials in the solid interface has been strongly considered. There are also other merits for their use,

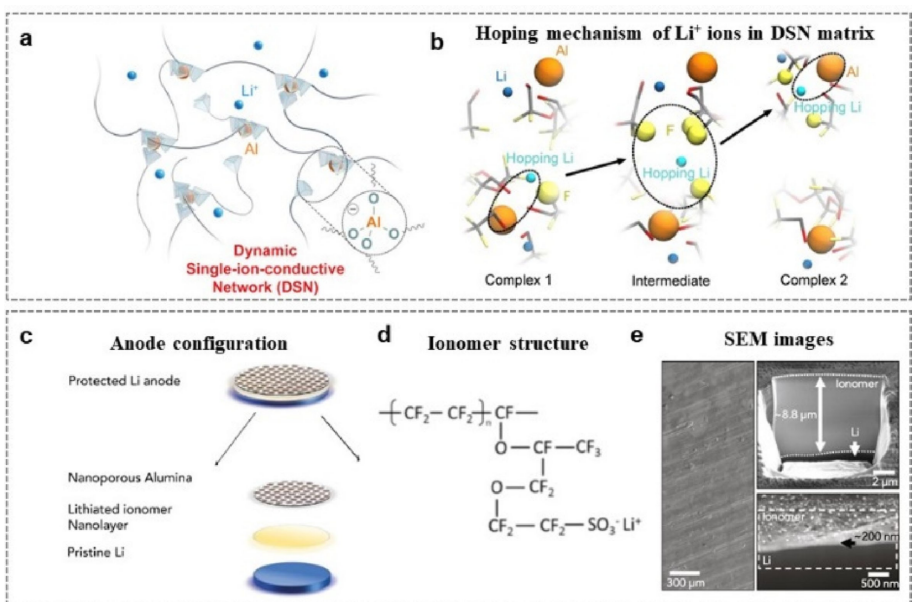


Figure 12. a) Conceptual sketch of Al-FTEG (DSN) (blue spheres: Li⁺ ions, orange spheres: Al atoms). b) Schematic illustration of the Li⁺ ion transport pathway and the hopping mechanism. Reproduced with permission.^[222] Copyright 2019, Elsevier. c) Schematic illustration of a Lithion-protected Li metal anode configuration for the cells. d) Ionomer molecular structure. e) Cyto-FIB-SEM images of an ionomer coated-Li metal anode with a thickness of 200 nm. Reproduced with permission.^[223] Copyright 2019, Elsevier.

such as the promotion of Li-ion conduction, blocking of electron transport, and buffering of the volume expansion of the Li metal anode.

Several studies have shown that various inorganic materials such as metal oxides and solid-state electrolytes are very reliable materials when used as protective layers for Li metal anodes.^[224–225] In a recent study, Qiao's group introduced an ultrathin bilayer of graphite/SiO₂ as an effective solid interface layer on Li metal anodes, as shown in Figure 13a, which shows its Li deposition mechanism.^[226] The bilayer on a direct Li chip surface was sequentially sputtered in the order of graphite and SiO₂ using a Torr combination system. Given the need to enable diffusion of Li-ions and the ability to handle higher mechanical stress during cycling, the ideal layer thicknesses were suggested to be 20 μm, respectively. Graphite and SiO₂ play different roles in the layer; graphite is a conductive skeleton in which to store Li, which helps to reduce the probability of the formation of dead Li and in maintaining a lower contact resistance. SiO₂ enhances the modulus of the material, so it aids in the effective suppression of dendritic Li growth. Also, SiO₂ allows fast Li diffusion because it simultaneously reacts with Li and forms Li-ion pathways. To confirm the mechanical strength of the material, AFM was used to measure the Young's modulus mapping, which is shown in Figure 12b. The Young's modulus value of the graphite/SiO₂ on Li was found to be 10.7 Gpa, while that of bare Li was only

0.23 Gpa. This result is significantly higher than the threshold value of 6.0 GPa, indicating that the graphite/SiO₂ Li electrode can withstand physical changes and has the desired mechanical stability for prolonged cycling. Finally, the suitability of the graphite/SiO₂ Li electrode for practical cells was verified using NMC111 as a cathode (10.0 mg cm⁻²) in a carbonate-based electrolyte. The graphite/SiO₂ Li electrode showed great performance in terms of an initial coulombic efficiency of 86.43%, an average cycling efficiency of over 99.3%, and capacity retention of 95.57%.

Similarly, Yan et al. demonstrated a quasi-solid interface layer of Li₃OCl covering a Li anode, as shown in Figure 13c.^[227] The application of this material was targeted at 4.5 V high-voltage rechargeable batteries containing an NCA cathode in a carbonate-based electrolyte. Operating a battery up to 4.5 V is unfavorable and hazardous to the chemical components in the cell because they decompose. Li₃OCl was suggested by the research group as a lightweight nanosized anti-perovskite solid-state electrolyte, which is non-flammable, chemical resistant, and has a thickness that can be controlled. A 500 nm in thickness Li₃OCl layer was prepared using vacuum filtration techniques and then coated on a Li metal surface. The orderly stacked Li₃OCl nanoparticles in the layer were found to effectively transport Li-ions and prevent dendritic Li growth due to high ionic conductivity and a high Young's modulus. In particular, the interface with high ionic conductivity showed a

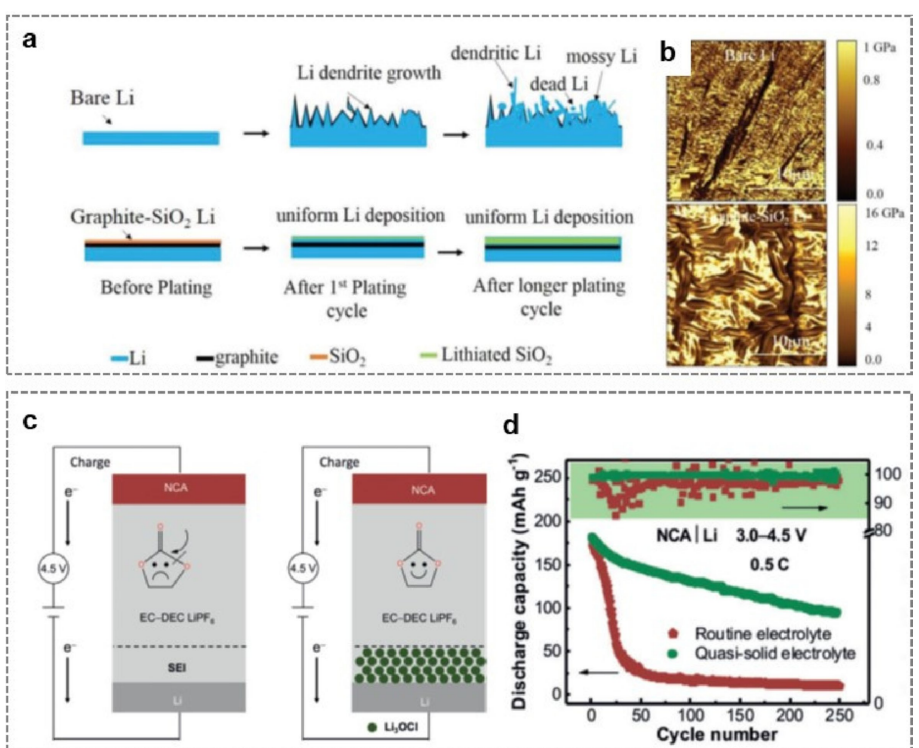


Figure 13. a) Schematic illustration of Li deposition on bare Li (top line) and on graphite-SiO₂ bilayer-modified Li (bottom line). b) Young's modulus mapping of bare Li (top) and on graphite-SiO₂ bilayer-modified Li (bottom) by AFM topography. Reproduced with permission.^[226] Copyright 2019, Wiley-VCH. c) Schematic diagram of the influence of the reduced polarization on Li metal anode. (Left) The solvent molecules in routine electrolyte decompose under 4.5 V high-voltage conditions. (Right) The Li₃OCl quasi-solid electrolyte layer that covers the Li metal efficiently prohibits the decomposition of solvent molecules. d) Electrochemical performance of NCA/Li batteries; the discharge capacity and Coulombic efficiency curves in routine and quasi-solid electrolytes, at a charge/discharge rate of 0.5 C and voltage windows of 3.0–4.5 V. Reproduced with permission.^[227] Copyright 2019, Wiley-VCH.

high Gibbs free energy of electrochemical oxidation for the electrolyte interphase and broadened the redox window of the liquid electrolyte, indirectly inducing a higher Li-ion potential for the cathode electrolyte interphase/liquid electrolyte. Therefore, a protected Li anode matched with a NCA cathode in a liquid electrolyte of 0.8 μL per gram of cathode active material exhibited excellent cycling stability over 250 cycles and a high average coulombic efficiency of up to 99.7%, as shown in Figure 12d.

3.3.4. Hybrid Artificial Layers

There is a trade-off between mechanical modulus and flexibility. Due to the inherent properties of materials, a dense inorganic-based artificial layer has a high mechanical modulus and low elasticity, and an organic-based artificial layer tends to have the complete opposite properties. For example, an inorganic material layer with high mechanical resistance provides a substantial physical barrier, however, it is often broken after prolonged battery operation due to its low flexibility, meaning that it cannot effectively bear stress, leading to the failure of the cell. Therefore, many researchers have been trying to develop ideal artificial layers for use in Li metal anodes that have the advantages of both types of layers.

In a recent study, Li et al. demonstrated a Li-ion affinity leaky film with high ion transport characteristics for use as a protective layer on a Li metal anode.^[228] The film was fabricated on top of Li metal via *in situ* crosslinking between polyethyleneimine (PEI) and hexamethylene diisocyanate (HDI) and consisted of crosslinked PEI-based polyurea (PU), poly(ethylene oxide) (PEO), and SiO_2 nanoparticles (PEIPU-PEO- SiO_2 , referred

to as PPS), as shown in Figure 14a. Although the chemical structure of the PPS film is complicated, each element of it plays a different important role. The amorphous PEO can facilitate improved Li-ion transport in the PPS layer. The inorganic SiO_2 nanoparticles in the polymer matrix contribute toward good mechanical strength and flexibility, leading to the material being able to withstand mechanical deformation upon Li plating/stripping processes. The Li-ion affinity functional groups in PEIPU, PEO, and SiO_2 can regulate Li-ion concentration and homogeneously distribute Li-ions and local current density on the Li metal surface. Therefore, the Li metal anode with the PPS film showed the ability to suppress dendritic Li growth even at an extremely high deposition capacity of 6 mAh cm^{-2} and a current density of 40 mA cm^{-2} , with significantly improved coulombic efficiency. A full cell with NMC811 (4.2 mAh cm^{-2}) as a cathode electrode and the protected Li metal as an anode exhibited good cycle retention of 80.3% over 200 cycles along with an average efficiency of 99.4%.

Another approach suggested by Lee et al. is the development of a Li-ion conductive material layer consisting of PVDF-HFP and Li metatitanate (Li_2TiO_3 , LT), as shown in Figure 14b–c.^[229] The layer was introduced onto the Li metal surface in two steps. To prepare the layer, they used a transference method from a PTFE film to a Li surface via a rolling and pressing process. There are reasons why LT is used as a material in the artificial layer; one is the 3D channel inside the LT structure, which enhances Li-ion migration even at a high-current density, resulting in low polarization and prevention of the dendritic Li growth during prolonged cycling. The other is the porous structure of the LT layer on the Li metal surface, which aids in the formation of a stable SEI layer that inhibits direct contact between the electrolyte and electrode. Consequentially, these

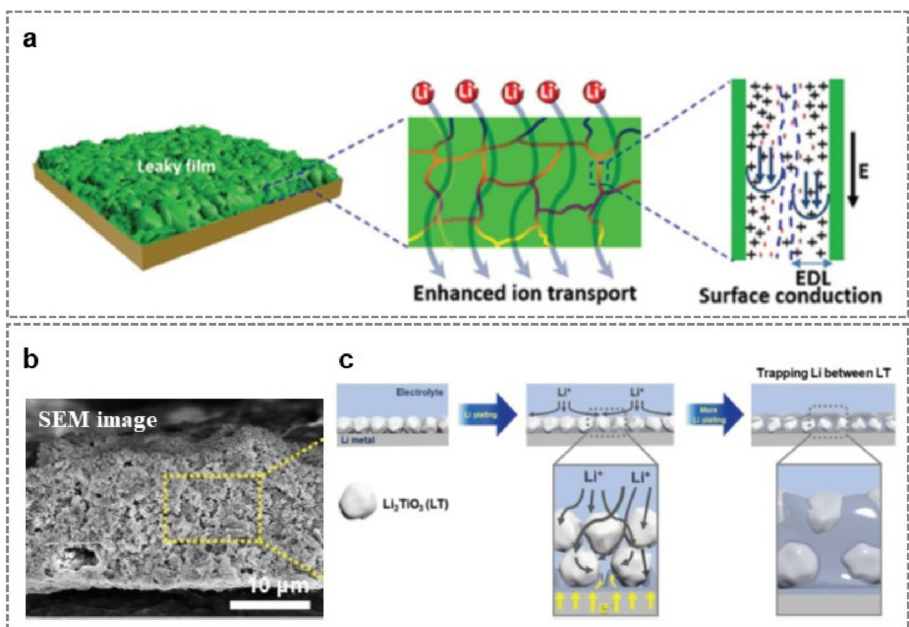


Figure 14. a) Schematic illustration of electrokinetic phenomena (i.e., electrokinetic surface conduction) in enhanced Li-ion transport in a leaky PPS film. Reproduced with permission.^[228] Copyright 2019, Wiley-VCH. b) SEM image of the fabricated Li_2TiO_3 layer. c) Schematic mechanistic illustrations: the Li plating of the LT-Li electrodes. Reproduced with permission.^[229] Copyright 2019, Wiley-VCH.

advantages of the LT system improve the electrochemical performance. Li-ions from the opposite electrode were reduced to Li metal between the LT particles, where there is an empty space in the layer, resulting in stable plating Li without the growth of Li dendrites. Furthermore, the Li metal anode with the LT layer was used in full cells containing NMC811, LNMO, and LMO, even at high temperatures over 60 °C. In particular, the full battery matched with NMC811 as a cathode and the Li metal with the artificial layer as an anode showed a great life span over 500 cycles, even at a current density of 450 mA g⁻¹.

4. Li Interphase Characterization

The Li metal surface has been accurately modified using various surface engineering strategies, as described in the previous section. The progress in this area suggests the possibility of the direct use of Li metal in a stable and high-voltage energy storage system. Meanwhile, technical assessment has also been important to visualize graphical results, deeply understand the surface evolution, and determine the Li metal morphology evolution depending on the surface characteristics in Li metal batteries. Various measurements were recently adopted to unveil Li metal electrochemistry in accordance with the purposes.^[5,230–234]

There are two streams in characterization methods of Li metal batteries according to the point when it is measured as follow; (i) the *in situ* method that directly analyzes a battery under a flowing current; and (ii) the *ex situ* method that analyzes an electrode or others extracted from the battery after cycling. Each of both ways has its pros and cons distinctly. In the case of the *in situ* technique, the strength is to provide direct information in real-time under flowing a current, such as Li formation of micro/macrostructure and reactions between Li-ions and an electrolyte during cycling. The information can be used to fully understand the deposition/desolation mechanism of Li in the working conditions of the battery. However, there are weaknesses in the *in situ* analysis, such as the requirement of special instruments with an electrochemical test module in a restrictive environment, and difficulties in the elucidation related to long-term cycle properties. In contrast, the *ex situ* technique is particularly valuable to substantiate the results working for extended cycles in real batteries, along with having versatility and simplicity. Nevertheless, the measurement is only providing discontinuous information at selected points during cycling, resulting in the fact that it would cause difficulty in verifying fundamental principles. Therefore, it is significantly important to select reasonable tools for the analysis of Li-metal anodes with consideration of all research situations.

In this section, we introduce and summarize the *in situ/ex situ* characterization through various tools, and provide the criterion of Li metal analysis.

4.1. Morphology Characterization

4.1.1. In Situ Macroscopic Observations

The observation of the complicated electrochemistry of original Li-metal batteries is essential to reveal the impact that intrinsic Li characteristics have on Li deposition/dissolution. From this point-of-view, *in situ* optical microscopy (OM) provides objective information while monitoring morphological and chemical phenomena that occur on the Li-metal surface in real time.^[235–240] The measurements are enabled through a visualization cell, connected to a potentiostat instrument and an OM (Figure 15a).^[237] The optical images in Figure 15b show the morphological changes of a Li metal anode via high-resolution video capture with a time-dependent voltage response for a Li|Li symmetric cell by dividing the measurements into six parts from before cycling to the end of the third half-cycle. There were no morphology changes or voltage changes before cycling, and the dendrites were observed to begin to nucleate on the surface of the Li metal (plating) randomly at state i. After the bias was applied at state ii, Li metal was deposited as arbitrary dendrites, the sizes of which eventually increased on the electrode. Then, while undergoing an initial dissolution process via reverse bias through states iii–iv, the Li dendrites quickly disappeared under large polarization. At the end of the stripping at state v, a pitting phenomenon occurred on the fresh Li metal, specifically not in the positions where the dendrites formed. Finally, as the plating process was started again (state vi), new dendritic whiskers formed at other local positions. Consequently, *in situ* OM observations allow the characterization of realistic Li-metal evolution for plating/stripping cycles.

Meanwhile, *in situ* SEM has also been used to show magnified, high-resolved, and three-dimensional Li dendrite evolution with the accurate distinction of growth form and elements under electrochemical reactions.^[241–243] The liquid cell used for the *in situ* electrochemical (EC)-SEM operation was initially assembled using a top silicon chip with a silicon nitride (SiN_x) membrane and bottom quartz chip with two injection orifices, followed by a sealing step using epoxy and liquid electrolyte injection (Figure 15c).^[241] Then, the growth and dissolution mechanism were observed through an electron beam penetrating into the SiN_x window when the electrochemical experiment was continuously carried out under LiTFSI in 1,3-dioxolane (DOL) and 1,2-dimethoxyethane (DME) electrolyte with a Li nitrate (LiNO₃) additive. Li dendrites were observed to build upon the Li/Cu electrode during electrodeposition (states i–iii), resulting in the material exhibiting a reddish color, indicating the presence of dense Li metal, as shown in Figure 15d. Generally, Li dendrites in ether-based electrolytes feature non-packed structures with continuous participation to construct a SEI layer on newly exposed locations upon electrodeposition. The EC-SEM measurements clearly showed that a high density of suppressed Li dendrites exist on the Li/Cu electrode in the presence of a Li nitrate (LiNO₃) additive, unlike under simple electrolyte conditions. Besides this, according to the SEM images of states iv–vi, some

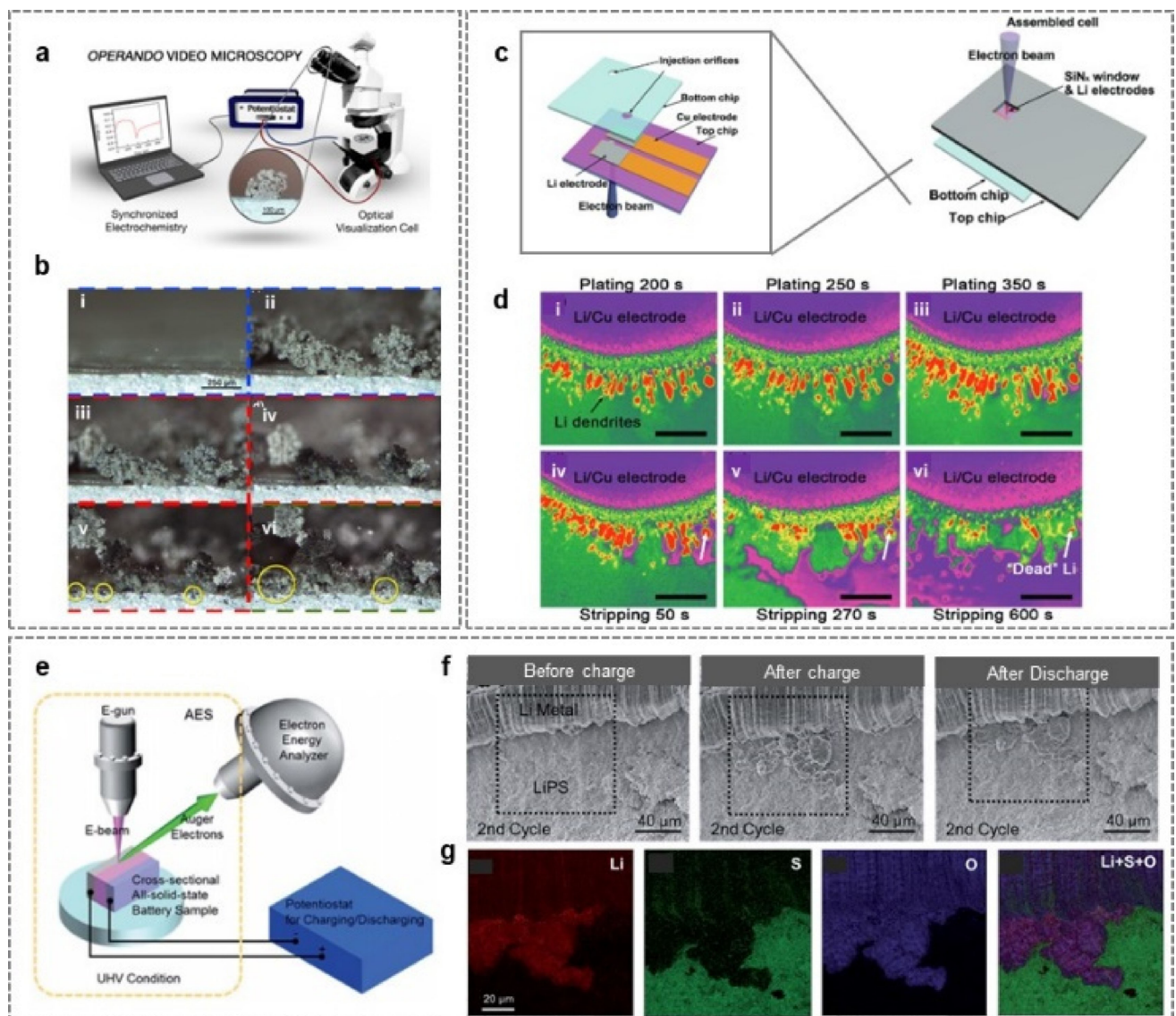


Figure 15. a) Schematic diagram of a synchronized electrochemical/video microscopy setup. b) The Li morphology (i) before cycling; (ii) after the first half-cycle; (iii) at the cell polarization minimum; (iv) at the cell polarization maximum; pitting not yet evident; (v) morphology at the end of a half-cycle; pitting observed (examples highlighted in yellow circles); (vi) morphology at the end of the third half-cycle; new dendrites are deposited in the pits that formed at the end of the previous half-cycle (yellow circles). Reproduced with permission.^[237] Copyright 2016, The Authors. c) Schemes and photographs of an *in situ* SEM-EC liquid cell. d) A time-lapse series of SEM images of the processes of i–iii) Li plating and iv–vi) stripping under 0.15 mA cm^{-2} on the Li/Cu electrode in LiTFSI/DOL/DME electrolyte with LiNO₃ (1 wt%) as an additive. Reproduced with permission.^[241] Copyright 2017, Wiley-VCH. e) Schematic showing an *in situ* Auger electron spectroscopy (AES)/Auger electron microscopy (AEM) setup. f) Series of SEM images of LiNi_{0.8}Mn_{0.05}Co_{0.15}O₂ (NMC811)/Li₆PS₅Cl (LiPS)/Li all-solid-state battery (ASSB) samples during the second cycle of charge and discharge and g) elemental maps after the charge process. Reproduced with permission.^[243] Copyright 2019, The Royal Society of Chemistry.

dendrites, referred to as dead Li, were still observed on the Li/Cu electrode after the stripping process. When tracing the time-lapse EC-SEM results shown in Figure 15d, Li metal was not dissolved from the top position. For this reason, some Li metal was locally isolated elsewhere, resulting in severance from the electrode. Consequently, EC-SEM objectively verified the critical reasons for the failure of Li-metal anodes via the monitoring of Li deposition/dissolution.

All-solid-state batteries (ASSBs), which feature solid-state electrolytes (SSEs), as one of their components in Li-based batteries, have been used to address the safety issues associated with liquid electrolytes. Beyond liquid cell operation

in conjunction with electron microscopy, *in situ* Auger electron microscopy (AEM)/Auger electron spectroscopy (AES), an SEM analysis technique, has also been used to investigate ASSBs, as shown in Figure 15e.^[243] Real-time monitoring of Li metal and SSEs in ASSBs, including sulfur-based Li₆PS₅Cl (LiPS) SSEs, was carried out to confirm Li-metal growth mechanism, volume expansion/contraction, and correlation with SSEs. The SEM images in Figure 15f show the Li dendrite morphology during the 2nd cycle, where the Li metal protruded while extruding the SSEs after the charging process. Then, the Li metal experienced a discharging process, where the Li-metal morphology became contoured and there was only structural contraction without

any shape changes. This means that Li metal is sensitive to the pressing forces, which are loaded on grown Li metal during Li extraction. Furthermore, the elemental mapping in Figure 15g suggests a correlation between Li-metal expansion and SSEs deformation. The SSEs changes alongside the Li metal growth contouring. Sulfur, present in the SSEs, was found to barely exist in the grown Li metal after the charging process, which clearly demonstrates that Li-metal growth in the presence of SSEs is dependent on the applied local pressure. These results confirm that homogeneous pressure distribution is a critical factor in inducing stable Li-metal growth, promoting the application of practical ASSBs.

4.1.2. In Situ Microscopic Observations

Transmission electron microscopy (TEM), operated at a high acceleration voltage, enables highly magnified orthographic images to be captured with nanoscale resolution. In this regard, TEM is a critical tool that can be used to investigate the morphological structure and thin layer of the Li surface.^[28,244–246] Beyond the simple observation of static samples, TEM analysis could be upgraded to deliver capture structural evolution of all reaction states via the design of a solid-state open cell, as depicted in Figure 16a.^[244] This cell consists of two separate electrodes, working and counter electrodes (typically Li) with a

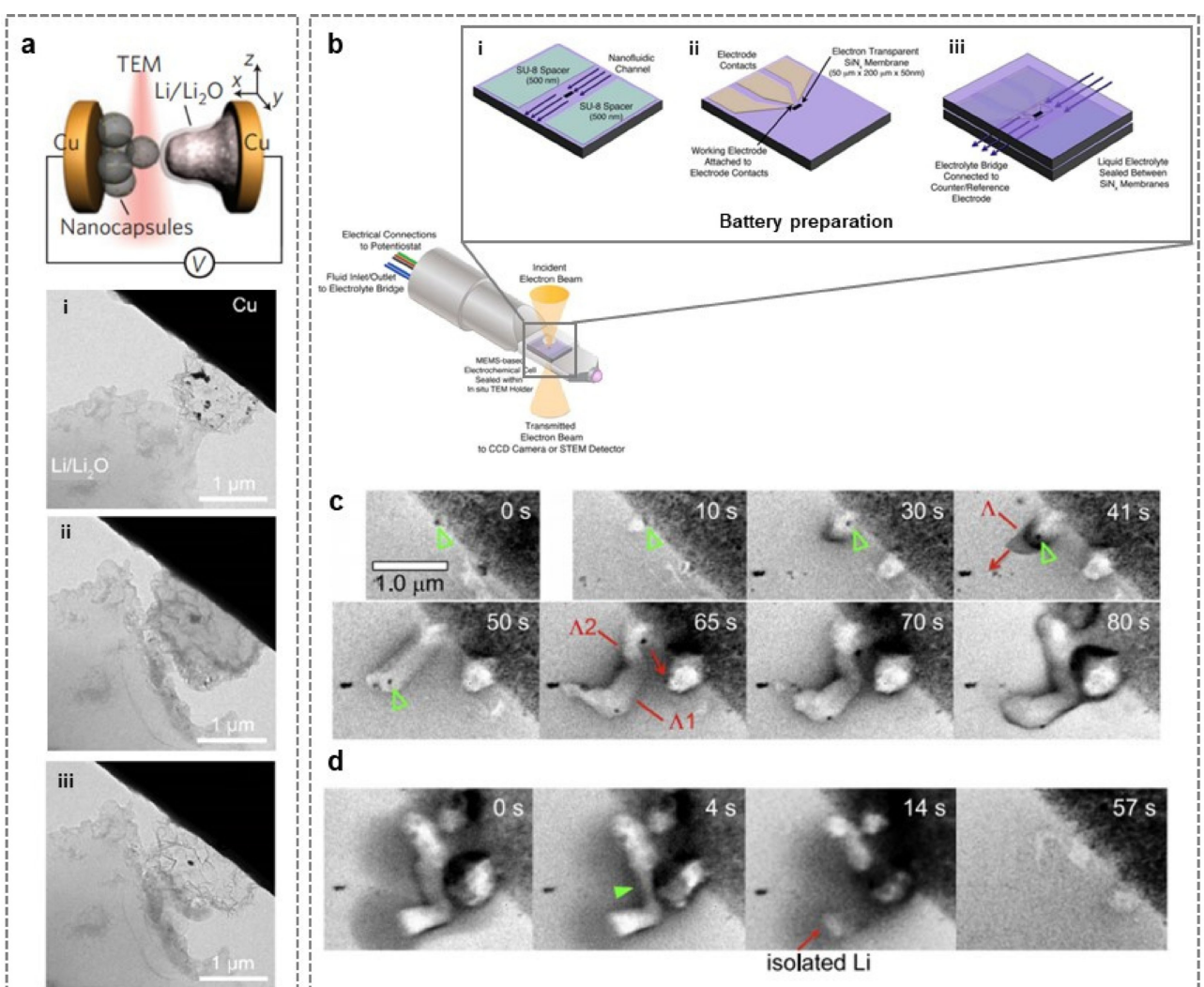


Figure 16. a) Schematic of a dry cell used in an *in situ* Li deposition study using TEM. Reproduced with permission.^[244] Copyright 2016, Springer Nature (i) *In situ* TEM observation of a pristine wrinkled graphene cage (WGC). (ii) The WGC is completely filled with Li metal during deposition and (iii) fully emptied after Li metal stripping. Reproduced with permission.^[28] Copyright 2019, American Chemical Society. b) *In situ* electrochemical liquid cell TEM: schematic illustration cutaway view of the *in situ* electrochemical fluid cell TEM holder with removable micro electro mechanical system-based silicon microchips. For the preparation, (i) an upper microchip with a 500 nm thick SU-8 spacer layer material patterned onto the surface of the SiN_x membrane, which was used to define the liquid electrolyte layer thickness and provide a nanofluidic pathway to transport electrolyte into the viewing chamber. (ii) Lower microchip with integrated Au electrodes patterned onto the surface of the SiN_x membrane, which interfaces the battery electrode to an external potentiostat. Both upper and lower microchips contain a central electron transparent SiN_x viewing membrane (50×200 μm) that is overlapped to image electrochemical processes within the liquid layer. (iii) Assembled electrochemical cell created by stacking the upper and lower microchips on top of one another (SiN_x membranes face-to-face) – a thin layer of liquid electrolyte is sealed and an electrolyte bridge is created between the electrochemical cell and an externally sealed counter/reference electrode via polyetheretherketone tubing. Reproduced with permission.^[245] Copyright 2014, Cambridge University Press. c) Temporal evolution of the growth of a single Li whisker under -6.0 V vs. LiCoO₂ (LCO) bias. d) The dissolution process at 0.0 V vs. LCO. Reproduced with permission.^[246] Copyright 2017, Elsevier.

solid-state electrolyte, as a naturally formed Li_2O inorganic layer, on the Li-metal surface. Using *in situ* TEM in a solid-state open cell, Li metal growth can be clearly observed when the electrode has lithophilic properties. General Cu current collectors suffer from uncontrollable Li dendritic growth upon Li electrodeposition, triggering short-circuiting and leading to Li isolation issues, whereas, gold (Au) nanoparticles, which are lithophilic, preferentially attract Li-ions on these surfaces while preventing Li dendrite behavior.^[28] *In situ* TEM characterization (Figure 16a) clearly enables the visualization of Li-metal evolution in the presence of Au particles through real-time electrochemical observations and provides crucial evidence to understand the Li-metal deposition kinetics. The pristine electrode (state i) before initiating an electrochemical reaction showed an empty inner surface with nanosized Au particles. After electrodeposition was completed (state ii), it exhibited compact filling in the internal space without any dendritic growth and then state iii showed the well-recovered morphological structure and no residual Li isolation after the Li stripping process. In addition to observing the time-lapse sequence of Li deposition, the electrode also reached a high coulombic efficiency of 99% at a current density of 1 mA cm^{-2} with a limited capacity of 1 mAh cm^{-2} during 140 cycles. Consequently, the lithophilic characteristics were obviously proven in the point that metallic Li grew onto the surface of Au nanoparticles during the deposition process, as well as the results of *in situ* TEM observations and electrochemical properties for long cycling.

Another type of electrochemical measurement using a liquid cell via *in situ* TEM could provide further critical information about the electrolyte/electrode interphase where the SEI forms, electrolyte decomposition occurs, similar to the realistic battery. Compared to a solid-state open cell, a liquid-type cell (Figure 16b) is typically fabricated as a closed system in which silicon nitride seals the whole component to prevent leakage of liquid electrolyte while allowing the electron beam to transmit across the cell.^[245] In this configuration, a working electrode is indirectly connected to the counter/reference electrodes as Li-ions diffuse via an electrolyte bridge. A liquid cell was sealed in an argon (Ar)-filled glove box with 1 M LiTFSI as an electrolyte in dimethoxy sulfoxide (DMSO), then transferred to the TEM holder and monitored under external bias.^[246] Negative bias induced Li electrodeposition was first applied to investigate the Li growth mechanism in a liquid electrolyte (Figure 16c). A thin SEI layer was initially formed as a result of electrolyte decomposition on the electrode, and then four distinguishable states (stages I–IV) occurred when Li-metal deposition gradually proceeded. Firstly, Li began to nucleate at the electrode surface and grew in the diffusion-limited direction under the SEI layer with short-range solid-state transportation. Importantly, *in situ* microscopic monitoring at this stage demonstrated that the Li deposition rate eventually decreased as time elapsed because Li-ions have a strong urge to penetrate the SEI layer to pair with electrons. Li grew from the nucleation root, in which the electrochemical kinetics of the Li growth were spontaneous, rather than initiating nucleation again on the electrode, while the Li rapidly grew in

the z-direction, compared to the width, where it was observed to barely expand in the x- and y-directions. The difference in thickness between the initially formed and newly formed SEI layer interrupted the root growth of the Li metal and instead the deposited Li experienced stress build-up, adopting a kink-like shape as an intermediate on the Li plating to release the built-up stress. Then, Li plating newly proceeded in the kinked direction again. When observing the stripping process (Figure 16d), the thinner SEI layer, located at a new position, facilitated fast Li-ion diffusion rather than the thick initially formed SEI layer, in which the inner position preferentially underwent Li-metal dissolution upon a positive external bias. For this reason, the dissolution sequence was quite different from the growth mechanism. Due to Li-metal dissolution in the inner SEI layer, Li consequently isolated from the electrode, resulting in the formation of dead Li in the liquid electrolyte. Meanwhile, Li dendrites below the initiating position continuously disappeared. These *in situ* TEM observations provide direct information on the time-lapsed Li growth mechanism, facile kinetics pathway related to the SEI layer formation/thickening for the whole Li plating process, and could clearly diagnose the main issues for Li metal battery failure.

4.1.3. Ex Situ Microscopic Observations

Time-lapse monitoring through *in situ* microscopy observations could help to understand basic Li metal evolution during the plating/stripping process in a transient environment or system. Unfortunately, Li metal and organic SEI layers are easily contaminated when exposed to an electron beam, as shown in Figure 17a, and therefore high-resolution observations need to be carried out via other microscopic approaches. Here TEM observations under cryogenic condition, known as cryo-electron microscopy (Cryo-EM),^[247–248] illustrated in Figure 17b, enable the characterization of the fine configuration of Li dendrites and SEI layer without any damage occurring from exposure to an electron beam in an extremely controlled system using liquid nitrogen gas.^[247] With the help of cryo-EM, selected area electron diffraction (SAED) patterns were clearly measured for three representative growth directions along the $<111>$, $<110>$, and $<211>$ directions and it was revealed that there is a preference for Li metal growth in a carbonate-based electrolyte in the $<111>$ direction, showing 49% growth in this direction compared to the other directions (Figure 17c). Furthermore, the crystalline growth direction of Li metal can change upon Li plating, referred to as kinks due to Li-ion diffusion interference and the build-up of stress in SEI layers with non-uniform depth across the whole Li metal surface. A specific direction or kinked position can be hardly observed because the Li experiences beam damage before any information can be obtained. Cryo-EM enables crystalline deformation in the kink region to be explored when Li metal grows in a carbonate-based electrolyte. The Li dendrite growth initially corresponds to the $<211>$ direction; however, this changes to the $<110>$ direction once kinking occurs (Figure 17d). Then, the growth pathway reverts to the $<211>$

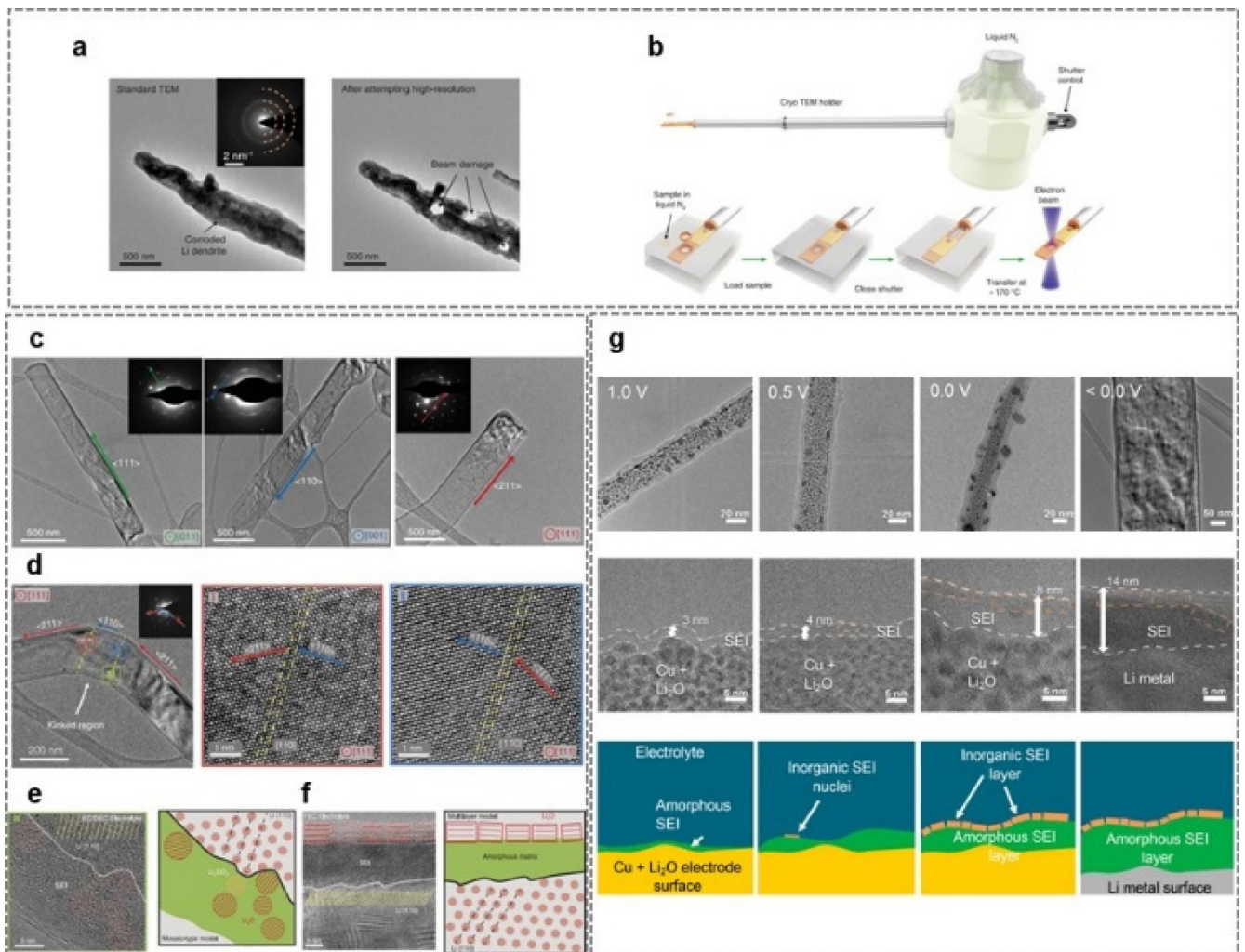


Figure 17. a) Standard TEM image of a Li-metal dendrite after ~1 s of air exposure at room temperature, where the inset shows the corresponding SAED pattern and the dendrite formed after exposure to an electron dose rate of $\sim 500 \text{ e}\AA^{-2}\text{s}^{-1}$ for ~1 s. Three holes were formed immediately after this exposure. b) The specimen was then placed onto a cryo-TEM holder while still immersed in liquid nitrogen and isolated from the environment using a closed shutter. During insertion into the TEM column, the temperatures do not increase above -170°C , and the shutter prevents exposure of the Li metal to air. c) Li metal dendrites and their corresponding SAED patterns (insets) growing along the $<111>$, $<110>$, and $<211>$ directions. Electron dose rate $<1 \text{ e}\AA^{-2}\text{s}^{-1}$ for ~30 s. d) TEM images of a kinked Li-metal dendrite that changes from $<211>$ to $<110>$ and back to the $<211>$ growth direction (inset shows corresponding SAED pattern) under an electron dose rate of $<1 \text{ e}\AA^{-2}\text{s}^{-1}$ for ~30 s and magnified images of the red region I and blue region II under an electron dose rate of $\sim 1000 \text{ e}\AA^{-2}\text{s}^{-1}$ for ~30 s. e) Atomic-resolution image of the green region III revealing the interface between the Li metal and the SEI. The lattice spacing of small crystalline grains of inorganic material dispersed throughout the amorphous film can be matched to Li carbonate (Li_2CO_3 , orange circles) and Li oxide (Li_2O , red circles). Electron dose rate of $\sim 1000 \text{ e}\AA^{-2}\text{s}^{-1}$ for ~30 s and schematic of the observed mosaic-type structure formed on Li dendrites in EC-DEC electrolyte. f) Atomic-resolution image of the SEI formed in FEC electrolyte. Electron dose rate of $\sim 1000 \text{ e}\AA^{-2}\text{s}^{-1}$ for ~30 s and schematic of the observed multilayered structure formed on the Li dendrites in the FEC electrolyte. Reproduced with permission.^[247] Copyright 2017, The Authors. g) TEM images and illustrations of the structural evolution of the inverted layered SEI nanostructure in EC/DEC + 10% FEC electrolyte at different potentials. Reproduced with permission.^[248] Copyright 2019, American Chemical Society.

direction in the second kink region. While high resolved images show an atomic array of Li at the kink regions, there was no beam interference, compared to standard TEM measurements, and interestingly, the Li metal did not feature any crystal defects even though typical nanowire growth is accompanied by the formation of defects.

Meanwhile, SEI layers, which settled on the Li metal or electrode surface, were found to vary depending on the compositions of the liquid electrolytes and influence the morphological structure of the growing Li metal. Cryo-EM also facilitated the characterization of the SEI layer, enabling high-

resolution images to be captured without any beam interruption (Figure 17e). When a standard electrolyte, a carbonate-based electrolyte (EC/DEC) was decomposed as the SEI layer, an amorphous SEI matrix (organic portion) was formed on the Li surface with randomly distributed small crystalline grains (~3 nm) composed of inorganic components, Li_2CO_3 , and Li_2O . This confirmed that carbonate-based electrolytes generally produce heterostructures through the decomposition of an organic/amorphous polymer matrix and inorganic $\text{Li}_2\text{CO}_3/\text{Li}_2\text{O}$ small domains along with a mosaic-type model. Interestingly, when FEC was added into the EC/DEC carbonate electrolyte as

an additive, the formed SEI structure was different compared to that in a simple EC/DEC electrolyte system (Figure 17f). The SEI layer featured a multilayer-like structure with two separated organic/inorganic layers in which stacked Li₂O particles were preferentially located on top, and, in contrast, an inner dense amorphous organic polymer matrix was formed on the Li (110) metal. Even though FEC exists in liquid electrolytes, LiF was curiously not observable in the SEI matrix, showing only its modified configuration. Furthermore, to clearly understand the *in situ* SEI structural evolution of an EC/DEC/FEC electrolyte system, copper oxide (CuO) nanowires on a Cu grid were exposed to a voltage sweep under a constant current density of 50 $\mu\text{A cm}^{-2}$ for SEI formation and 2.0 mA cm^{-2} for Li deposition (Figure 17g).^[248] Firstly, the initial CuO nanowires completed the conversion reaction to nanocrystalline Cu + Li₂O composites with a thin amorphous SEI layer (~3 nm) at 1.0 V vs. Li/Li⁺. When the potential was decreased to 0.5 V vs. Li/Li⁺, the SEI layer became thicker, at 4 nm, with the emergence of crystalline nanograins on the outermost surface. Then, most of the surface was covered with discrete inorganic particles at 0.0 V vs. Li/Li⁺, forming a thicker SEI layer (~8 nm) on the surface of the Cu + Li₂O composite nanowires. Finally, Li metal nucleated and grew under the formed SEI layer under negative potential compared with a Li reference electrode, and, interestingly, the pure SEI layer continuously thickened during Li deposition to 14 nm, rather than at 0.0 V before initiating Li nucleation. This means that solvent molecules in liquid electrolytes could diffuse or swell across inorganic components and an amorphous SEI layer is subsequently electrochemically formed due to Li nucleation overpotential. These results obtained via cryo-EM are crucial in revealing that the orientation of Li growth, a priority for SEI layer/structural formation, visibly depends on electrolyte compositions and further presents a way in which to resolve issues that occur in Li metal batteries.

4.2. X-Ray Surface Analysis

The primary Li growth mechanism in solid or liquid electrolytes has been well studied through microscopic measurements. Beyond the simple design of Li metal batteries, the field of the prevention of Li metal growth has grown rapidly in an attempt to modify the Li metal growth mechanism physically/chemically through facile Li-ion diffusion and hardening of the SEI layer via surface pretreatment and electrolyte control.^[122,249–251] Likewise, suitable qualitative analysis is suggested to unveil newly constructed SEI layer composition and Li metal growth behavior. X-ray-based analysis enables the measurement of atomic bonds and chemical structures, consisting of an overall SEI layer, the content of which depends on the electrolyte components and depth. In particular, XPS is a specialized technique that can be used to acquire information on reformed SEI layers, related to stable Li deposition. Thus, XPS is focused on here as a technique for carrying out qualitative surface studies. As mentioned above, the amorphous organic layer preferentially deposits an inner SEI layer near to the electrode

and inorganic components are subsequently loaded on the top surface of the SEI layer. However, liquid electrolytes can penetrate the entire SEI layer and continuously decompose as an organic matrix, even under 0.0 V vs. Li/Li⁺. Interestingly, the multi-stacking of layers can be reversed when the electrode is soaked in pure FEC solvent in advance. As a result, there is an inorganic layer, initially coated on the inner surface and then an organic layer present on the top.^[213] XPS depth profiling shows that O, F atoms eventually appear at internal positions in the form of Li₂CO₃ and LiF particles after 20 nm in-depth, where carbon composites were dominant on the top surface as almost organic component (ROCO₂Li) by carbonate electrolyte decomposition (Figure 18a). As the result, the electrode showed the average coulombic efficiency of 98.3% at a current density of 1.0 mA cm^{-2} . This confirms that the reversal of the stacking of layers occurs in which the inner inorganic layer enhances the SEI hardness and prevents the formation of an additional amorphous matrix on Li deposition.

Compared to conventional carbonate electrolyte, LiNO₃ additives in electrolyte enhance ionic conductivity and disperse Li-ion flux toward uniform Li deposition, where Li₃N shows high Li-ion conductivity, decomposed from LiNO₃ on lithiation.^[252] Depth-resolved XPS results demonstrate that residual LiN_xO_y molecules, which cannot penetrate into the inner surface, are present on the top surface and gradually N^{3–} positions, related to Li₃N, increased at the inner surface (Figure 18b). Thus, Li metal stably deposited on the very surface of the electrode without the formation of a Li dendritic structure based on its shallow location in comparison to the electrolyte, not including LiNO₃ salts. The effect of the salt in a carbonated electrolyte was proved to maintaining the highly stable coulombic efficiency over 98.1% after 200 cycles. This means that the SEI layer composition directly affects the Li growth morphology, delaying needle-like formation, as observed through depth observations using XPS.

4.3. Operando Visualization

4.3.1. Neutron Depth Profiling

Typical microscopic or spectroscopic measurements serve as visual and qualitative aids; however, these approaches might be limited in the case of sensitive polymeric layers or light metals such as Li. On the other hand, neutron depth profiling (NDP) allows the capture of the reaction of thermal neutrons of ⁶Li atoms forming ⁴He and ³H atoms, well-defined initial energies, and serves as a non-invasive operando measurement technique that enables the monitoring of Li growth dynamics and SEI formation kinetics as a function of depth in an electrode.^[232,253] A detector collects energy loss from the formed ⁴He and ³H atoms and calculates the depth of Li atoms and current density through Li amounts at that depth. However, when observing Li deposition/dissolution cycles on a Cu current collector, the ⁴He atoms cannot penetrate through a Cu electrode.^[253] So, the ³H atom is used to demonstrate Li metal density and growth behavior in the NDP system (Figure 19a,

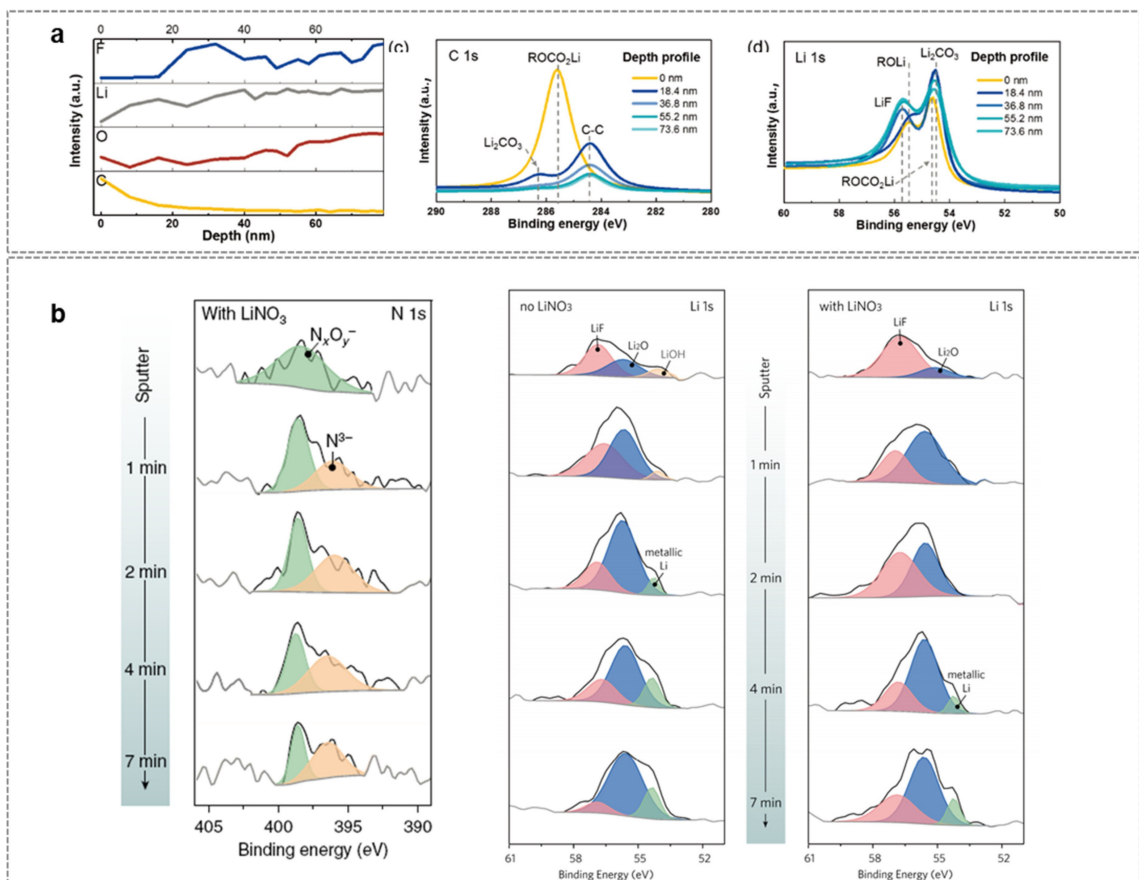


Figure 18. a) Relative elemental intensities along depth directions measured from XPS C 1s and Li 1s spectra. Reproduced with permission.^[213] Copyright 2018, Wiley-VCH. b) XPS N 1s depth profiles of the SEI formed in 0.5 M LiPF₆ EC/DEC electrolyte saturated with NO₃⁻ and a comparison of the SEI formed in the presence or absence of nitrate additive for XPS Li 1s when Li deposition was carried out at 1 mA cm⁻²/0.1 mAh cm⁻² on Cu foil. Reproduced with permission.^[252] Copyright 2018, The Authors.

left). To confirm the consequent Li depth and density through electrochemical deposition/dissolution, a current density of 1 mA cm⁻² was flowed through 1 mAh cm⁻² of the areal capacity for four charge/discharge cycles, where the Cu current collector was chosen as the working electrode, paired with a 500 μm Li foil on the other side as the counter/reference electrode. In the right hand side of Figure 19a, the blue-red gradation indicates low-high Li density on the Cu current collector, measured through an NDP detector on cycling. Dense Li metal was gradually plated on around 12 μm of the Cu current collector during the deposition states, and then Li disappeared upon stripping. Moreover, detection of the thickness of the Li metal was more profound, showing that a low density of metal was deposited close to the electrolytes, implying the high porosity of the Li morphology because the electrolyte reacts with the outermost surface of the formed Li metal structure. In this respect, the NDP results elucidate that Li metal builds heterostructured Li whiskers on deposition, which possess a high concentration of Li metal at the core with SEI components such as Li₂O, Li₂CO₃, and organic components in a shell, which produce cavities in the surface morphology.

Also, Li metal shows distinguishable electrochemical behavior, in that the current density influences Li efficiency and

morphological structure. Thus, additional measurements in this work were conducted to observe the relative behavior depending on the combination of current densities (Figure 19b). There were two types of electrochemical conditions used, slow (0.5 mA cm⁻²) and fast (2.0 mA cm⁻²) for every five cycles, in inverse order. The results for type I in order of density showed more dense Li plating density after the first five cycles and less Li concentration at the Li tail over 10 μm of deposited Li metal, compared with the Li morphology formed dendrite-like structure in Type II with widely distributed Li, after continuous plating under 0.5 mA cm⁻² without any remarkable variation in the Li density according to depth profiling. Interestingly, provided that the Li metal was first distributed at a slow current density (type I), the electrochemical system barely increased in terms of Li concentration even after the use of a fast current density (2.0 mA cm⁻²) in later cycles. Moreover, after stripping, for Type II, the remaining Li concentration on the Cu current collector eventually increased when the current density was changed, where the results reflect a steep decrease in the Li efficiency and rapid formation of inactive Li at overall Li deposition sites at 0.5 mA cm⁻². In contrast, type I showed a sustained fractional Li concentration under the following current density (0.5 mA cm⁻²) after 5 cycles, conducted at

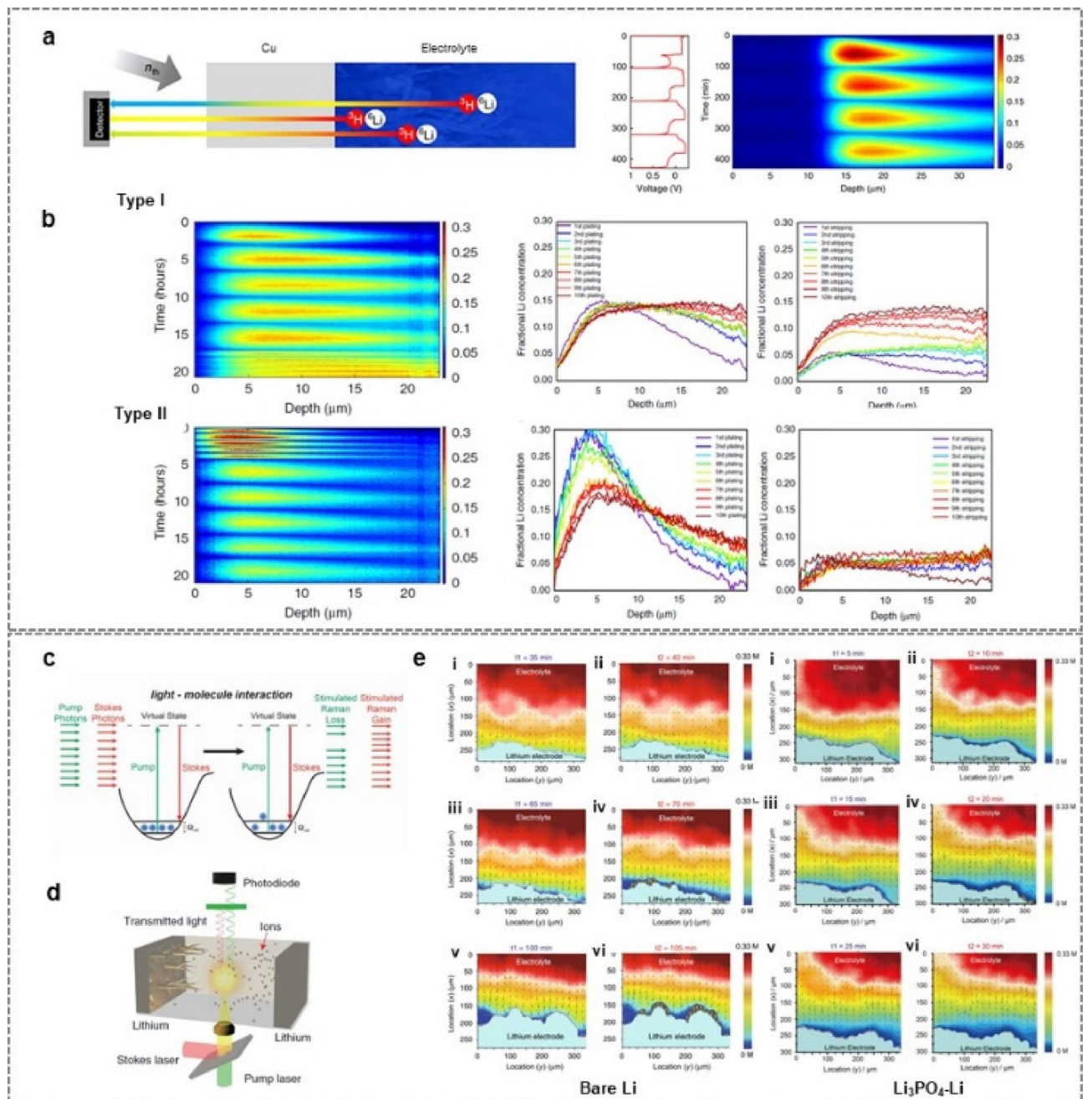


Figure 19. Principles of operando neutron depth profiling of Li-metal plating and stripping. a) Principles and schematic setup of operando neutron depth profiling (NDP). Operando NDP measurements of four plating and stripping cycles at 1.0 mA cm^{-2} current density, showing the fractional Li density as a function of depth perpendicular to the Cu current collector. The fractional Li density is obtained by normalizing the measured Li density using the Li-metal density. b) Evolution of the total amount of Li; operando NDP and impact of the plating history on the density during plating and stripping; fractional Li density from operando NDP for five plating/stripping cycles at 2 mA cm^{-2} followed by five cycles at 0.5 mA cm^{-2} (type I), and for five plating/stripping cycles at 0.5 mA cm^{-2} followed by two cycles at 0.5 mA cm^{-2} , all up to 1 mAh cm^{-2} plating capacity (Type II). The depth was measured starting from the interface of the Cu current collector with the electrolyte/SEI/Li-metal. Reproduced with permission.^[253] Copyright 2018, The Authors. c) Principles and experimental setup for stimulated Raman scattering (SRS) microscopy. d) A schematic illustration of a Li/Li symmetric cell under SRS imaging. The two lasers are pump and Stokes laser. e) Correlation between the local Li growth and local Li^+ concentration. 2D overlapping images at three representative moments (t_1/t_2), (i–ii) stage I/no depletion, (iii–iv) stage II/partial depletion, and (v–vi) stage III/full depletion for bare Li (left) and Li_3PO_4 -Li (right). Reproduced with permission.^[254] Copyright 2018, The Authors.

2.0 mA cm^{-2} , demonstrating relatively stable efficiency. Consequently, the initial Li-metal morphology critically affects the subsequent Li electrochemical behavior and Li-metal evolution on cycling. Broadly distributed Li deposition at low current

density induces large amounts of Li consumption upon SEI layer formation and leaves lots of inactive Li on the Cu current collector after stripping, in the form of dead Li metal. That is,

dense Li-metal formation on plating results in the high activity of the Li metal and reversible capacity on cycling.

4.3.2. Stimulated Raman Scattering Microscopy

Raman spectroscopy allows the measurement of the motions of chemical bonds in molecules, with a wide detection range. So, it enables the confirmation of Li-ion interactions in both liquid and solid environments, depending on salt concentrations, because all reactions follow electroneutrality in a system. Based on understanding of how Raman measurements mean, stimulated Raman scattering (SRS) further synchronizes two spatial and temporal pulses in picosecond resolution, the combined actions of which can increase vibrational motion by up to 10^8 times, over that in general Raman spectroscopy. In this respect, SRS allows accurate measurement of fast Li-ion concentration evolution and unveils that Li metal progresses through three states related to growth structures on Li electrodeposition.^[254] The fundamental principles of SRS are shown in Figure 19c, where the energy differences between the pump and Stokes photons represent the vibrational signals related to specific chemical bonds in molecules. This vibration creates two types of photons, stimulated Raman loss and stimulated Raman gain, resulting in color contrast for SRS spectroscopy. Meanwhile, a Li|Li symmetric cell was prepared to observe the Li metal growth mechanism in a Li bis(oxalate) borate (LiBOB)-included gel electrolyte through SRS imaging (Figure 19d). 2D overlapping images converted from SRS microscopy correspond to the relationship between local Li growth and Li-ion concentration on Li electrodeposition (Figure 19e, left). Li growth passes through three stages (stage I); no depletion (states i–ii), stage II; partial depletion (states iii–iv), and stage III; full depletion (states v–vi), showing spatial heterogeneity of Li-ion concentration as a function of depletion. Firstly, bare Li metal at states i and ii generally exists under such uniform Li-ion concentration. Then, once Li depletion in bare Li initiates, Li metal grows fast, while accompanying dense Li-ion concentration in certain positions (states iii and iv). The concentration gradient and growth speed finally show a big intensity difference between the highest/lowest values at states v and vi. Likewise, Li metal suffers from heterogeneous Li-ion concentration, resulting in jumbled Li deposition morphology. Homogeneous Li-ion concentration leading to tidy Li growth was additionally explored, where an artificial SEI layer consisting of a 100 nm thick Li₃PO₄-based interphase was introduced on Li metal. According to overlapped images of time-lapse observations through SRS microscopy (Figure 19e, right) of Li₃PO₄-loaded Li metal, states i–ii (stage I) in Li₃PO₄-Li show a similar Li growth mechanism to that of bare Li, but quite a slow Li growth rate owing to uniform Li-ion distribution on the electrode surface in states iii–iv (stage II). For this reason, the final Li morphology in states v–vi (stage III) features a smooth Li surface morphology without any height fluctuation. Consequently, SRS microscopy can be used to investigate a rational Li growth mechanism during Li electrodeposition through continuous detection of the Li-ion

concentration along with the vibrational frequency of chemical bonds of the Li salt in gel electrolyte, while surface modification of Li metal could stabilize the Li-ion distribution between the electrolyte/electrode, through indirect visualization in an electrochemical reaction.

5. Summary and Perspective

Li metal anodes enable the integration of high capacity and energy density owing to low operating voltage and high theoretical capacity in various battery systems paired with high-capacity cathodes (NCA/NCM), sulfur (S), and oxygen (O₂). We summary the related data and concept of the protecting layer approaches of this review in Table 1. Thus, there is no doubt that Li metal anodes are required in the development of high-energy-density battery systems. To handle versatile Li metal as an anode material, the suppression of infinite volume changes and arbitrary growth direction is essential when Li-ions undergo reduction at the electrode/electrolyte interface. These issues could be addressed through *ex situ/in situ* artificial layer formation of the Li metal or electrode. The addition of polymeric layers for physical protection or functional assignment (e.g., single-ion conductor) through a coating process efficiently alleviates Li dendrite growth toward the opposite electrode side during prolonged cycles and equalizes Li-ion flux at the electrode/electrolyte interface as well as improving Li-ion mobility. Besides this, metallic alloys containing Li stabilize the morphology of the Li structure in both deposition/dissolution states. Besides this, an artificial layer formed with the aid of salts, additives, and solvents in electrolytes allows stable Li-metal cyclability while physically/electrochemically protecting the Li surface on cycling. The dominance of specific species (e.g., LiF) as a SEI layer affects the modification of the Li metal surface and additional components (e.g., toluene) in electrolytes can manipulate electrochemical features in batteries.

Analytical techniques further guide the way toward the development of stable Li-metal anodes. Macro/microscopic observations via the use of OM, SEM, and TEM allow the visible elucidation of information on the objective Li-metal mechanism in various types of electrolytes and clues to how Li dendrite formation could be prevented. Moreover, XPS analysis clearly shows what types of components are formed during the electrochemical reaction between Li/electrolytes and which SEI layer components are helpful to stabilize the Li-metal surface. Other techniques such as NDP and SRS allow *in situ* visualization via spectroscopic measurements. These unveil overall Li-metal electrochemical mechanisms via simple long length/depth observations.

One of the inevitable issues of using Li metal as an efficient anode material is external influences. Li metal is not abundant in the earth and is hard to handle in an ambient atmosphere. So, upcoming strategies should focus on using less Li or Li-less anode systems to improve both cost and handling, which are compatible with high operating voltage/high-energy-density Li metal-based batteries.

Table 1. Summary of the recent artificial layer progress on Li metal anodes for high-energy-density batteries.

Batteries	Material	Methods	Approach (<i>in situ</i> or <i>ex situ</i>)	Current density [mA cm ⁻²]	Lifespan of Li/Li cell [h]	Cathode material for the full cell (active loading)	Life span of the full cell (cycles)
Li–O ₂	IL-TEMPO ^[156]	Electrolyte-additive	<i>in situ</i>	1	600	CNT	200
	TESI ^[54]	Electrolyte-additive	<i>in situ</i>	—	—	SWNT-SLG-IL gel	60
	InBr ₃ ^[158]	Electrolyte-additive	<i>in situ</i>	0.25	700	NWCNTs	206
	1-chlorodecane ^[160]	Exposure of Li	<i>ex situ</i>	2	300	Aligned-MWCNT	340
	TEOS ^[161]	Electrolyte-additive	<i>in situ</i>	—	—	Ru/CNTs	140
	Al ₂ O ₃ / PVDF-HFP ^[162]	Doctor blade coating	<i>ex situ</i>	—	—	Co ₃ O ₄ nanoparticles/ Super-P	80
	Al ₂ O ₃ / PVDF-HFP ^[163]	Doctor blade coating	<i>ex situ</i>	—	—	MWCNTs/PVDF-HFP/ TEMPO	175
	GeCl ₄ -THF ^[164]	Immersing Li metal in the solution	<i>ex situ</i>	3	>330	RuO ₂ /MnO ₂ /Super-P	>150
	FEC ^[255]	Electrolyte-additive	<i>in situ</i>	—	—	Super-P	>100
	TCCF ^[256]	Electrolyte-additive	<i>in situ</i>	1	>90	Super-P	50
	1 M LiTf-TEGDME ^[257]	Electrochemical method under Ar gas	<i>in situ</i>	—	—	CNTs	90
	Graphene -polydopamine ^[258]	Drop casting	<i>ex situ</i>	0.2	>500	Gas diffusion layer	150
	PEEK-WC/ nanosponge ^[259]	Inserting the membrane	<i>ex situ</i>	0.1	1250	Mesoporous carbon	80
	Boric acid ^[260]	Electrolyte-additive	<i>ex situ</i>	—	—	Carbon fiber	146
Li–S	SOCl ₂ ^[183]	Electrolyte-additive	<i>in situ</i>	3.8	100	pPAN@S composite (1 mg cm ⁻²)	>500 (1600 mA g ⁻¹)
	TMP-HFE ^[184]	Electrolyte-additive	<i>in situ</i>	1	350	S@pPAN composite (5.6 mg cm ⁻²)	>50 (0.483 mA cm ⁻²)
	LiPON ^[179]	Nitrogen plasma-assisted deposition	<i>ex situ</i>	3	600	CNT/S composite (7 mg cm ⁻²)	120 (0.79 mA cm ⁻²)
	MgO-containing layer ^[188]	Reaction of Li–Mg alloy	<i>in situ</i>	—	—	NBC/CNT/C (2 mg cm ⁻²)	200 (168 mA g ⁻¹)
	N-doped porous carbon nanosheet ^[192]	Attaching the Li surface	<i>ex situ</i>	0.5	1600	N-CNT/S (0.7 mg cm ⁻²)	1400 (3.0 A g ⁻¹)
	Metal fluoride complex ^[193] (MFC, Li ₃ Bi, LiF)	Immersing Li metal in the solution	<i>ex situ</i>	5.0	>160	Carbon nanofiber matrix/S (6.8 mg cm ⁻²)	200 (4 mA cm ⁻²)
	18-crown-6/PVDF ^[261]	Spin coating	<i>ex situ</i>	1	149	S	200 (335 mA g ⁻¹)
	Sericin protein ^[262]	Drop casting	<i>ex situ</i>	10	160	N-doped carbon/S (1 mg cm ⁻²)	520 (1672 mA g ⁻¹)
	Fluorinated ethers ^[170]	Electrolyte-additive	<i>in situ</i>	—	—	Bulk sulfur	200 (167 mA g ⁻¹)
	Li ₃ PS ₄ ^[169]	Immersing Li in P ₄ S ₁₆ / NMP	<i>ex situ</i>	0.5	2000	S@C (0.8–1.3 mg cm ⁻²)	400 (5 A g ⁻¹)
Li metal	PEO-UPy/THF ^[263]	Drop casting	<i>ex situ</i>	1	1000	NMC622 (8 mg cm ⁻²)	200 (180 mA g ⁻¹)
	Toluene (TOL) ^[203]	Electrolyte-additive	<i>in situ</i>	—	—	NMC532 (9 mg cm ⁻²)	80 (1.4 mA cm ⁻²)
	FEC ^[213]	Immersing Li metal in the solution	<i>ex situ</i>	1	120	NMC532 (12.02 mg cm ⁻²)	120 (91 mA g ⁻¹)
	AgTFSI in DME:FEC ^[214]	Immersing Li metal in the solution	<i>ex situ</i>	0.5	1000	NMC111 (1.8 mAh cm ⁻²)	100 (1.8 mA cm ⁻²)
	Al(OR) ⁺ -FTEG ^[222]	Spin coating/Dip coating	<i>ex situ</i>	1	2000	NMC532 (2 mAh cm ⁻²)	160 (1 mA cm ⁻²)
	Ionomer solution ^[223] (LITHion TM)	Coating	<i>ex situ</i>	3	830	NCA (3 mAh cm ⁻²)	400 (1.5 mA cm ⁻²)
	Graphite/SiO ₂ ^[226]	Sputtering	<i>ex situ</i>	1	800	NMC111 (9.98 mg cm ⁻²)	150 (1 C)
	Li ₃ OCl ^[227]	Coating	<i>ex situ</i>	—	—	NCA (10 mg cm ⁻²)	200 (5 mA cm ⁻²)
	PEIPU-PEO-SiO ₂ ^[228] (PPS)	Drop coating	<i>ex situ</i>	1	1000	NMC811 (4.2 mAh cm ⁻²)	200 (0.6 mA cm ⁻²)
	Li ₂ TiO ₃ / PVDF-HFP ^[229]	Coating	<i>ex situ</i>	1	350	NMC811 (1.5 mAh cm ⁻²)	500 (450 mA g ⁻¹)

Acknowledgements

This work was supported by Climate Changes through the National Research Foundation of Korea (NRF) funded by the Ministry of Science, ICT & Future Planning (2018M1A2A2063346)

and Presidential Post-Doc. Fellowship through the National Research Foundation of Korea (NRF) funded by the Ministry of Education (2017R1A6A3A04010902).

Conflict of Interest

The authors declare no conflict of interest.

Keywords: lithium metal anode · high-energy-density battery · artificial layer · Li metal protection · Lithium metal anode

- [1] J. M. Tarascon, M. Armand, *Nature*. **2001**, *414*, 359–367.
- [2] W. Xu, J. Wang, F. Ding, X. Chen, E. Nasybulin, Y. Zhang, J.-G. Zhang, *Energy Environ. Sci.* **2014**, *7*, 513–537.
- [3] P. G. Bruce, S. A. Freunberger, L. J. Hardwick, J.-M. Tarascon, *Nat. Mater.* **2012**, *11*, 19–29.
- [4] M. S. Whittingham, A. H. Thompson, *J. Chem. Phys.* **1975**, *62*, 1588–1588.
- [5] D. Lin, Y. Liu, Y. Cui, *Nat. Nanotechnol.* **2017**, *12*, 194–206.
- [6] X.-B. Cheng, R. Zhang, C.-Z. Zhao, Q. Zhang, *Chem. Rev.* **2017**, *117*, 10403–10473.
- [7] C. Yang, K. Fu, Y. Zhang, E. Hitz, L. Hu, *Adv. Mater.* **2017**, *29*, 1701169.
- [8] M. Li, J. Lu, Z. Chen, K. Amine, *Adv. Mater.* **2018**, *30*, 1800561.
- [9] G. E. Blomgren, *J. Electrochem. Soc.* **2016**, *164*, A5019–A5025.
- [10] C. Julien, A. Mauger, K. Zaghib, H. Groult, *Inorganics* **2014**, *2*, 132–154.
- [11] V. Etacheri, R. Marom, R. Elazari, G. Salitra, D. Aurbach, *Energy Environ. Sci.* **2011**, *4*, 3243–3262.
- [12] M. Winter, B. Barnett, K. Xu, *Chem. Rev.* **2018**, *118*, 11433–11456.
- [13] J. Tarascon, *Electrochem. Soc. Interface* **2016**, *25*, 79–83.
- [14] R. Zhang, N. W. Li, X. B. Cheng, Y. X. Yin, Q. Zhang, Y. G. Guo, *Adv. Sci.* **2017**, *4*, 1600445.
- [15] Y. Guo, H. Li, T. Zhai, *Adv. Mater.* **2017**, *29*, 1700007.
- [16] N. W. Li, Y. X. Yin, C. P. Yang, Y. G. Guo, *Adv. Mater.* **2016**, *28*, 1853–1858.
- [17] B. Liu, J.-G. Zhang, W. Xu, *Joule* **2018**, *2*, 833–845.
- [18] Y. Liu, X. Qin, S. Zhang, Y. Huang, F. Kang, G. Chen, B. Li, *Energy Storage Mater.* **2019**, *18*, 320–327.
- [19] A. Rosenman, E. Markevich, G. Salitra, D. Aurbach, A. Garsuch, F. F. Chesneau, *Adv. Energy Mater.* **2015**, *5*, 1500212.
- [20] N. Imanishi, O. Yamamoto, *Mater. Today Adv.* **2019**, *4*, 100031.
- [21] J. He, A. Manthiram, *Energy Storage Mater.* **2019**, *20*, 55–70.
- [22] H. Yang, C. Guo, A. Naveed, J. Lei, J. Yang, Y. Nuli, J. Wang, *Energy Storage Mater.* **2018**, *14*, 199–221.
- [23] Z. A. Ghazi, Z. Sun, C. Sun, F. Qi, B. An, F. Li, H. M. Cheng, *Small* **2019**, *15*, e1900687.
- [24] H. Kang, M. Boyer, G. S. Hwang, J. W. Lee, *Electrochim. Acta* **2019**, *303*, 78–84.
- [25] H. Ye, S. Xin, Y.-X. Yin, Y.-G. Guo, *Adv. Energy Mater.* **2017**, *7*, 1700530.
- [26] G. Huang, J. Han, F. Zhang, Z. Wang, H. Kashani, K. Watanabe, M. Chen, *Adv. Mater.* **2019**, *31*, 1805334.
- [27] Z. Lu, S. Liu, C. Li, J. Huang, D. Wu, R. Fu, *Chem Comm* **2019**, *55*, 6034–6037.
- [28] H. Wang, Y. Li, Y. Li, Y. Liu, D. Lin, C. Zhu, G. Chen, A. Yang, K. Yan, H. Chen, Y. Zhu, J. Li, J. Xie, J. Xu, Z. Zhang, R. Vila, A. Pei, K. Wang, Y. Cui, *Nano Lett.* **2019**, *19*, 1326–1335.
- [29] C. Niu, H. Pan, W. Xu, J. Xiao, J.-G. Zhang, L. Luo, C. Wang, D. Mei, J. Meng, X. Wang, Z. Liu, L. Mai, J. Liu, *Nat. Nanotechnol.* **2019**, *14*, 594–601.
- [30] S. Huang, W. Zhang, H. Ming, G. Cao, L.-Z. Fan, H. Zhang, *Nano Lett.* **2019**, *19*, 1832–1837.
- [31] H. Ye, Z. J. Zheng, H. R. Yao, S. C. Liu, T. T. Zuo, X. W. Wu, Y. X. Yin, N. W. Li, J. J. Gu, F. F. Cao, Y. G. Guo, *Angew. Chem. Int. Ed.* **2019**, *58*, 1094–1099.
- [32] S. Li, S. Fang, H. Dou, X. Zhang, *ACS Appl. Mater. Interfaces* **2019**, *11*, 20804–20811.
- [33] Q. Zhang, K. Wang, X. Wang, Y. Zhong, M. Liu, X. Liu, K. Xu, W. Fan, L. Yu, W. Li, *ACS Appl. Mater. Interfaces* **2019**, *11*, 20854–20863.
- [34] N. Phattharasupakun, J. Wuttiprom, S. Duangdangchote, M. Sawangphruk, *Chem Comm* **2019**, *55*, 5689–5692.
- [35] Y. Feng, C. Zhang, B. Li, S. Xiong, J. Song, *J. Mater. Chem. A* **2019**, *7*, 6090–6098.
- [36] M. Ue, K. Uosaki, *Curr Opin Electrochem* **2019**, *17*, 106–113.
- [37] M. D. Tikekar, S. Choudhury, Z. Tu, L. A. Archer, *Nat. Energy* **2016**, *1*, 16114.
- [38] X. B. Cheng, R. Zhang, C. Z. Zhao, F. Wei, J. G. Zhang, Q. Zhang, *Adv. Sci.* **2016**, *3*, 1500213.
- [39] S. Hess, M. Wohlfahrt-Mehrens, M. Wachtler, *J. Electrochem. Soc.* **2015**, *162*, A3084–A3097.
- [40] H. Zhang, G. G. Eshetu, X. Judez, C. Li, L. M. Rodriguez-Martínez, M. Armand, *Angew. Chem. Int. Ed.* **2018**, *57*, 15002–15027.
- [41] S. Jiao, X. Ren, R. Cao, M. H. Engelhard, Y. Liu, D. Hu, D. Mei, J. Zheng, W. Zhao, Q. Li, N. Liu, B. D. Adams, C. Ma, J. Liu, J.-G. Zhang, W. Xu, *Nat. Energy* **2018**, *3*, 739–746.
- [42] Y. Zhu, J. G. Connell, S. Tepavcevic, P. Zapol, R. Garcia-Mendez, N. J. Taylor, J. Sakamoto, B. J. Ingram, L. A. Curtiss, J. W. Freeland, D. D. Fong, N. M. Markovic, *Adv. Energy Mater.* **2019**, *9*, 1803440.
- [43] H. Duan, M. Fan, W.-P. Chen, J.-Y. Li, P.-F. Wang, W.-P. Wang, J.-L. Shi, Y.-X. Yin, L.-J. Wan, Y.-G. Guo, *Adv. Mater.* **2019**, *31*, 1807789.
- [44] P. Wang, J. Chai, Z. Zhang, H. Zhang, Y. Ma, G. Xu, H. Du, T. Liu, G. Li, G. Cui, *J. Mater. Chem. A* **2019**, *7*, 5295–5304.
- [45] W. Zhou, Z. Wang, Y. Pu, Y. Li, S. Xin, X. Li, J. Chen, J. B. Goodenough, *Adv. Mater.* **2019**, *31*, 1805574.
- [46] X.-B. Cheng, C.-Z. Zhao, Y.-X. Yao, H. Liu, Q. Zhang, *Chem* **2019**, *5*, 74–96.
- [47] X. Zhang, S. Wang, C. Xue, C. Xin, Y. Lin, Y. Shen, L. Li, C.-W. Nan, *Adv. Mater.* **2019**, *31*, 1806082.
- [48] N. Wu, Y.-R. Shi, S.-Y. Lang, J.-M. Zhou, J.-Y. Liang, W. Wang, S.-J. Tan, Y.-X. Yin, R. Wen, Y.-G. Guo, *Angew. Chem. Int. Ed.* **2019**, *58*, 18146–18149.
- [49] S.-J. Park, J.-Y. Hwang, Y.-K. Sun, *J. Mater. Chem. A* **2019**, *7*, 13441–13448.
- [50] S. H. Lee, J. Y. Hwang, S. J. Park, G. T. Park, Y. K. Sun, *Adv. Funct. Mater.* **2019**, *29*, 1902496.
- [51] F. Liu, R. Xu, Z. Hu, S. Ye, S. Zeng, Y. Yao, S. Li, Y. Yu, *Small* **2019**, *15*, e1803734.
- [52] Z. Lu, Q. Liang, B. Wang, Y. Tao, Y. Zhao, W. Lv, D. Liu, C. Zhang, Z. Weng, J. Liang, H. Li, Q.-H. Yang, *Adv. Energy Mater.* **2019**, *9*, 1803186.
- [53] B. Yoon, S. Kim, Y. M. Lee, M.-H. Ryoo, *ACS Omega* **2019**, *4*, 11724–11727.
- [54] R. Xu, X.-B. Cheng, C. Yan, X.-Q. Zhang, Y. Xiao, C.-Z. Zhao, J.-Q. Huang, Q. Zhang, *Matter* **2019**, *1*, 317–344.
- [55] S. Wei, S. Choudhury, Z. Tu, K. Zhang, L. A. Archer, *Acc. Chem. Res.* **2018**, *51*, 80–88.
- [56] X.-Q. Zhang, X.-B. Cheng, Q. Zhang, *Adv. Mater. Interfaces* **2018**, *5*, 1701097.
- [57] J. Lang, Y. Long, J. Qu, X. Luo, H. Wei, K. Huang, H. Zhang, L. Qi, Q. Zhang, Z. Li, H. Wu, *Energy Storage Mater.* **2019**, *16*, 85–90.
- [58] M. Du, K. Liao, Q. Lu, Z. Shao, *Energy Environ. Sci.* **2019**, *12*, 1780–1804.
- [59] H. Wang, D. Lin, J. Xie, Y. Liu, H. Chen, Y. Li, J. Xu, G. Zhou, Z. Zhang, A. Pei, Y. Zhu, K. Liu, K. Wang, Y. Cui, *Adv. Energy Mater.* **2019**, *9*, 1802720.
- [60] J. Bae, Y. Qian, Y. Li, X. Zhou, J. B. Goodenough, G. Yu, *Energy Environ. Sci.* **2019**, *12*, 3319–3327.
- [61] H. Chen, A. Pei, D. Lin, J. Xie, A. Yang, J. Xu, K. Lin, J. Wang, H. Wang, F. Shi, D. Boyle, Y. Cui, *Adv. Energy Mater.* **2019**, *9*, 1800858.
- [62] Y. Guo, P. Niu, Y. Liu, Y. Ouyang, D. Li, T. Zhai, H. Li, Y. Cui, *Adv. Mater.* **2019**, *31*, 1900342.
- [63] R. Xu, Y. Xiao, R. Zhang, X. B. Cheng, C. Z. Zhao, X. Q. Zhang, C. Yan, Q. Zhang, J. Q. Huang, *Adv. Mater.* **2019**, *31*, e1808392.
- [64] Y. Sun, Y. Zhao, J. Wang, J. Liang, C. Wang, Q. Sun, X. Lin, K. R. Adair, J. Luo, D. Wang, R. Li, M. Cai, T. K. Sham, X. Sun, *Adv. Mater.* **2019**, *31*, e1806541.
- [65] H. Wang, D. Yu, C. Kuang, L. Cheng, W. Li, X. Feng, Z. Zhang, X. Zhang, Y. Zhang, *Chem* **2019**, *5*, 313–338.
- [66] X. Guan, A. Wang, S. Liu, G. Li, F. Liang, Y. W. Yang, X. Liu, J. Luo, *Small* **2018**, *14*, e1801423.
- [67] S. Jiao, J. Zheng, Q. Li, X. Li, M. H. Engelhard, R. Cao, J.-G. Zhang, W. Xu, *Joule* **2018**, *2*, 110–124.
- [68] P. Shi, X. B. Cheng, T. Li, R. Zhang, H. Liu, C. Yan, X. Q. Zhang, J. Q. Huang, Q. Zhang, *Adv. Mater.* **2019**, *e1902785*.
- [69] G. García, S. Dieckhöfer, W. Schuhmann, E. Ventosa, *J. Mater. Chem. A* **2018**, *6*, 4746–4751.
- [70] C. Chu, N. Wang, L. Li, L. Lin, F. Tian, Y. Li, J. Yang, S. -x Dou, Y. Qian, *Energy Storage Mater.* **2019**, *23*, 137–143.
- [71] L. Wang, Z. Zhou, X. Yan, F. Hou, L. Wen, W. Luo, J. Liang, S. X. Dou, *Energy Storage Mater.* **2018**, *14*, 22–48.
- [72] Y. Han, Y. Jie, F. Huang, Y. Chen, Z. Lei, G. Zhang, X. Ren, L. Qin, R. Cao, S. Jiao, *Adv. Funct. Mater.* **2019**, *29*, 1904629.

- [73] J. Alvarado, M. A. Schroeder, T. P. Pollard, X. Wang, J. Z. Lee, M. Zhang, T. Wynn, M. Ding, O. Borodin, Y. S. Meng, K. Xu, *Energy Environ. Sci.* **2019**, *12*, 780–794.
- [74] X. Ren, L. Zou, X. Cao, M. H. Engelhard, W. Liu, S. D. Burton, H. Lee, C. Niu, B. E. Matthews, Z. Zhu, C. Wang, B. W. Arey, J. Xiao, J. Liu, J.-G. Zhang, W. Xu, *Joule* **2019**, *3*, 1662–1676.
- [75] F. Qiu, X. Li, H. Deng, D. Wang, X. Mu, P. He, H. Zhou, *Adv. Energy Mater.* **2019**, *9*, 1803372.
- [76] Y. Yamada, J. Wang, S. Ko, E. Watanabe, A. Yamada, *Nat. Energy* **2019**, *4*, 269–280.
- [77] M. S. Kim, J.-H. Ryu, Y. Deepika, R. Lim, I. W. Nah, K.-R. Lee, L. A. Archer, W. Il Cho, *Nat. Energy* **2018**, *3*, 889–898.
- [78] Y. Sawada, A. Dougherty, J. P. Gollub, *Phys. Rev. Lett.* **1986**, *56*, 1260.
- [79] C. Léger, J. Elezgaray, F. Argoul, *Phys. Rev. E* **1998**, *58*, 7700.
- [80] E. B. Budevski, G. T. Staikov, W. J. Lorenz, *Electrochemical phase formation and growth: an introduction to the initial stages of metal deposition*, John Wiley & Sons, 2008.
- [81] M. Musiani, *Electrochim. Acta* **2000**, *45*, 3397–3402.
- [82] J.-C. Bradley, H.-M. Chen, J. Crawford, J. Eckert, K. Ernazarova, T. Kurzeja, M. Lin, M. McGee, W. Nadler, S. G. Stephens, *Nature* **1997**, *389*, 268–271.
- [83] A. J. Bard, L. R. Faulkner, J. Leddy, C. G. Zoski, *Electrochemical methods: fundamentals and applications*, Vol. 2, Wiley New York, 1980.
- [84] P. Bai, J. Li, F. R. Brushett, M. Z. Bazant, *Energy Environ. Sci.* **2016**, *9*, 3221–3229.
- [85] H. J. S. Sand, *Philos. Mag.* **1901**, *1*, 45–79.
- [86] L. Gireaud, S. Grugeon, S. Laruelle, B. Yrieix, J. M. Tarascon, *Electrochem. Commun.* **2006**, *8*, 1639–1649.
- [87] J. Chazalviel, *Phys. Rev. A* **1990**, *42*, 7355–7367.
- [88] C. Brissot, M. Rosso, J. N. Chazalviel, S. Lascaud, *J. Power Sources* **1999**, *81–82*, 925–929.
- [89] C. Brissot, M. Rosso, J. N. Chazalviel, P. Baudry, S. Lascaud, *Electrochim. Acta* **1998**, *43*, 1569–1574.
- [90] M. Rosso, T. Gobron, C. Brissot, J. N. Chazalviel, S. Lascaud, *J. Power Sources* **2001**, *97–98*, 804–806.
- [91] M. Rosso, C. Brissot, A. Teyssot, M. Dollé, L. Sannier, J.-M. Tarascon, R. Bouchet, S. Lascaud, *Electrochim. Acta* **2006**, *51*, 5334–5340.
- [92] Y. S. Cohen, Y. Cohen, D. Aurbach, *J. Phys. Chem. B* **2000**, *104*, 12282–12291.
- [93] D. Aurbach, *J. Power Sources* **2000**, *89*, 206–218.
- [94] A. Wang, S. Kadam, H. Li, S. Shi, Y. Qi, *Npj Comput. Mater.* **2018**, *4*, 15.
- [95] E. Peled, S. Menkin, *J. Electrochem. Soc.* **2017**, *164*, A1703–A1719.
- [96] S. Schweidler, L. de Biasi, A. Schiele, P. Hartmann, T. Brezesinski, J. Janek, *J. Phys. Chem. C* **2018**, *122*, 8829–8835.
- [97] J. R. Szczech, S. Jin, *Energy Environ. Sci.* **2011**, *4*, 56–72.
- [98] W.-J. Zhang, *J. Power Sources* **2011**, *196*, 13–24.
- [99] C. K. Chan, H. Peng, G. Liu, K. McIlwraith, X. F. Zhang, R. A. Huggins, Y. Cui, *Nat. Nanotechnol.* **2008**, *3*, 31.
- [100] C. Zhang, Y. Liu, X. Jiao, S. Xiong, J. Song, *J. Electrochem. Soc.* **2019**, *166*, A3675.
- [101] A. J. Louli, M. Genovese, R. Weber, S. Hames, E. Logan, J. Dahn, *J. Electrochem. Soc.* **2019**, *166*, A1291–A1299.
- [102] J. Zhao, G. Zhou, K. Yan, J. Xie, Y. Li, L. Liao, Y. Jin, K. Liu, P.-C. Hsu, J. Wang, H.-M. Cheng, Y. Cui, *Nat. Nanotechnol.* **2017**, *12*, 993–999.
- [103] E. Peled, *J. Electrochem. Soc.* **1979**, *126*, 2047–2051.
- [104] E. Peled, D. Golodnitsky, G. Ardel, *J. Electrochem. Soc.* **1997**, *144*, L208–L210.
- [105] D. Aurbach, Y. Ein-Ely, A. Zaban, *J. Electrochem. Soc. Interface* **1994**, *141*, L1–L3.
- [106] D. Aurbach, B. Markovsky, M. D. Levi, E. Levi, A. Schechter, M. Moshkovich, Y. Cohen, *J. Power Sources* **1999**, *81–82*, 95–111.
- [107] A. Schechter, D. Aurbach, H. Cohen, *Langmuir* **1999**, *15*, 3334–3342.
- [108] H. Nakai, T. Kubota, A. Kita, A. Kawashima, *J. Electrochem. Soc.* **2011**, *158*, A798–A801.
- [109] M. Nie, D. P. Abraham, Y. Chen, A. Bose, B. L. Lucht, *J. Phys. Chem. C* **2013**, *117*, 13403–13412.
- [110] Y.-X. Lin, Z. Liu, K. Leung, L.-Q. Chen, P. Lu, Y. Qi, *J. Power Sources* **2016**, *309*, 221–230.
- [111] S. J. An, J. Li, C. Daniel, D. Mohanty, S. Nagpure, D. L. Wood, *Carbon* **2016**, *105*, 52–76.
- [112] M. Gauthier, T. J. Carney, A. Grimaud, L. Giordano, N. Pour, H.-H. Chang, D. P. Fenning, S. F. Lux, O. Paschos, C. Bauer, *J. Phys. Chem. Lett.* **2015**, *6*, 4653–4672.
- [113] A. v Cresce, S. M. Russell, D. R. Baker, K. J. Gaskell, K. Xu, *Nano Lett.* **2014**, *14*, 1405–1412.
- [114] K. N. Wood, M. Noked, N. P. Dasgupta, *ACS Energy Lett.* **2017**, *2*, 664–672.
- [115] X.-B. Cheng, Q. Zhang, *J. Mater. Chem. A* **2015**, *3*, 7207–7209.
- [116] Z. Liu, Y. Qi, Y. Lin, L. Chen, P. Lu, L. Chen, *J. Electrochem. Soc.* **2016**, *163*, A592–A598.
- [117] D. Lu, Y. Shao, T. Lozano, W. D. Bennett, G. L. Graff, B. Polzin, J. Zhang, M. H. Engelhard, N. T. Saenz, W. A. Henderson, P. Bhattacharya, J. Liu, J. Xiao, *Adv. Energy Mater.* **2015**, *5*, 1400993.
- [118] E. P. Kamphaus, S. Angarita-Gomez, X. Qin, M. Shao, M. Engelhard, K. T. Mueller, V. Murugesan, P. B. Balbuena, *ACS Appl. Mater. Interfaces* **2019**, *11*, 31467–31476.
- [119] H. Liu, X.-B. Cheng, Z. Jin, R. Zhang, G. Wang, L.-Q. Chen, Q.-B. Liu, J.-Q. Huang, Q. Zhang, *EnergyChem* **2019**, *1*, 100003.
- [120] R. Fong, U. Von Sacken, J. R. Dahn, *J. Electrochem. Soc.* **1990**, *137*, 2009–2013.
- [121] P. Verma, P. Maire, P. Novák, *Electrochim. Acta* **2010**, *55*, 6332–6341.
- [122] X. Liang, Q. Pang, I. R. Kochetkov, M. S. Sempere, H. Huang, X. Sun, L. F. Nazar, *Nat. Energy* **2017**, *2*, 17119.
- [123] A. M. Haregewoin, A. S. Wotango, B.-J. Hwang, *Energy Environ. Sci.* **2016**, *9*, 1955–1988.
- [124] D. Aurbach, M. Daroux, P. Faguy, E. Yeager, *J. Electrochem. Soc.* **1987**, *134*, 1611–1620.
- [125] S. K. Heiskanen, J. Kim, B. L. Lucht, *Joule* **2019**, *3*, 2322–2333.
- [126] B. S. Parimalam, B. L. Lucht, *J. Electrochem. Soc.* **2018**, *165*, A251–A255.
- [127] D. Aurbach, A. Zaban, A. Schechter, Y. Ein-Eli, E. Zinigrad, B. Markovsky, *J. Electrochim. Soc.* **1995**, *142*, 2873–2882.
- [128] K. Xu, *Chem. Rev.* **2004**, *104*, 4303–4418.
- [129] Y. Gofer, M. Ben-Zion, D. Aurbach, *J. Power Sources* **1992**, *39*, 163–178.
- [130] Y. He, Y. Zhang, P. Yu, F. Ding, X. Li, Z. Wang, Z. Lv, X. Wang, Z. Liu, X. Huang, *J. Energy Chem.* **2020**, *45*, 1–6.
- [131] Y. Zhao, G. Li, Y. Gao, D. Wang, Q. Huang, D. Wang, *ACS Energy Lett.* **2019**, *4*, 1271–1278.
- [132] Y. Yang, D. M. Davies, Y. Yin, O. Borodin, J. Z. Lee, C. Fang, M. Olgun, Y. Zhang, E. S. Sablina, X. Wang, C. S. Rustomji, Y. S. Meng, *Joule* **2019**, *3*, 1986–2000.
- [133] M. Balaish, A. Kravtsberg, Y. Ein-Eli, *Phys. Chem. Chem. Phys.* **2014**, *16*, 2801–2822.
- [134] S. S. Zhang, *J. Power Sources* **2013**, *231*, 153–162.
- [135] D. Aurbach, Y. Talyosef, B. Markovsky, E. Markevich, E. Zinigrad, L. Asraf, J. S. Gnanaraj, H.-J. Kim, *Electrochim. Acta* **2004**, *50*, 247–254.
- [136] K. Hayashi, Y. Nemoto, S. -i Tobishima, J. -i Yamaki, *Electrochim. Acta* **1999**, *44*, 2337–2344.
- [137] D. H. Jang, S. M. Oh, J. *Electrochim. Soc.* **1997**, *144*, 3342–3348.
- [138] C. Monroe, J. Newman, *J. Electrochim. Soc.* **2005**, *152*, A396–A404.
- [139] G. Stone, S. Mullin, A. Teran, D. Hallinan, A. Minor, A. Hexemer, N. Balsara, *J. Electrochim. Soc.* **2012**, *159*, A222–A227.
- [140] A. Manthiram, L. Li, *Adv. Energy Mater.* **2015**, *5*, 1401302.
- [141] L. Grande, E. Paillard, J. Hassoun, J.-B. Park, Y.-J. Lee, Y.-K. Sun, S. Passerini, B. Scrosati, *Adv. Mater.* **2015**, *27*, 784–800.
- [142] Z.-K. Luo, C.-S. Liang, F. Wang, Y.-H. Xu, J. Chen, D. Liu, H.-Y. Sun, H. Yang, X.-P. Fan, *Adv. Funct. Mater.* **2014**, *24*, 2101–2105.
- [143] T. Liu, X.-L. Feng, X. Jin, M.-Z. Shao, Y.-T. Su, Y. Zhang, X.-B. Zhang, *Angew. Chem. Int. Ed.* **2019**, *58*, 18240–18245.
- [144] Y.-S. Hong, C.-Z. Zhao, Y. Xiao, R. Xu, J.-J. Xu, J.-Q. Huang, Q. Zhang, X. Yu, H. Li, *Batteries Supercaps* **2019**, *2*, 638–658.
- [145] H.-K. Kim, H.-D. Lim, K.-Y. Park, D.-H. Seo, H. Gwon, J. Hong, W. A. Goddard, H. Kim, K. Kang, *J. Am. Chem. Soc.* **2013**, *135*, 9733–9742.
- [146] W. Xu, J. Xiao, D. Wang, J. Zhang, J.-G. Zhang, *Electrochim. Solid-State Lett.* **2010**, *13*, A48–A51.
- [147] J.-S. Lee, S. Tai Kim, R. Cao, N.-S. Choi, M. Liu, K. T. Lee, J. Cho, *Adv. Energy Mater.* **2011**, *1*, 34–50.
- [148] W. Walker, V. Giordani, J. Uddin, V. S. Bryantsev, G. V. Chase, D. Addison, *J. Am. Chem. Soc.* **2013**, *135*, 2076–2079.
- [149] D. Sharon, M. Afri, M. Noked, A. Garsuch, A. A. Frimer, D. Aurbach, *J. Phys. Chem. Lett.* **2013**, *4*, 3115–3119.
- [150] T. Kuboki, T. Okuyama, T. Ohsaki, N. Takami, *J. Power Sources* **2005**, *146*, 766–769.
- [151] Y. Chen, S. A. Freunberger, Z. Peng, F. Bardé, P. G. Bruce, *J. Am. Chem. Soc.* **2012**, *134*, 7952–7957.
- [152] Z. Peng, S. A. Freunberger, Y. Chen, P. G. Bruce, *Science* **2012**, *337*, 563–566.
- [153] W. Xu, K. Xu, V. V. Viswanathan, S. A. Towne, J. S. Hardy, J. Xiao, Z. Nie, D. Hu, D. Wang, J.-G. Zhang, *J. Power Sources* **2011**, *196*, 9631–9639.
- [154] B. D. McCloskey, R. Scheffler, A. Speidel, D. S. Bethune, R. M. Shelby, A. C. Luntz, *J. Am. Chem. Soc.* **2011**, *133*, 18038–18041.

- [155] D. Aurbach, B. D. McCloskey, L. F. Nazar, P. G. Bruce, *Nat. Energy* **2016**, 1, 16128.
- [156] J. Zhang, B. Sun, Y. Zhao, A. Tkacheva, Z. Liu, K. Yan, X. Guo, A. M. McDonagh, D. Shanmukaraj, C. Wang, T. Rojo, M. Armand, Z. Peng, G. Wang, *Nat. Commun.* **2019**, 10, 602.
- [157] X. P. Zhang, Y. Y. Sun, Z. Sun, C. S. Yang, T. Zhang, *Nat. Commun.* **2019**, 10, 3543.
- [158] J. Liu, T. Wu, S. Zhang, D. Li, Y. Wang, H. Xie, J. Yang, G. Sun, *J. Power Sources* **2019**, 439, 227095.
- [159] C. V. Amanchukwu, J. R. Harding, Y. Shao-Horn, P. T. Hammond, *Chem. Mater.* **2015**, 27, 550–561.
- [160] J. Zhu, J. Yang, J. Zhou, T. Zhang, L. Li, J. Wang, Y. Nuli, *J. Power Sources* **2017**, 366, 265–269.
- [161] Y. Yu, Y.-B. Yin, J.-L. Ma, Z.-W. Chang, T. Sun, Y.-H. Zhu, X.-Y. Yang, T. Liu, X.-B. Zhang, *Energy Storage Mater.* **2019**, 18, 382–388.
- [162] D. J. Lee, H. Lee, J. Song, M.-H. Ryou, Y. M. Lee, H.-T. Kim, J.-K. Park, *Electrochem. Commun.* **2014**, 40, 45–48.
- [163] D. J. Lee, H. Lee, Y. J. Kim, J. K. Park, H. T. Kim, *Adv. Mater.* **2016**, 28, 857–863.
- [164] K. Liao, S. Wu, X. Mu, Q. Lu, M. Han, P. He, Z. Shao, H. Zhou, *Adv. Mater.* **2018**, e1705711.
- [165] H.-J. Peng, J.-Q. Huang, X.-B. Cheng, Q. Zhang, *Adv. Energy Mater.* **2017**, 7, 1700260.
- [166] M. Rana, S. A. Ahad, M. Li, B. Luo, L. Wang, I. Gentle, R. Knibbe, *Energy Storage Mater.* **2019**, 18, 289–310.
- [167] W. Xue, L. Miao, L. Qie, C. Wang, S. Li, J. Wang, J. Li, *Curr Opin Electrochem* **2017**, 6, 92–99.
- [168] J.-H. Jiang, A.-B. Wang, W.-K. Wang, Z.-Q. Jin, L.-Z. Fan, *J. Energy Chem.* **2020**, 46, 114–122.
- [169] J. Liang, X. Li, Y. Zhao, L. V. Goncharova, G. Wang, K. R. Adair, C. Wang, R. Li, Y. Zhu, Y. Qian, L. Zhang, R. Yang, S. Lu, X. Sun, *Adv. Mater.* **2018**, 30, 1804684.
- [170] Q. J. Meisner, T. Rojas, N. L. Dietz Rago, J. Cao, J. Bareño, T. Glossmann, A. Hintennach, P. C. Redfern, D. Pahls, L. Zhang, I. D. Bloom, A. T. Ngo, L. A. Curtiss, Z. Zhang, *J. Power Sources* **2019**, 438, 226939.
- [171] C. Yan, X.-Q. Zhang, J.-Q. Huang, Q. Liu, Q. Zhang, *Trends Chem.* **2019**, 1, 693–704.
- [172] C. Xiong, Y. X. Ren, H. R. Jiang, M. C. Wu, T. S. Zhao, *J. Energy Storage* **2019**, 26, 101006.
- [173] Y. Zhong, Y. Chen, Y. Cheng, Q. Fan, H. Zhao, H. Shao, Y. Lai, Z. Shi, X. Ke, Z. Guo, *ACS Appl. Mater. Interfaces* **2019**, 11, 37726–37731.
- [174] M. Li, X. Liu, Q. Li, Z. Jin, W. Wang, A. Wang, Y. Huang, Y. Yang, *J. Energy Chem.* **2020**, 41, 27–33.
- [175] K. Chen, R. Pathak, A. Gurung, E. A. Adhamash, B. Bahrami, Q. He, H. Qiao, A. L. Smirnova, J. J. Wu, Q. Qiao, Y. Zhou, *Energy Storage Mater.* **2019**, 18, 389–396.
- [176] T. Chen, W. Kong, P. Zhao, H. Lin, Y. Hu, R. Chen, W. Yan, Z. Jin, *Chem. Mater.* **2019**, 31, 7565–7573.
- [177] Y. Zhao, D. Wang, Y. Gao, T. Chen, Q. Huang, D. Wang, *Nano Energy* **2019**, 64, 103893.
- [178] S. Xia, X. Zhang, C. Liang, Y. Yu, W. Liu, *Energy Storage Mater.* **2020**, 24, 329–335.
- [179] W. Wang, X. Yue, J. Meng, J. Wang, X. Wang, H. Chen, D. Shi, J. Fu, Y. Zhou, J. Chen, Z. Fu, *Energy Storage Mater.* **2019**, 18, 414–422.
- [180] J. Bobnar, M. Lozinsek, G. Kapun, C. Njel, R. Dedryvere, B. Genorio, R. Dominiko, *Sci. Rep.* **2018**, 8, 5819.
- [181] C. Zhang, Q. Lan, Y. Liu, J. Wu, H. Shao, H. Zhan, Y. Yang, *Electrochim. Acta* **2019**, 306, 407–419.
- [182] Y. Nan, S. Li, M. Zhu, B. Li, S. Yang, *ACS Appl. Mater. Interfaces* **2019**, 11, 28878–28884.
- [183] S. Li, H. Dai, Y. Li, C. Lai, J. Wang, F. Huo, C. Wang, *Energy Storage Mater.* **2019**, 18, 222–228.
- [184] J. Chen, H. Yang, X. Zhang, J. Lei, H. Zhang, H. Yuan, J. Yang, Y. Nuli, J. Wang, *ACS Appl. Mater. Interfaces* **2019**, 11, 33419–33427.
- [185] A. Paolella, H. Demers, P. Chevallier, C. Gagnon, G. Girard, N. Delaporte, W. Zhu, A. Vijh, A. Guerfi, K. Zaghib, *J. Power Sources* **2019**, 427, 201–206.
- [186] X. Yan, H. Zhang, M. Huang, M. Qu, Z. Wei, *ChemSusChem* **2019**, 12, 2263–2270.
- [187] Q. Tang, H. Li, Y. Pan, J. Zhang, Y. Chen, *Ionics* **2019**, 25, 2525–2533.
- [188] L. L. Kong, L. Wang, Z. C. Ni, S. Liu, G. R. Li, X. P. Gao, *Adv. Funct. Mater.* **2019**, 29, 1808756.
- [189] H. Fan, Q. Dong, C. Gao, B. Hong, Z. Zhang, K. Zhang, Y. Lai, *ACS Appl. Mater. Interfaces* **2019**, 11, 30902–30910.
- [190] Z. Liang, D. Lin, J. Zhao, Z. Lu, Y. Liu, C. Liu, Y. Lu, H. Wang, K. Yan, X. Tao, Y. Cui, *Proc. Natl. Acad. Sci. USA* **2016**, 113, 2862–2867.
- [191] C. P. Yang, Y. X. Yin, S. F. Zhang, N. W. Li, Y. G. Guo, *Nat. Commun.* **2015**, 6, 8058.
- [192] F. Pei, A. Fu, W. Ye, J. Peng, X. Fang, M. S. Wang, N. Zheng, *ACS Nano* **2019**, 13, 8337–8346.
- [193] Y. X. Ren, L. Zeng, H. R. Jiang, W. Q. Ruan, Q. Chen, T. S. Zhao, *Nat. Commun.* **2019**, 10, 3249.
- [194] X.-B. Cheng, C. Yan, X. Chen, C. Guan, J.-Q. Huang, H.-J. Peng, R. Zhang, S.-T. Yang, Q. Zhang, *Chem* **2017**, 2, 258–270.
- [195] J. Qian, L. Liu, J. Yang, S. Li, X. Wang, H. L. Zhuang, Y. Lu, *Nat. Commun.* **2018**, 9, 4918–4918.
- [196] J. Lim, A. Choi, H. Kim, S. W. Doo, Y. Park, K. T. Lee, *J. Power Sources* **2019**, 426, 162–168.
- [197] J. Zheng, Z. Yang, A. Dai, L. Tang, H. Wei, Y. Li, Z. He, J. Lu, *Small* **2019**, 15, 1904854.
- [198] A. Grenier, H. Liu, K. M. Wiaderek, Z. W. Lebens-Higgins, O. J. Borkiewicz, L. F. J. Piper, P. J. Chupas, K. W. Chapman, *Chem. Mater.* **2017**, 29, 7345–7352.
- [199] E. Markevich, G. Salitra, P. Hartmann, J. Kulisch, D. Aurbach, K.-J. Park, C. S. Yoon, Y.-K. Sun, *J. Electrochem. Soc.* **2019**, 166, A5265–A5274.
- [200] A. Eftekhar, *ACS Sustainable Chem. Eng.* **2019**, 7, 3684–3687.
- [201] P. Jankowski, W. Wieczorek, P. Johansson, *J. Mol.* **2016**, 23, 6.
- [202] P. Peljo, H. H. Girault, *Energy Environ. Sci.* **2018**, 11, 2306–2309.
- [203] D.-J. Yoo, S. Yang, Y. S. Yun, J. H. Choi, D. Yoo, K. J. Kim, J. W. Choi, *Adv. Energy Mater.* **2018**, 8, 1802365.
- [204] Y.-M. Lin, K. C. Klavetter, P. R. Abel, N. C. Davy, J. L. Snider, A. Heller, C. B. Mullins, *Chem Comm* **2012**, 48, 7268–7270.
- [205] V. Etacheri, O. Haik, Y. Goffer, G. A. Roberts, I. C. Stefan, R. Fasching, D. Aurbach, *Langmuir* **2012**, 28, 965–976.
- [206] D. M. Seo, C. C. Nguyen, B. T. Young, D. R. Heskett, J. C. Woicik, B. L. Lucht, *J. Electrochem. Soc.* **2015**, 162, A7091–A7095.
- [207] S. A. Webb, C. A. Bridges, G. M. Veith, *J. Power Sources* **2014**, 248, 1105–1117.
- [208] C.-C. Su, M. He, R. Amine, Z. Chen, R. Sahore, N. Dietz Rago, K. Amine, *Energy Storage Mater.* **2019**, 17, 284–292.
- [209] X.-Q. Zhang, X. Chen, X.-B. Cheng, B.-Q. Li, X. Shen, C. Yan, J.-Q. Huang, Q. Zhang, *Angew. Chem. Int. Ed.* **2018**, 57, 5301–5305; *Angew. Chem.* **2018**, 130, 5399–5403.
- [210] X.-Q. Zhang, X.-B. Cheng, X. Chen, C. Yan, Q. Zhang, *Adv. Funct. Mater.* **2017**, 27, 1605989.
- [211] Z. L. Brown, S. Jurng, C. C. Nguyen, B. L. Lucht, *ACS Appl. Energy Mater.* **2018**, 1, 3057–3062.
- [212] E. Markevich, G. Salitra, F. Chesneau, M. Schmidt, D. Aurbach, *ACS Energy Lett.* **2017**, 2, 1321–1326.
- [213] C. Yan, X. B. Cheng, Y. Tian, X. Chen, X. Q. Zhang, W. J. Li, J. Q. Huang, Q. Zhang, *Adv. Mater.* **2018**, 30, e1707629.
- [214] Z. Peng, J. Song, L. Huai, H. Jia, B. Xiao, L. Zou, G. Zhu, A. Martinez, S. Roy, V. Murugesan, H. Lee, X. Ren, Q. Li, B. Liu, X. Li, D. Wang, W. Xu, J.-G. Zhang, *Adv. Energy Mater.* **2019**, 9, 1901764.
- [215] Q. Ma, H. Zhang, C. Zhou, L. Zheng, P. Cheng, J. Nie, W. Feng, Y.-S. Hu, H. Li, X. Huang, L. Chen, M. Armand, Z. Zhou, *Angew. Chem. Int. Ed.* **2016**, 55, 2521–2525; *Angew. Chem.* **2016**, 128, 2567–2571.
- [216] I. Villaluenga, K. H. Wujcik, W. Tong, D. Devaux, D. H. Wong, J. M. DeSimone, N. P. Balsara, *Natl. Acad. Sci. U. S. A.* **2016**, 113, 52–57.
- [217] L. Porcarelli, A. S. Shaplov, F. Bella, J. R. Nair, D. Mecerreyres, C. Gerbaldi, *ACS Energy Lett.* **2016**, 1, 678–682.
- [218] S. S. Park, Y. Tulchinsky, M. Dincă, *J. Am. Chem. Soc.* **2017**, 139, 13260–13263.
- [219] H.-D. Nguyen, G.-T. Kim, J. Shi, E. Paillard, P. Judeinstein, S. Lyonnard, D. Bresser, C. Iojoiu, *Energy Environ. Sci.* **2018**, 11, 3298–3309.
- [220] S. Li, A. I. Mohamed, V. Pande, H. Wang, J. Cuthbert, X. Pan, H. He, Z. Wang, V. Viswanathan, J. F. Whitacre, K. Matyjaszewski, *ACS Energy Lett.* **2018**, 3, 20–27.
- [221] H. G. Buss, S. Y. Chan, N. A. Lynd, B. D. McCloskey, *ACS Energy Lett.* **2017**, 2, 481–487.
- [222] Z. Yu, D. G. Mackanic, W. Michaels, M. Lee, A. Pei, D. Feng, Q. Zhang, Y. Tsao, C. V. Amanchukwu, X. Yan, H. Wang, S. Chen, K. Liu, J. Kang, J. Qin, Y. Cui, Z. Bao, *Joule* **2019**, 3, 2761–2776.
- [223] Z. Tu, S. Choudhury, M. J. Zachman, S. Wei, K. Zhang, L. F. Kourkoutis, L. A. Archer, *Joule* **2017**, 1, 394–406.
- [224] X. Shen, H. Liu, X.-B. Cheng, C. Yan, J.-Q. Huang, *Energy Storage Mater.* **2018**, 12, 161–175.
- [225] Z. Ahmad, T. Xie, C. Maheshwari, J. C. Grossman, V. Viswanathan, *ACS Cent. Sci.* **2018**, 4, 996–1006.

- [226] R. Pathak, K. Chen, A. Gurung, K. M. Reza, B. Bahrami, F. Wu, A. Chaudhary, N. Ghimire, B. Zhou, W.-H. Zhang, Y. Zhou, Q. Qiao, *Adv. Energy Mater.* **2019**, *9*, 1901486.
- [227] C. Yan, R. Xu, J.-L. Qin, H. Yuan, Y. Xiao, L. Xu, J.-Q. Huang, *Angew. Chem. Int. Ed.* **2019**, *58*, 15235–15238.
- [228] G. Li, Z. Liu, D. Wang, X. He, S. Liu, Y. Gao, A. AlZahrani, S. H. Kim, L. Q. Chen, D. Wang, *Adv. Energy Mater.* **2019**, *9*, 1900704.
- [229] J. I. Lee, M. Shin, D. Hong, S. Park, *Adv. Energy Mater.* **2019**, *9*, 1803722.
- [230] A. J. Leenheer, K. L. Jungjohann, K. R. Zavadil, J. P. Sullivan, C. T. Harris, *ACS Nano* **2015**, *9*, 4379–4389.
- [231] D. Liu, Z. Shadike, R. Lin, K. Qian, H. Li, K. Li, S. Wang, Q. Yu, M. Liu, S. Ganapathy, X. Qin, Q.-H. Yang, M. Wagemaker, F. Kang, X.-Q. Yang, B. Li, *Adv. Mater.* **2019**, *31*, 1806620.
- [232] Q. Li, T. Yi, X. Wang, H. Pan, B. Quan, T. Liang, X. Guo, X. Yu, H. Wang, X. Huang, L. Chen, H. Li, *Nano Energy* **2019**, *63*, 103895.
- [233] H. Wang, F. Wang, *Curr. Opin. Chem. Eng.* **2016**, *13*, 170–178.
- [234] J.-H. Cheng, A. A. Assegie, C.-J. Huang, M.-H. Lin, A. M. Tripathi, C.-C. Wang, M.-T. Tang, Y.-F. Song, W.-N. Su, B. J. Hwang, *J. Phys. Chem. C* **2017**, *121*, 7761–7766.
- [235] X. Shen, Y. Li, T. Qian, J. Liu, J. Zhou, C. Yan, J. B. Goodenough, *Nat. Commun.* **2019**, *10*, 900.
- [236] Y. Chen, M. Yue, C. Liu, H. Zhang, Y. Yu, X. Li, H. Zhang, *Adv. Funct. Mater.* **2019**, *29*, 1806752.
- [237] K. N. Wood, E. Kazyak, A. F. Chadwick, K.-H. Chen, J.-G. Zhang, K. Thornton, N. P. Dasgupta, *ACS Cent. Sci.* **2016**, *2*, 790–801.
- [238] L. Porz, T. Swamy, B. W. Sheldon, D. Rettenwander, T. Frömling, H. L. Thaman, S. Berendts, R. Uecker, W. C. Carter, Y.-M. Chiang, *Adv. Energy Mater.* **2017**, *7*, 1701003.
- [239] A. C. Kozen, C.-F. Lin, O. Zhao, S. B. Lee, G. W. Rubloff, M. Noked, *Chem. Mater.* **2017**, *29*, 6298–6307.
- [240] K. Xu, M. Zhu, X. Wu, J. Liang, Y. Liu, T. Zhang, Y. Zhu, Y. Qian, *Energy Storage Mater.* **2019**, *23*, 587–593.
- [241] G. Rong, X. Zhang, W. Zhao, Y. Qiu, M. Liu, F. Ye, Y. Xu, J. Chen, Y. Hou, W. Li, W. Duan, Y. Zhang, *Adv. Mater.* **2017**, *29*, 1606187.
- [242] M. Nagao, A. Hayashi, M. Tsumisago, T. Kanetsuku, T. Tsuda, S. Kuwabata, *Phys. Chem. Chem. Phys.* **2013**, *15*, 18600–18606.
- [243] S. H. Kim, K. Kim, H. Choi, D. Im, S. Heo, H. S. Choi, *J. Mater. Chem. A* **2019**, *7*, 13650–13657.
- [244] K. Yan, Z. Lu, H.-W. Lee, F. Xiong, P.-C. Hsu, Y. Li, J. Zhao, S. Chu, Y. Cui, *Nat. Energy* **2016**, *1*, 16010.
- [245] R. R. Unocic, X.-G. Sun, R. L. Sacci, L. A. Adamczyk, D. H. Alsem, S. Dai, N. J. Dudney, K. L. More, *Microsc. Microanal.* **2014**, *20*, 1029–1037.
- [246] A. Kushima, K. P. So, C. Su, P. Bai, N. Kuriyama, T. Maebashi, Y. Fujiwara, M. Z. Bazant, J. Li, *Nano Energy* **2017**, *32*, 271–279.
- [247] Y. Li, Y. Li, A. Pei, K. Yan, Y. Sun, C.-L. Wu, L.-M. Joubert, R. Chin, A. L. Koh, Y. Yu, J. Perrino, B. Butz, S. Chu, Y. Cui, *Science* **2017**, *358*, 506–510.
- [248] W. Huang, D. T. Boyle, Y. Li, Y. Li, A. Pei, H. Chen, Y. Cui, *ACS Nano* **2019**, *13*, 737–744.
- [249] K. Fu, Y. Gong, Z. Fu, H. Xie, Y. Yao, B. Liu, M. Carter, E. Wachsman, L. Hu, *Angew. Chem. Int. Ed.* **2017**, *56*, 14942–14947; *Angew. Chem.* **2017**, *129*, 15138–15143.
- [250] S. Liu, X. Xia, S. Deng, D. Xie, Z. Yao, L. Zhang, S. Zhang, X. Wang, J. Tu, *Adv. Mater.* **2019**, *31*, e1806470.
- [251] X. Fan, L. Chen, X. Ji, T. Deng, S. Hou, J. Chen, J. Zheng, F. Wang, J. Jiang, K. Xu, C. Wang, *Chem* **2018**, *4*, 174–185.
- [252] Y. Liu, D. Lin, Y. Li, G. Chen, A. Pei, O. Nix, Y. Li, Y. Cui, *Nat. Commun.* **2018**, *9*, 3656.
- [253] S. Lv, T. Verhallen, A. Vasileiadis, F. Ooms, Y. Xu, Z. Li, Z. Li, M. Wagemaker, *Nat. Commun.* **2018**, *9*, 2152.
- [254] Q. Cheng, L. Wei, Z. Liu, N. Ni, Z. Sang, B. Zhu, W. Xu, M. Chen, Y. Miao, L.-Q. Chen, W. Min, Y. Yang, *Nat. Commun.* **2018**, *9*, 2942.
- [255] Q. C. Liu, J. J. Xu, S. Yuan, Z. W. Chang, D. Xu, Y. B. Yin, L. Li, H. X. Zhong, Y. S. Jiang, J. M. Yan, X. B. Zhang, *Adv. Mater.* **2015**, *27*, 5241–5247.
- [256] D. Wang, F. Zhang, P. He, H. Zhou, *Angew. Chem. Int. Ed.* **2019**, *58*, 2355–2359.
- [257] B. Liu, W. Xu, J. Tao, P. Yan, J. Zheng, M. H. Engelhard, D. Lu, C. Wang, J.-G. Zhang, *Adv. Energy Mater.* **2018**, *8*, 1702340.
- [258] W.-J. Kwak, S.-J. Park, H.-G. Jung, Y.-K. Sun, *Adv. Energy Mater.* **2018**, *8*, 1702258.
- [259] J. Amici, M. Alidoost, F. Caldera, D. Versaci, U. Zubair, F. Trotta, C. Francia, S. Bodardo, *ChemElectroChem* **2018**, *5*, 1599–1605.
- [260] Z. Huang, J. Ren, W. Zhang, M. Xie, Y. Li, D. Sun, Y. Shen, Y. Huang, *Adv. Mater.* **2018**, *30*, 1803270.
- [261] H. Dong, X. Xiao, C. Jin, X. Wang, P. Tang, C. Wang, Y. Yin, D. Wang, S. Yang, C. Wu, *J. Power Sources* **2019**, *423*, 72–79.
- [262] H. Wu, Q. Wu, F. Chu, J. Hu, Y. Cui, C. Yin, C. Li, *J. Power Sources* **2019**, *419*, 72–81.
- [263] G. Wang, C. Chen, Y. Chen, X. Kang, C. Yang, F. Wang, Y. Liu, X. Xiong, *Angew. Chem. Int. Ed.* **2020**, *59*, 2055–2060.

Manuscript received: January 16, 2020

Revised manuscript received: March 27, 2020

Accepted manuscript online: March 27, 2020

Version of record online: April 20, 2020